A comprehensive model of the Antarctic lithosphere based on geophysical data integration

Dissertation

zur Erlangung des Grades eines
Doktors der Naturwissenschaften.
Vorgelegt von

Carina Haeger

am Fachbereich Geowissenschaften der Freien Universität Berlin,
angefertigt am Deutschen GeoForschungszentrum GFZ, Potsdam.

Berlin, 2019

Autor:	Carina Haeger
Erstgutachter:	Prof. Dr. Maik Thomas
Zweitgutachter:	Prof. Dr. Jörg Ebbing (Universität Kiel)
Datum der Einreichung:	03.09.2019
Datum der Disputation:	08.11.2019

Contents

Eidesstattliche Erklärung

Hiermit versichere ich, dass ich die vorliegende Dissertation selbstständig angefertigt habe und keine anderen als die angegebenen Quellen und Hilfsmittel benutzt habe, sowie Zitate kenntlich gemacht habe. Ein Promotionsverfahren zu einem früheren Zeitpunkt an einer anderen Hochschule oder bei einem anderen Fachbereich wurde nicht beantragt.

Potsdam, 02. September 2019

Abstract

The Antarctic continent is almost entirely ($\sim 99\,\%$) covered by a thick ice layer impeding classical in-situ measurements. It hence remains one of the least geophysically known areas on Earth. Little is known about the structure and the thermal and rheological properties of its lithosphere. Since the state of the lithosphere is strongly linked to near-surface processes such as ice dynamics or glacial isostatic adjustment (GIA) as well as the deeper, convecting mantle, knowledge of those properties is crucially important when modeling the coupled systems. This cumulative thesis consists of three published scientific papers that together characterize the lithosphere of Antarctica in terms of strength, temperature, density, composition and upper crustal properties.

As a measure of strength, the effective elastic thickness T_e was derived by cross-spectral analysis of the gravity field with the adjusted topography. The fan wavelet technique was employed to, for the first time, calculate variations of T_e over the entire continent by means of admittance and coherence analysis. The same gravity and topography data was then combined with tomography models constrained by mineral physics equations in an iterative inversion scheme to develop a 3D density, thermal and compositional model of the Antarctic lithosphere and upper mantle. Seismic data on crustal structures was further employed to create a new Moho and crustal density model. In order to investigate upper crustal structures and properties, corrections of the gravity effect of isostatic compensation of geological loads were further applied to the isostatic gravity anomalies. The resulting so-called decompensative gravity anomalies were translated into sediment distributions previously hidden below the ice sheet.

A general division of the Antarctic lithosphere is confirmed by all parameters under study. A transition is visible along the Transantarctic Mountains. Whether the mountain chain belongs to West Antarctica (WANT) or East Antarctica (EANT) has been under question, but especially the estimates of T_e indicate a closer connection to WANT. Apart from this general division, lithospheric fragmentation was discovered within EANT. Cratonic fragments of Precambrian origin exhibiting high depletion, low temperatures and high T_e were detected in Dronning Maud Land, in Wilkes Land and close to the South Pole. The latter

two are likely part of the Mawson craton. Lithospheric weakening combined with an almost primitive upper mantle exists in the Lambert Graben and was probably the result of rifting in the East Antarctic Rift System. The obtained decompensative gravity anomalies correspond well to known sedimentary basins such as the Lambert Graben and the Filchner-Ronne Ice shelf. They also suggest the presence of large sedimentary deposits that were not ore only sparsely mapped previously. Therefore, this thesis provides a comprehensive model of the lithosphere of Antarctica and a basis for further analysis of its coupling with the deep mantle and surface processes. As such, the resulting model facilitates surface heat flux modeling and estimates of upper mantle viscosity crucial for GIA modeling.

Kurzfassung

Geophysikalisch gesehen ist die Antarktis bis heute eines der am wenigsten bekannten Gebiete auf der Erde, da In-situ-Messungen durch die dicke Eiskappe, die 99 % des Kontinents bedeckt, stark behindert werden. Über die Struktur und die thermischen und rheologischen Eigenschaften seiner Lithosphäre ist daher wenig bekannt. Da der Zustand der Lithosphäre stark mit oberflächennahen Prozessen und der Eisdynamik sowie dem tieferen, konvektierenden Mantel verbunden ist, ist die Kenntnis dieser Eigenschaften für die Modellierung der gekoppelten Systeme von entscheidender Bedeutung. Diese kumulative These besteht aus drei veröffentlichten wissenschaftlichen Arbeiten, die zusammen die Lithosphäre der Antarktis in Bezug auf Stärke, Temperatur, Dichte, Zusammensetzung und Eigenschaften der oberen Kruste charakterisieren.

Als Maß für die Stärke wird die effektive elastische Dicke T_e durch Kreuzspektralanalyse des Schwerefeldes mit der eingestellten Topographie abgeleitet. Die Fan-Wavelet-Technik wurde verwendet, um Variationen von T_e über den gesamten Kontinent mittels Admittanz- und Kohärenzanalyse zu berechnen. Die gleichen Schwerkraft- und Topographiedaten wurden dann mit Tomographiemodellen, verknüpft mit mineralphysikalische Gleichungen, in einem iterativen Inversionsschema kombiniert, um ein 3D-Dichte-, Wärme- und Zusammensetzungsmodell der antarktischen Lithosphäre und des oberen Mantels zu entwickeln. Seismische Daten zu Krustenstrukturen wurden weiter verwendet, um ein neues Moho- und Krustendichtemodell zu erstellen. Um die Strukturen und Eigenschaften der oberen Kruste zu untersuchen, wurden dekompensierten Korrekturen an den isostatischen Anomalien des Gravitationsfeldes vorgenommen. Diese dekompensierten Gravitationsanomalien wurden in Sedimentverteilungen übersetzt, die zuvor unter der Eisdecke verborgen waren.

Die allgemeine Unterteilung der antarktischen Lithosphäre wird durch alle untersuchten Parameter bestätigt. Ein Übergang ist entlang des Transantarktischen Gebirges sichtbar. Ob die Gebirgskette zur Westantarktis (WANT) oder zur Ostantarktis (EANT) gehört, ist noch fraglich, aber insbesondere die T_e Werte deuten auf eine engere Verbindung zu WANT hin. Abgesehen von dieser allgemeinen Aufteilung wurde in EANT lithosphärische Fragmentierung entdeckt. In Dronning Maud Land, in Wilkes Land und in der Nähe des

Südpols wurden kratonische Fragmente präkambrischen Ursprungs gefunden, die eine hohe Verarmung an Eisen, niedrige Temperaturen und hohe T_e aufweisen. Die beiden letzteren sind wahrscheinlich Teil des Mawson-Kratons. Lithosphärische Schwächung in Kombination mit einem fast primitiven oberen Mantel existiert im Lambert-Graben und war wahrscheinlich das Ergebnis von Rifting im Ostantarktischen Rift-System. Die erhaltenen Anomalien der dekompensierten Gravitationsanomalie decken sich mit bekannten Sedimentbecken wie dem Lambert-Graben und dem Filchner-Ronne-Eisschelfs. Sie deuten auch auf das Vorhandensein großer Sedimentablagerungen hin, die zuvor nicht oder nur spärlich kartiert wurden. Daher bietet diese Arbeit ein umfassendes Modell der Lithosphäre der Antarktis und eine Grundlage für die weitere Analyse ihrer Kopplung mit den Prozessen im tiefen Mantel und ander Oberfläche. Das resultierende Modell ermöglicht die Modellierung des Oberflächenwärmestroms und die Schätzung der Viskosität des oberen Mantels, die für die GIA-Modellierung entscheidend ist.

1 Introduction

1.1. Motivation

Even today, Antarctica remains one of the least studied regions on Earth. Traditional in-situ measurements are strongly hindered by its remoteness, harsh weather conditions and the thick ice cap covering 99 % of the continent. Consequently, little is known about the thermal and rheological properties of the Antarctic lithosphere, which controls to a large extent the initiation and evolution of visco-elastic deformation processes such as glacial isostatic adjustment (GIA). This, in turn, is crucial for monitoring the mass balance of the Antarctic ice sheet. Additionally, it has been recently demonstrated for the Greenland ice shield, that ice dynamics does not only depend on climate forcing but is strongly affected by heat flow from the Earth's interior (Petrunin et al., 2013b) and by the distribution and thickness of sediments below ice streams (Smith et al., 2013). Hence, temperature distributions within the lithosphere are not only important to model lithospheric dynamics, but are also of high relevance when modeling ice behavior and potential consequences for the sea level.
Furthermore, the Antarctic continent held a key position in the Gondwana and Rodinia supercontinents and their subsequent break-ups. Therefore, detailed knowledge of its lithospheric structure is necessary to fully understand the past and present state of the Earth system through reconstruction of plate tectonics.
The rising number of satellite missions and improvements in their sensor technology in recent years offers innovative possibilities to study previously not or only sparsely mapped regions such as the interior of Antarctica. Hence, the main focus of this thesis will be the analysis of the gravity field provided by satellite missions such as GRACE and GOCE, supplemented by ground-based gravity measurements to increase local resolution and provide information within the so-called polar gap, a region around the poles that cannot be covered by satellites in a sun-synchronous orbit. Combination of the gravity data with other, independent sources of data such as seismic reflection, refraction and receiver function data, surface wave tomography, ice penetrating radar and other geophysical data allows to complement and constrain each other, offering more detailed information than any single method could

provide.

The aim of this thesis is to create a continent wide 3D model of the temperature, density, composition and strength of the lithosphere as well as constraints of crustal structures for Antarctica, integrating mainly satellite based gravity data, seismic tomography and other geophysical data, such as seismic reflection, refraction and receiver function data and surface wave tomography. This model produces the first continent-wide map of Antarctica in terms of strength, composition and density. Previous work on T_e only provides information on local scales (Stern and ten Brink, 1989; Yamasaki et al., 2008; Ferraccioli et al., 2011) or averages for the entire EANT and WANT regions (McKenzie et al., 2015). The composition of the Antarctic lithosphere has been studied even less. Xenolith data has been used for local composition analysis (e.g. Goodge, 2018; Jacobs et al., 2015). On larger scales, Kuge and Fukao (2005) detect depleted continental lithosphere in EANT. The thermal state of the lithosphere is better constrained. Several studies on surface heat flux have been conducted (e.g. Martos et al., 2017; Shapiro and Ritzwoller, 2004; Maule et al., 2005) yielding striking differences. The 3D temperature structure was estimated by An et al. (2015a) using a similar mineral physics based approach without taking compositional changes into account. The iterative combination of gravity and seismic analysis also provides the means to not only estimate continent-wide density variations but also to distinguish between the thermal or compositional origin of these variations. Upper crust structures and sediment distribution in Antarctica are still largely unknown. Several local surveys exist (e.g. Bamber et al., 2006; Wobbe et al., 2014; Frederick et al., 2016) that were recently collected in a compilation (Baranov et al., 2018). However, large data gaps prevail. The analysis of decompensative anomalies employed in this thesis offers new insights into the structure of the upper crust on continental scales.

1.2. History and present state of Antarctica studies

The existence of a southern continent named *Terra Australis Incognita* had already been theorized by Ptolemy in 150 AD, it wasn't until 1820 however, that the continent was officially discovered by Fabian Gottlieb Thaddeus von Bellinghausen and Mikhail Lazarev (Fogg, 1992, p. 36). In 1882 and 1883, the first International Polar Year was held by 12 nations as the first international collaboration to collect geophysical data in polar regions (Naylor et al., 2008) but only included two expeditions south (Fogg, 1992, p. 105). Between 1897 and 1922, during the *heroic age of Antarctica expeditions* (Fogg, 1992, p. 128f), many expeditions were designed to increase knowledge about Antarctica itself, characterized by

limited technical resources putting to test personal, physical and mental capacities. It was during this period, that Roald Amundsen and Robert Falcon Scott started their respective expeditions to the South Pole with Amundsen reaching it on December 14th 1911. Scott and his expedition arrived one month later, but, unlike Amundsen, took the time on their return journey to take 16 kg of geologic samples of the Transantarctic Mountains - additional weight that may have lead to their deaths in March 1912 during a blizzard. These samples, along with samples collected by Scott and Shackleton during earlier expeditions through the Transantarcrtic Mountains, however, later supported Alex Du Toit's reconstructions of a southern super continent in 1937 (Dalziel, 1992). A second International Polar Year was held in 1932-1933, but due to the on-going recession, the plan to build a ring of stations around the Antarctic was abandoned (Fogg, 1992, p. 169).

The outline of the Antarctic continent had been mapped by the beginning of the 20th century, but information on ice thickness and sub-ice topography could only be studied in detail, when larger scale seismic soundings became possible with improving transport systems for heavy equipment (Fogg, 1992, p. 262ff). The first such sounding of the interior of the continent was conducted on the central plateau of Queen Maud Land between 1951 and 1952 and discovered ice thicknesses of 2.4 km and bedrock elevation to be a couple of 100 m above or well below sea level (Robin, 1953, 1958). Due to the strong density contrast between ice and bedrock, gravity surveys such as those made by the Trans-Antarctic Expedition in 1955-58 were intended to complement ice thickness determinations from other sources such as seismic surveys, but required accurate determination of elevation that was proven difficult at the time (Fogg, 1992, p. 266ff). Yet, it was not until the International Geophysical Year (IGY; 1957-1958) that seismic soundings became common. The IGY included studies from a wide range of scientific fields such as glaciology, meteorology, geomagnetism, ionospheric physics, seismology and many others and expanded beyond the polar areas with all data being freely available to scientists around the world (Naylor et al., 2008). During this time, the number of stations rose from 20 to 48 with a summer population of around 5000 and a rise in winter population from 179 to 912 (Fogg, 1992, p. 147). It also sparked the foundation of the Scientific Committee on Antarctic Research (SCAR) by twelve countries, that was devoted to coordinate research in Antarctica. These countries signed the Antarctic Treaty one year later, stating that all territorial claims to Antarctica were frozen, neither accepted nor rejected, and peaceful use favoring scientific research with free exchange of information was promoted (Fogg, 1992, p. 176ff).

Advancements in radar echo soundings greatly improved knowledge about ice thickness and bedrock topography throughout the 1960s and 1970s. These soundings were also the

first to find evidence of subglacial lakes, with the biggest and most prominent being lake Vostok. The advent of satellites starting from the early 1970s provided data, accurate positioning and improved communication. However, early remote sensing missions did not provide full coverage in the Antarctic. For example, in 1978 SEASAT provided altimetry data only to 72°S. By 1965, substantial differences between East Antarctica (EANT) and West Antarctica (WANT) were determined. Crustal thicknesses of $\sim 40\,\mathrm{km}$ and bedrock topography mostly above sea level were found in EANT, while bedrock topography in WANT was found to be mostly below sea level with a thinner crust of $\sim 30\,\mathrm{km}$ with an abrupt transition along the Transantarctic Mountains. This general structure is still valid today (Fogg, 1992, p. 266ff). Clarkson (1983) first proposed a complex structure for WANT that is composed of 5 main tectonic plates with some built from microplates. This proposition was later supported by a British/US initiative including gravity and aeromagnetic surveys (Fogg, 1992, p. 261).

In recent years, scientific interest in Antarctica is on the rise. In 1993, 849 articles were published on the subject representing $\sim 0.06\,\%$ of all SCI articles of that year. This number rose to 2328 publications representing $\sim 0.17\,\%$ of all SCI articles in 2012. Increasing cooperation is visible in the average number of authors per article which rose from 3.0 to 5.3 in the same time span (Ji et al., 2014) as well as in newly developing efforts to bundle existing surveys to more comprehensive and consistent compilations in multiple disciplines of Antarctic research such as the Antarctic magnetic anomaly compilation (ADMAP) (Golynsky et al., 2001) and BEDMAP, an ice thickness and subglacial topographic model of Antarctica (Lythe et al., 2001). The BEDMAP Consortium represented the first attempt to provide a continent-wide digital model of bedrock topography and ice thickness in Antarctica. Both compilations received a recent update with ADMAP-2 (Golynsky et al., 2018) and BEDMAP-2 (Fretwell et al., 2013). International collaboration culminated with the 4th International Polar Year (IPY4) 2007-2008 with an estimated 50,000 researchers from over 60 nations working on 228 international projects. These projects included, among others, extensive airborne geophysical surveys using geomagnetic, gravity and ice-penetrating radar soundings, deep ice-core drilling and a substantial increase of geophysical observatories with over 80 new GPS and/or continuous seismic stations (Krupnik et al., 2011).

The IPY4 advanced the study of Antarctica in many fields. The new seismic data significantly contribute to tomographic models both on global and regional scales. Advances in surface wave tomography facilitated first continent-wide tomographic images (Danesi and Morelli, 2001; Ritzwoller et al., 2001) despite large gaps in receiver distribution, but propagation path density and resolution improved strongly with the new data (An et al., 2015b;

Schaeffer and Lebedev, 2013). The resulting models underline the fundamental difference between EANT and WANT with significantly lower velocities in WANT. Since seismic velocity strongly depends on temperature, this indicates a hotter lithosphere and upper mantle compared to EANT. In general, seismic studies have been used to infer surface heat flow in Antarctica (Shapiro and Ritzwoller, 2004; An et al., 2015a), because direct measurements are restricted to sparse deep borehole observations. Other studies rely on geomagnetic field data through calculations of the so-called magnetic Moho based on satellite missions such as CHAMP (Maule et al., 2005; Martos et al., 2017). These models however show striking differences in magnitude and pattern revealing large uncertainties of the results. The resolution of the gravity field greatly improved with the recent satellite missions GOCE and GRACE. With a maximum spatial resolution of spherical harmonics degree and order 280, GOCE offers crucial information in the mid to long wavelength of the gravity field. Due to its inclined orbit, it cannot cover the pole, leaving a polar gap of $\sim 7°$. With a higher altitude, the polar gap for GRACE is less than $1°$, yet provides a lower spatial resolution (Klokočník et al., 2017). In order to fill the polar gap and increase resolution, the satellite field models are often combined with ground-based observations (Förste et al., 2014). Scheinert et al. (2016) compiled ground-based, air-borne and ship-borne gravity data into a high resolution Antarctica-wide map covering 73% at a resolution of 10 km. Knowledge about crustal thickness has also greatly improved with the enhanced coverage of seismic stations (e.g. An et al., 2015b; Baranov and Morelli, 2013) and gravity models (Block et al., 2009) or combining both (Baranov and Morelli, 2013). However, large discrepancies in crustal thickness still remain between the studies.

All the innovations and improvements mentioned above allow us to decipher crustal and lithospheric structures hidden below the ice. Progress is constantly being made, showing that also EANT is divided into distinct tectonic blocks (Ferraccioli et al., 2011; Aitken et al., 2014; Jacobs et al., 2015; Ebbing et al., 2018, and many others). However, the exact tectonic structure is still left unknown today and further research is indispensable.

1.3. Structure of this thesis

The lithospheric and upper crustal architecture of Antarctica is still not sufficiently discovered. This thesis aims to take a step further in deciphering its structures and properties by providing a comprehensive model of the lithosphere and upper crust. The following chapters 4 to 6 encompass three independent studies in the form of peer-reviewed and published manuscripts. The connections between the studies are detailed in context passages. In

chapter 4, the effective elastic thickness T_e, a proxy for lithospheric strength, is calculated based on the coherence and admittance between the residual gravity field and the topography adjusted for density variations of ice, water and bedrock loads. Chapter 5 combines gravity with tomographic data to estimate temperature, density and composition variations of the lithosphere and upper mantle in an iterative approach. The third study in chapter 6 utilizes decompensative gravity anomalies to decipher upper crustal structures and infer sediment distributions hidden below the ice shield. Chapters 4 and 5 represent two independent studies characterizing the thermo-mechanical state of the lithosphere, allowing for comparison and cross-validation and building the basis for the calculations conducted in chapter 6. Due to the nature of published articles, theoretic explanations have to be kept short and concise and are often referred back to the publication the method originated in. In chapter 2, certain aspects that were not or only briefly explained in the respective theory section of chapters 4 through 6 are introduced or their explanation expanded. In chaper 3, the construction of the free air gravity field from two independent models and the corrections applied to it to obtain the residual (Bouguer) gravity field that is employed throughout this thesis are detailed.

2 Theory

Due to the cumulative nature of this thesis, the conducted studies are presented in the form of published articles, causing theoretical explanations to be kept short and concise. This chapter serves as a way to introduce theoretical aspects that have not explicitly been stated in the respective theory sections of each article and to expand on the explanation of only briefly mentioned aspects. Firstly, all three studies are based on the analysis of the gravity field corrected for surface loads. The way that these corrections were obtained has not been detailed in the articles, yet constitutes the basis for all calculations. Therefore, it is explained in section 2.1. In section 4.3, the calculation of T_e using the admittance and the coherence between the Bouguer gravity field and the topography with the fan wavelet method is described. This is complemented by section 2.2, which gives more details on the wavelet transform applied to both fields in the T_e calculations. In the study presented in chapter 5, an iterative approach combines temperatures and thermally induced densities obtained from seismic tomography with composition and composition induced densities estimated through joint inversion of residual gravity and topography. Section 2.3 expands on the mineral physics approach used in the temperature estimations that was kept very brief in chapter 5, while section 2.4 introduces new information on sensitivity and regularization of the joint inversion.

2.1. Gravity Modeling

In the course of this thesis, the main data source will be gravity disturbances, which is, in geophysics, often referred to as the gravity anomaly. They are defined as the magnitude of the gradient of the potential at a give point minus the magnitude of the gradient of the normal potential at the same point, which distinguishes it from the actual gravity anomaly, where the gradient of the normal potential on the Telluroid is subtracted (Barthelmes, 2013). Thus, the advantage is, that the gravity disturbance can be directly defined at the gravity observation point without the need of downward continuation (Hackney and Featherstone, 2003).

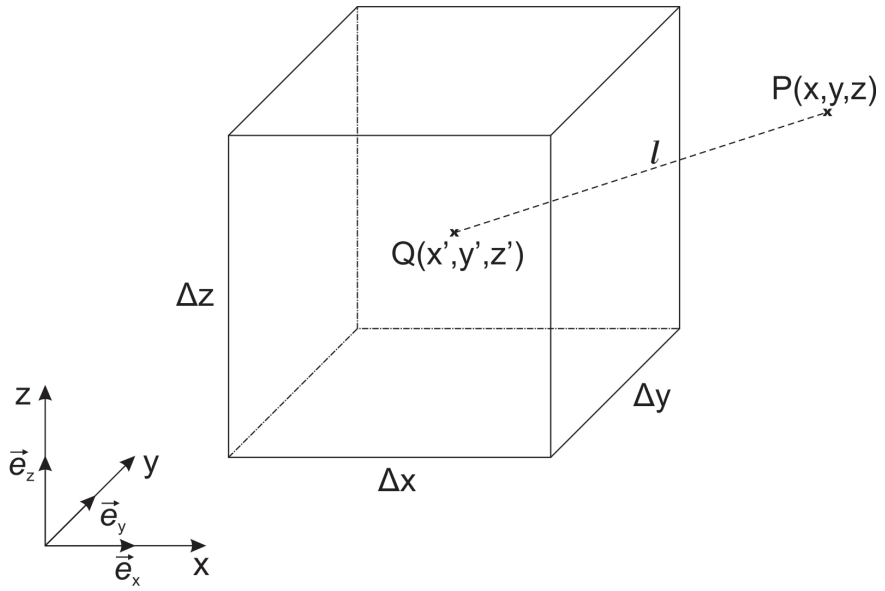

Figure 2.1.: Geometry of a rectangular prism (after Heck and Seitz, 2007)

The measured gravity field represents a combination of all Earth structures. Hence, if the effect of a specific layer is to be determined, in this case of the lithosphere, the effect of other known structures such as surface loads should be subtracted to reduce the non-uniqueness of the gravity inversion. For Antarctica, the surface loads are composed of the ice and water columns and topographic loads. Traditionally, the latter was corrected for using Bouguer correction which approximates the topography to an infinite planar Bouguer slab, taking into account the curvature of the Earth by reducing the slab to a spherical cap of the same thickness within 1.5° around each point and further terrain correction (Nowell, 1999). This might not always be a sufficiently accurate approximation of the complex shape of boundary layers at the Earth's surface. With increasing computational power, higher resolution terrain and density models can be used to quantify the gravity effect of surface loads by dividing the models into grid cells to calculate the effect of every cell on every point on the surface. In the following chapters, the model is divided into right rectangular prisms of homogeneous mass-density ρ as displayed in Fig. 2.1. Following Heck and Seitz (2007), the gravitational potential of a prism can be described as

$$u(x,y,z) = G\rho \int_{z_1}^{z_2} \int_{y_1}^{y_2} \int_{x_1}^{x_2} \frac{dx'dy'dz'}{l}\,, \tag{2.1}$$

where G is Newton's constant of gravitation, x_1, x_2, y_1, y_2, z_1 and z_1 are the coordinates of the corners of the prism and l is the euclidean distance between the computation point $P(x, y, z)$ and the center of the prism $Q(x', y', z')$

$$l = \sqrt{(x - x')^2 + (y - y')^2 + (z - z')^2}\,. \tag{2.2}$$

The gradient of the potential in z-direction $\nabla u = u_z \vec{e}_z$ depends on the partial derivative of u with respect to z which can be calculated through

$$u_z = -G\rho \int_{z_1}^{z_2} \int_{y_1}^{y_2} \int_{x_1}^{x_2} \frac{(z - z')dx'dy'dz'}{l^3}\,, \tag{2.3}$$

which can be solved analytically:

$$\begin{aligned} u_z = G\rho \sum_{i=1}^{2} \sum_{j=1}^{2} \sum_{k=1}^{2} (-1)^{i+j+k} \times \Big[& (x - x_i) \ln \left| \frac{y - y_j + w_{ijk}}{\sqrt{(z - z_k)^2 + (x - x_i)^2}} \right| \\ & + (y - y_j) \ln \left| \frac{x - x_i + w_{ijk}}{\sqrt{(z - z_k)^2 + (y - y_j)^2}} \right| \\ & - (z - z_k) \arctan \frac{(x - x_i)(y - y_j)}{(z - z_k) w_{ijk}} \Big]\,, \end{aligned} \tag{2.4}$$

with

$$w_{ijk} = \sqrt{(x - x_i)^2 + (y - y_j)^2 + (z - z_k)^2}\,. \tag{2.5}$$

The multiple ln and arctan operations are associated with high computation cost. Since the gravitational effect of surface loads decreases quickly with increasing distance, the prism approach is only applied within 2° of the computation point. Outside of this radius, grid cells are reshaped to wedge-shaped segments between two concentric cylinders (Fig. 2.2) of identical center of mass and total mass. Uncertainties caused by the reshaping of the grid cells were investigated and proven to be negligible in the past (Kaban et al., 1999). The gradient of the potential of such a cell in cylindrical coordinates can be described by equation 2.6 (see Watts, 2001):

$$u_z(\theta, r, z) = G\rho \int_{z_1}^{z_2} \int_{\theta_1}^{\theta_2} \int_{r_1}^{r_2} \frac{rz}{(r^2 + z^2)^{3/2}}\, \mathrm{d}z\, \mathrm{d}\theta\, \mathrm{d}r\,, \tag{2.6}$$

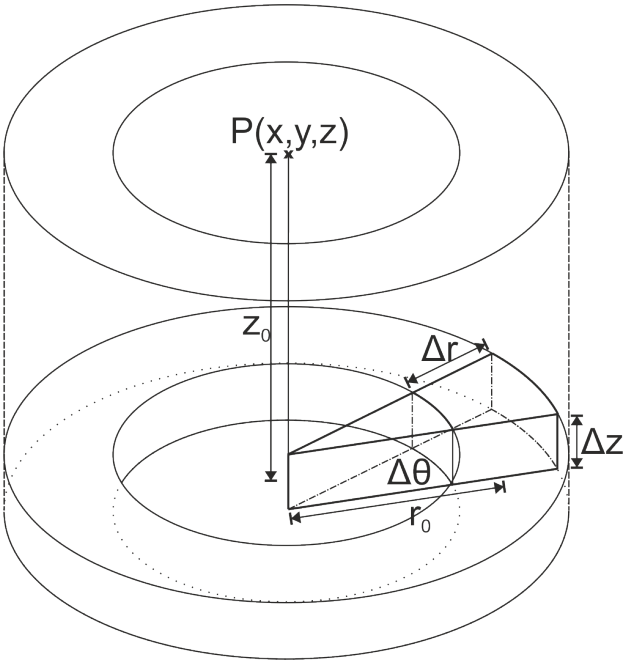

Figure 2.2.: Geometry of a wedge-shaped segment between two concentric cylinders

with the analytic solution

$$u_z = G\rho\Delta\theta \left(\sqrt{r_1 + z_1} + \sqrt{r_2 + z_2} - \sqrt{r_1 + z_2} - \sqrt{r_2 + z_1}\right) , \tag{2.7}$$

where $z_{1/2} = (z_0 \mp \frac{dz}{2})^2$, $r_{1/2} = (r_0 \mp \frac{dy}{2})^2$ and $\Delta\theta = \frac{dx}{r_0}$, with dx, dy and dz being the side-lengths of the original prism and r_0 and z_0 being the distance from the computation point to the center of the new cell in radial and vertical direction, respectively.

2.2. Fan wavelet method

The effective elastic thickness of the lithosphere T_e is the central parameter of interest in the first study (chapter 4) and serves as a proxy for the thermal and rheological properties of the lithosphere. It can be calculated using the admittance and coherence between the observed gravity field and the topography corrected for density differences between the different surface loads which is explained in detail in section 4.3. Traditionally, these quantities were determined in the spectral domain through Fourier transforms in a moving window or using multitapers for two-dimensional results (McKenzie and Fairhead, 1997). Hereby, the choice of the correct window size is crucially important: too small windows will not resolve long wavelength information while too big windows cannot yield T_e variation. This combined

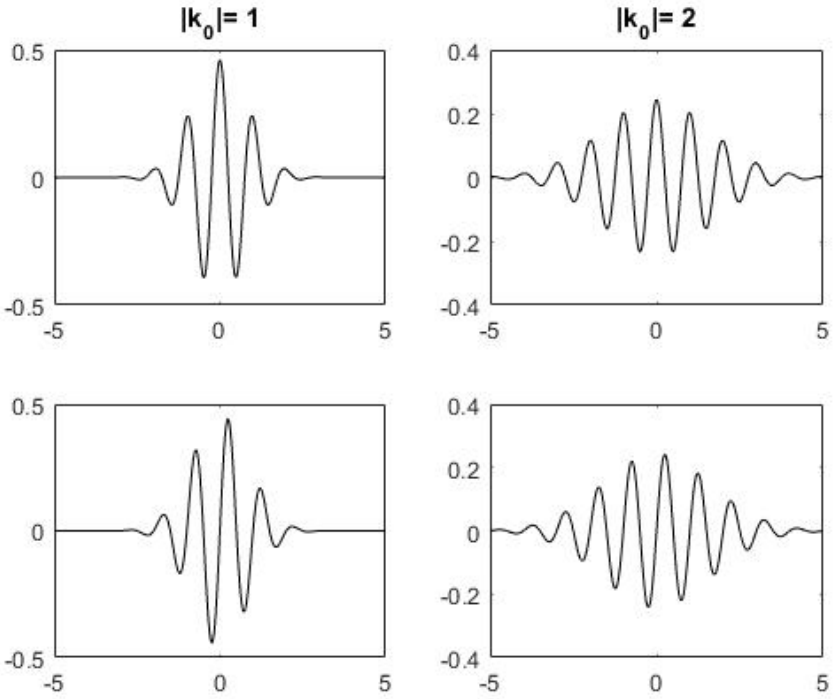

Figure 2.3.: Real part (top row) and imaginary part (bottom row) of the Morlet wavelet exemplary for two different central wavenumbers $|\mathbf{k}_0|$

with the bias introduced by multitaper, can produce unreliable T_e estimates (Swain and Kirby, 2003). Contrary to Fourier transforms yielding one power spectrum for an entire grid, continuous wavelet transforms (CWT) provide a way to calculate spectra on every grid point, allowing determination of coherence and admittance at each of those points (Kirby and Swain, 2004).
The CWT of a 2D space domain signal $g(\mathbf{x})$ is calculated by

$$\tilde{g}(s, \mathbf{x}, \theta) = \mathbf{F}^{-1}\left[\hat{g}(\mathbf{k})\hat{\psi}_{s\theta}(\mathbf{k})\right], \tag{2.8}$$

where $\tilde{g}(s, \mathbf{x}, \theta)$ are the wavelet coefficients, s and θ are the scale and azimuth of the wavelet, respectively, $\hat{g}(\mathbf{k})$ is the Fourier transform of the signal, $\hat{\psi}_{s\theta}(\mathbf{k})$ is the Fourier transform of the wavelet, $\mathbf{k} = (u, v)$ is the 2D wavenumber and $\mathbf{F}^{-1}$ indicates inverse Fourier transform (Kirby and Swain, 2011). For the study of isostatic processes, the resulting wavelet coefficients must be isotropic to avoid rotational bias in the T_e estimates and complex-valued to preserve phase information (Kirby and Swain, 2011).

The Morlet wavelet is a complex and anisotropic wavelet. In the space domain its form is

$$\psi(\mathbf{x}) = \mathrm{e}^{i\mathbf{k}_0\mathbf{x}}\mathrm{e}^{-|\mathbf{x}|^2/2}\,, \tag{2.9}$$

where $\mathbf{k}_0 = (|\mathbf{k}_0|\cos\theta, |\mathbf{k}_0|\sin\theta)$ and $|\mathbf{k}_0|$ is the central wavenumber (Kirby, 2005). An example for a Morlet wavelet is shown in Fig. 2.3. The associated Fourier transform is (Kirby, 2005)

$$\hat{\psi}(\mathbf{x}) = \mathrm{e}^{-\left[(u-|\mathbf{k}_0|\cos\theta)^2+(v-|\mathbf{k}_0|\sin\theta)^2\right]/2}\,. \tag{2.10}$$

Isotropy is realized through averaging over all azimuths. The name *fan* wavelet is derived from the superposition of Morlet wavelets for different scales ranging from the Nyquist frequency to the maximum dimension of the study area.

2.3. Upper mantle temperature determination

In the second study (chapter 5), tomographic velocities are used to infer upper mantle temperature variations taking into account anharmonic and anelastic properties. This section is an extension of chapter 5, section 3.2, providing more detail about the mineral physics equations this approach is based upon.

In order to calculate temperature variations, it is necessary to determine synthetic velocities for varying temperature, pressure and a given mantle composition that is varied for each iteration (compare iterative scheme combining temperature and density estimation in chapter 5, section 3.1). Those synthetic velocities matching closest to measured velocities are identified and the respective temperatures picked for every grid point. As the upper mantle composition, a peridotite consisting of four mineral phases with an ideal solid solution of Mg and Fe end-member species with varying percentages is assumed: Olivine (Ol) with forsterite and fayalite, orthopyroxene (OPX) with enstatite and ferrosilite, clinopyroxene (CPX) with diopside and hedenbergite and garnet (Gt) with pyrope and almandine. For Gt, a third Ca species (grossular) is assumed to comprise a constant proportion of 20%. The mantle composition is varied between the two end-members described in Table 2.1 and following Tesauro et al. (2014) according to the magnesium number Mg # ($100 \times \mathrm{Mg}/(\mathrm{Mg}+\mathrm{Fe})$) estimates from the previous iteration. For the initial thermal model, a uniform primitive mantle composition (Mg # = 89) is assumed.

In order to estimate synthetic velocities, the shear modulus and density for every mineral phase has to be calculated as a function of temperature and pressure using a mineral physics approach (Stixrude and Lithgow-Bertelloni, 2005). The density for each mineral phase is

Table 2.1.: Mineral fractions and Magnesium number Mg # ($100 \times \mathrm{Mg}/(\mathrm{Mg}+\mathrm{Fe})$) for the end-member compositions

	Ol (%)	OPX (%)	CPX (%)	Gt (%)	Mg #
Primitve Mantle	58.5	15	11.5	15	89
Depleted Mantle	69.5	21	4	5.5	94

calculated by

$$\rho_i = \frac{m}{V}\,, \tag{2.11}$$

where m is the molar mass and V is the molar Volume. Following Stixrude and Lithgow-Bertelloni (2005), the shear modulus for each mineral phase is given as

$$\begin{aligned}\mu_{\mathrm{i}} =&(1+2f)^{\frac{5}{2}}\left[\mu_0 + (3K_0G_0' - 5G_0)f + (6K_0G_0' - 24K_0 - 14G_0 + \frac{9}{2}K_0K_0')f^2\right] \\ &- \eta_{\mathrm{s}}\frac{E_{\mathrm{th}}(V,T) - E_{\mathrm{th}}(V,T_0)}{V}\,,\end{aligned} \tag{2.12}$$

where G_0 and K_0 are the shear modulus and bulk modulus, respectively, with the subscript 0 indicating STP conditions at zero pressure P_0 and room temperature ($T_0 = 300\,\mathrm{K}$), G_0' and K_0' are the respective pressure derivatives and f is defined as

$$f = \frac{1}{2}\left[\left(\frac{V_0}{V}\right)^{\frac{2}{3}} - 1\right]\,. \tag{2.13}$$

E_{th} is the vibrational energy

$$E_{\mathrm{th}}(V,T) = \frac{9nRT}{\theta/T)^3}\int_0^{\theta/T}\frac{x^3\mathrm{dx}}{e^x - 1} \tag{2.14}$$

which can be calculated using the Debye model (Jackson and Rigden, 1996) with R being the gas constant, n being the number of atoms per formula unit and θ being the Debye temperature

$$\theta = \theta_0 \exp\left(\frac{\gamma_0 - \gamma}{q}\right)\,. \tag{2.15}$$

Here, γ is the Grüneisen parameter

$$\gamma = \gamma_0\left(\frac{V}{V_0}\right)^q\,, \tag{2.16}$$

Table 2.2.: Properties of mantle mineral phases used in this study

Mineral	Species	Formula	V_0 [cm^3/mol]	K_0[GPa]	K_0'	θ_0[K]	γ	q	G_0[GPa]	G_0'	η_{s0}
Olivine	Forsterite	Mg_2SiO_4	43.6	129	4.2	809	0.99	2.1	81+31X_{Fe}	1.4	2.4
	Fayalite	Fe_2SiO_4	46.29			619	1.06	3.6			1.1
OPX	Enstatite	$Mg_4Si_4O_{12}$	125.35	109+20X_{Fe}	7.0	810	0.67	7.8	75+10X_{Fe}	1.6	2.4
	Ferrosilite	$Fe_4Si_4O_{12}$	131.88			680	0.67	7.8			1.1
CPX	Diopside	$Ca_2Mg_2Si_4O_{12}$	132.08	105+12X_{Fe}	6.2+1.9X_{Fe}	782	0.96	1.5	67+6X_{Fe}	1.7	1.6
	Hedenbergite	$Ca_2Fe_2Si_4O_{12}$	135.73			702	0.93	1.5			1.6
Garnet	Pyrope	$Mg_3Al_2Si_3O_{12}$	113.08	171+15X_{Fe}	4.4	823	1.01	1.4	92+7X_{Fe}	1.4	1.0
	Almanide	$Fe_3Al_2Si_3O_{12}$	115.43			742	1.10	1.4			2.2
	Grossular	$Ca_3Al_2Si_3O_{12}$	125.12			823	1.08	0.4			2.4

q its volume dependence which is assumed to be constant for each end-member (Stixrude and Lithgow-Bertelloni, 2005) and η_s its shear strain derivative

$$\eta_s = \eta_{s0}\left(\frac{V}{V_0}\right) . \tag{2.17}$$

The parameters used for these calculations for each end-member mineral phase are displayed in Table 2.2. The shear and bulk modulus and their pressure derivatives at STP conditions are taken from Cammarano et al. (2003), all other parameters displayed in Table 2.2 are taken from Stixrude and Lithgow-Bertelloni (2005). For a given mantle composition, the shear modulus and density of the individual phases are averaged using the volumetric percentage λ_i using the Voigt-Reuss-Hill averaging in case of the shear modulus:

$$\langle\rho\rangle = \sum \lambda_i \rho_i \tag{2.18}$$

$$\langle\mu\rangle = \frac{1}{2}\left[\sum \lambda_i \mu_i + \left(\sum \frac{\lambda_i}{\mu_i}\right)^{-1}\right] . \tag{2.19}$$

Subsequently, the anharmonic S-wave velocity can be calculated by

$$v_{s(anh)} = \sqrt{\frac{\langle\mu\rangle}{\langle\rho\rangle}} \tag{2.20}$$

(Stixrude and Lithgow-Bertelloni, 2005). Apart from the anharmonic effects, anelastic effects affect seismic velocities increasingly for increasing temperatures. Therefore, anelastisity has to be estimated to determine synthetic velocities for varying temperature and pressure conditions. The factor describing anelasticity can be described as follows according to

(Cammarano et al., 2003):

$$v_{\mathrm{s(anel)}} = 1 - \frac{Q_{\mathrm{s}}^{-1}}{2\tan\left(\frac{\pi a}{2}\right)}\,, \tag{2.21}$$

where Q_{s} is the S-wave quality factor

$$Q_{\mathrm{s}} = B\omega^{a}\exp\left(a\underbrace{\frac{H(P)}{RT}}_{g}\right)\,, \tag{2.22}$$

B is the normalizing factor, ω is the seismic frequency, a defines the frequency dependence of the attenuation, $H(P)$ is the activation enthalpy and g is the dimensionless temperature scaling factor. The values for B, a, g and ω are taken from the anelasticity models from Cammarano et al. (2003). Using the anelasticity parameter and the anharmonic velocity, the synthetic velocity can be calculated as

$$v_{\mathrm{syn}} = v_{\mathrm{s(anh)}} \cdot v_{\mathrm{s(anel)}}\,. \tag{2.23}$$

In order to finally estimate temperature variations from the input tomography models, synthetic velocities for distinct temperatures between 25°C and 1800°C are calculated with a 5°C spacing for pressures corresponding to the depths for which the seismic tomography velocities (v_{meas}) have been estimated. Thus, T for which $|v_{\mathrm{syn}}(T) - v_{\mathrm{meas}}|$ is minimal is determined in each grid cell.

2.4. Joint inversion of gravity and residual topography

Following the thermal modeling of the upper mantle, the residual gravity and residual topography fields are jointly inverted to obtain a 3D density model that is mainly caused by composition. This section complements chapter 5, section 3.3. Both fields depend on density variation, but react to variations of size and depth of the anomaly in fundamentally different ways (Kaban et al., 2015). This is shown in Fig. 2.4 for a single density anomaly in two different depths for varying spherical harmonics degrees. The inversion scheme (Kaban et al., 2015)

$$\min\{\|A\rho - g_{\mathrm{res}}\|^2 + k\|B\rho - t_{\mathrm{res}}\|^2 + \alpha\|\rho - \rho_{\mathrm{ini}}\|^2\}\,, \tag{2.24}$$

including both the gravity and the topography field can resolve the 3D density structure better than by inverting for the gravity field alone. Here, g_{res} and t_{res} are the residual

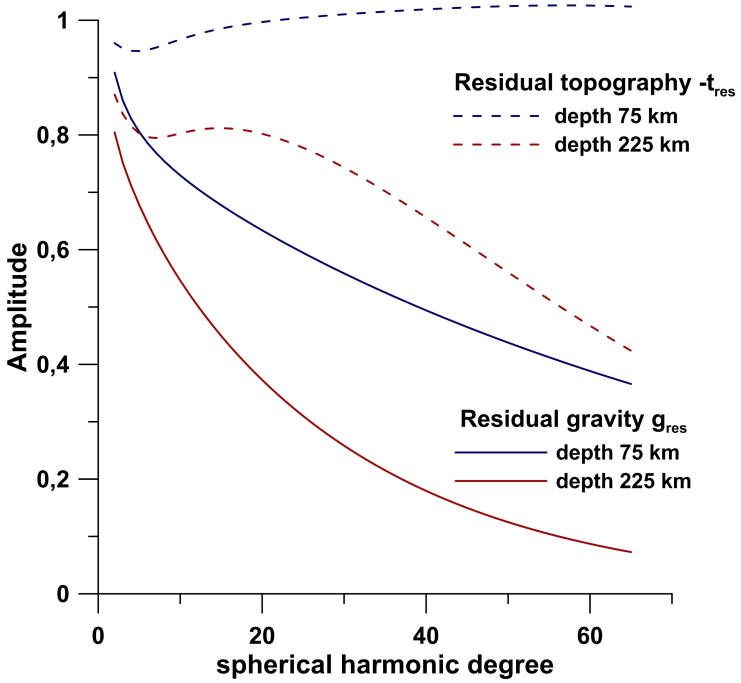

Figure 2.4.: Normalized gravity (solid line) and topography (broken line) kernels as a function of spherical harmonic degree for a single density anomaly in 75 km (blue) and 225 km (red) depth, respectively. The topography kernel is multiplied with -1 for better comparison with the gravity kernel

upper mantle gravity field and residual topography, respectively, $k = 2\pi G\rho_{\mathrm{t}}$ is a scaling coefficient normalizing the residual topography with respect to the gravity with ρ_{t} being the density of topography and A and B are integral operators converting densities ρ into gravity and topography perturbations in the spherical harmonic domain (Forte and Peltier, 1991). These integral operators are defined distinctly for varying depth layers and spherical degrees and an inverse solution can be calculated separately for each spherical coefficient with a maximum spherical degree of 180, reducing computation time notably. The third term in the inverse problem $\alpha\|\rho - \rho_{\mathrm{ini}}|^2$ describes regularization and is added to stabilize the inversion, since the operators A and B have no continuous inverse (Kaban, 2011). The regularization condition implies, that the density model should be close to a predefined initial density variation ρ_{ini}. If no initial model exists $\rho_{\mathrm{ini}} = 0$, the density perturbations should be minimal. The strength of the regularization is defined by the damping factor

$$\alpha = 2\pi G h D_{\mathrm{n}}\,, \tag{2.25}$$

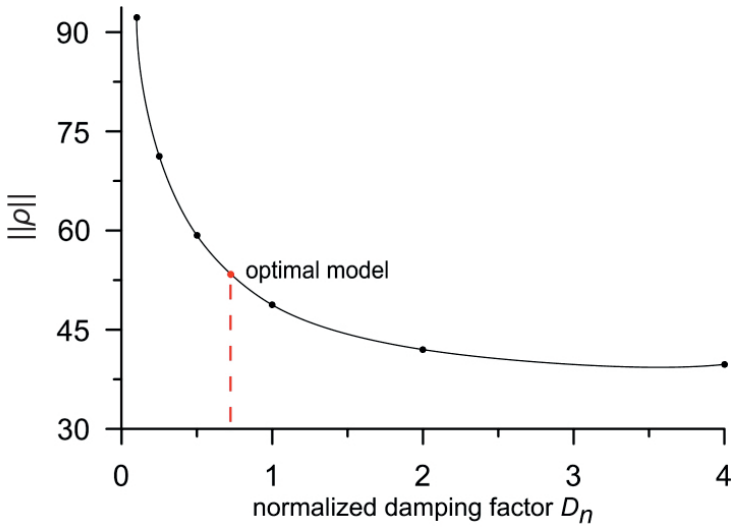

Figure 2.5.: Solution norm $||\rho||$ plotted against the normalized damping factor with the ideal value of D_n picked at the point of maximum curvature

where h is the thickness of the elementary cells used in the inversion and D_n is the normalized damping factor (Kaban et al., 2015). D_n is assigned using the L-curve criterion. The solution norm $||\rho||$ is plotted against D_n and the point of maximum curvature represents the optimal solution (Fig. 2.5). Lower D_n increases the noise level of the inversion while higher D_n introduces smearing. However, Kaban et al. (2015) have shown that the solution remains stable for a wide range of D_n and precise determination is not essential.

3 Initial gravity data

3.1. Free air gravity field

The free air gravity field used throughout this thesis is a combination of the models Eigen-6C4 (Förste et al., 2014) and AntGG (Scheinert et al., 2016) (Figs. 3.1 a and b, respectively). The Eigen-6C4 gravity disturbance dataset combines terrestrial and satellite data from GRACE, GOCE and LAGEOS with a maximum resolution of 2190 spherical harmonics degree and order. The actual resolution varies regionally and is controlled by the incorporated terrestrial data. For Antarctica, this is limited to a wavelength of around 200 km. The AntGG model is a compilation of ground-based, airborne and ship-borne gravity anomaly measurements over Antarctica and includes 13 million data points covering $\sim 73\%$ of the continent at resolution of 10 km. Especially over EANT, this model contains large gaps in data coverage distorting the long wavelength information. Therefore, we apply a Gaussian filter with a cut-off wavelength of 240 km (wavelength at which the amplitude of the filter is equal to half the maximum amplitude) before merging the fields resulting in a dominance of the satellite based observations at wavelength above 250 km and of the terrestrial data below wavelengths of 150 km with a gradual transition in between. The combined field is shown in Fig. 3.1 c.

As indicated above, the AntGG compilation was done in terms of gravity anomaly while the Eigen-6C4 gravity disturbance field is employed here. Förste et al. (2014) provide both disturbance and anomaly fields. The difference between these fields mainly depends on the geoid and can reach values of up to 20 mGal over Antarctica. The geoid, however, is a long-wavelength feature and the short wavelength component of the difference between anomaly and disturbance should be negligible. To test this hypotheses, the same gaussian high-pass filter that was applied to the AntGG model is now applied to the differential field, yielding values below ± 0.5 mGal over continental Antarctica, thus demonstrating the negligible effects of small wavelengths.

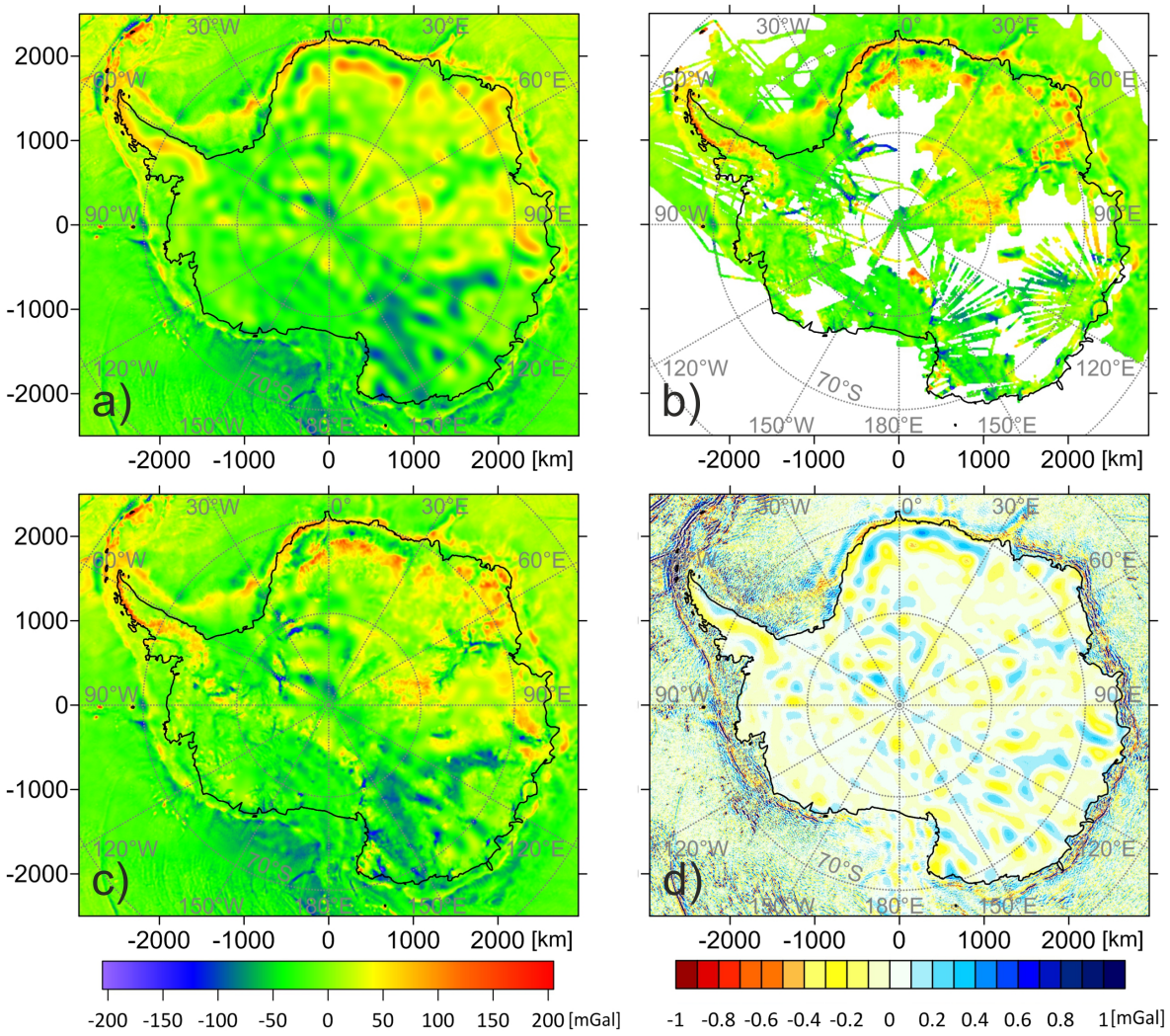

Figure 3.1.: Free air gravity field from a) Eigen-6C4 (Förste et al., 2014) and b) AntGG (Scheinert et al., 2016) and c) the combined field. d) Difference between the gravity anomaly and the gravity disturbance filtered with a Gaussian high-pass filter with a cut-off wavelength (half-amplitude) of 240 km.

3.2. Bouguer gravity field

Starting from the free air gravity field, corrections for topographic, ice and water load are calculated in order to obtain the residual or Bouguer gravity field. The first correction estimates the gravitational effect of bedrock topography (provided by Fretwell et al., 2013) variation from sea level with respect to a homogeneous reference model with a density of $\rho_{\text{crust}} = 2.7\,\text{g/cm}^3$. Depressions cause a negative gravity effect calculated with a density of $-\rho_{\text{crust}}$ while elevations above sea level are attributed a standard density of the uppermost

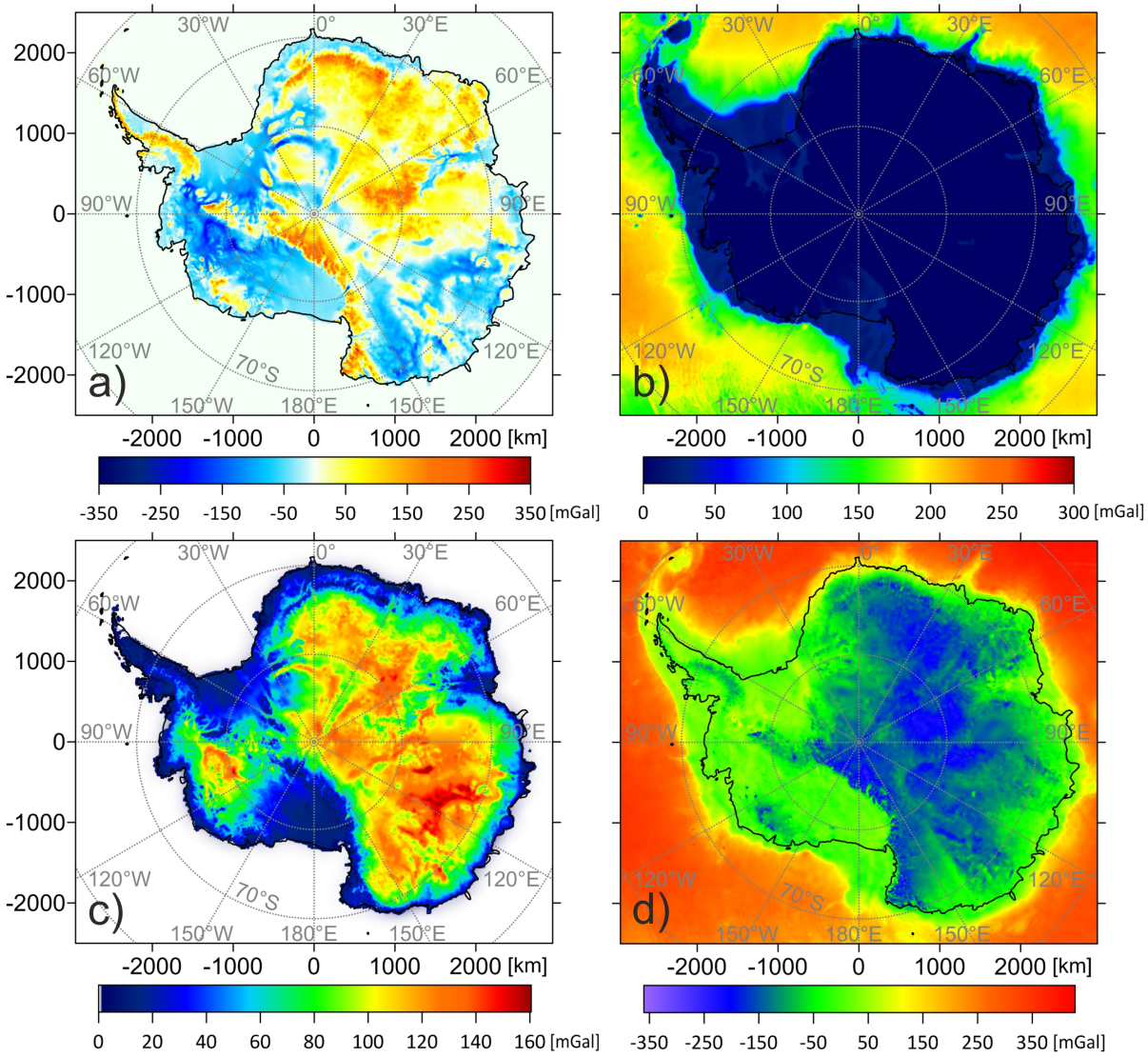

Figure 3.2.: Gravity effect of a) the topographic variation with respect to the homogeneous reference model, b) the water column with respect to the homogeneous reference model and c) the ice load. d) Bouguer gravity field.

crust of $\rho_{\text{topo}} = 2.67\,\text{g/cm}^3$. This correction is calculated for the continental area, while variations of the bathymetry are incorporated in the water load correction. For the latter, a distinction has been made for water columns on the continent and below ice shelves and the ice free ocean. For the ocean, the boundaries of the water column are the bathymetry (provided by Fretwell et al. (2013) south of 60°S and by (Schaffer et al., 2014) north of 60°S) and sea level, otherwise the boundaries are defined as bedrock topography and the lower ice boundary, which was calculated by subtracting the ice thickness from the surface elevation from Fretwell et al. (2013). To calculate the gravity deficit as compared to the

homogeneous crustal model, the effective density of this load is estimated by $\rho_{\text{water}} - \rho_{\text{crust}}$ with $\rho_{\text{water}} = 1.03\,\text{g/cm}^3$ which is the standard density for salt water. The continental freshwater detected at the current resolution is restricted to lake Vostok. Hence the error on the gravity correction caused by assuming purely salt water is negligible. Lastly, the total gravity effect of the ice load is calculated. The density of ice is temperature and pressure dependent. Reasonable temperature variations in Antarctic glacial settings range from -10 to -50°C (Price et al., 2002) translating to densities between $\rho_{\text{ice,min}} = 0.918\,\text{g/cm}^3$ and $\rho_{\text{ice,max}} = 0.922\,\text{g/cm}^3$. The uncertainties in the gravity field, calculated assuming the extreme densities as a constant throughout the entire ice layer, are $\pm 0.35\,\text{mGal}$. They are thus negligible and a constant density of $\rho_{\text{ice}} = 0.920\,\text{g/cm}^3$ is applied. The estimated corrections for topography, water and ice (displayed in Fig. 3.2 panels a, b and c, respectively) are subsequently subtracted from the free air gravity field and the final Bouguer field (Fig. 3.2 d) is obtained.

4 | Variations of the effective elastic thickness reveal tectonic fragmentation of the Antarctic lithosphere

Chapter abstract

To this day, little is known about thermal and rheological properties of the Antarctic lithosphere. We derive the effective elastic thickness T_e as a proxy for these parameters by using ice thickness, bedrock topography and a combination of new satellite and high resolution terrestrial gravity data. Cross-spectral analysis based on the fan wavelet technique was employed to calculate T_e variations by means of admittance and coherence techniques. Our results confirm a clear tectonic division of Antarctica with predominantly high values in East Antarctica (EANT) ($T_e \sim$ 60-80 km) and low values in West Antarctica (WANT) ($T_e \sim$ 5-20 km). For the Transantarctic Mountains separating these provinces, we found T_e to be around 10 km along the whole chain which is comparable to WANT. Apart from this general division, we found fragmentation of the lithosphere within these provinces. Especially EANT doesn't represent a single lithospheric block but shows strong variations of T_e. The highest values are found around the Aurora Subglacial Basin ($T_e \sim$ 90 km) and in Dronning Maud Land ($T_e \sim$ 80 km). The minimum value of T_e within EANT ($\sim$ 15 km) is found in the Lambert Graben. Such a low value can be associated with active rifting in the Permian-Triassic, strong localized erosion or possibly the effect of a Cenozoic mantle plume. According to the coherence calculations, the weak zone extends to the Gamburtsev Subglacial Mountains (GSM), showing a distinct decrease of T_e to 25-30 km. Thus, this weak channel divides the previously mentioned strong blocks. However, the admittance analysis gives relatively high values ($T_e \sim$ 70 km) for the GSM. Based on the analysis of the wavelength-dependent admittance and coherence results and misfits for several principal locations, we give some preference to the coherence based values. The admittance estimations could also be significantly biased by internal density heterogeneity of the lithosphere, as already discussed in several studies.

Published manuscript:
Chen, B., Haeger, C., Kaban, M. K., Petrunin, A. G. (2018). Variations of the effective elastic thickness reveal tectonic fragmentation of the Antarctic lithosphere. *Tectonophysics*, 746. http://dx.doi.org/10.1016/j.tecto.2017.06.012.

Contribution of Carina Haeger to article:

- Data collection and preparation
- Calculation of the Bouguer gravity and adjusted topography fields including all corrections
- Visualization, interpretation and discussion of results
- Writing of the sections Abstract, Introduction, Tectonic setting, Initial data, Discussion and Conclusion
- Creation of figures

4.1. Introduction

Knowledge of the thermal state and mechanical properties of the lithosphere is important for many geophysical applications (Burov and Diament, 1995). The thermo-mechanical structure of the lithosphere controls to a large extent the initiation and evolution of tectonic deformation processes (e.g. Willett et al., 1985). These parameters are also required to model vertical motions at the Earth's surface, such as glacial isostatic adjustment (GIA), which are of prime importance in monitoring the mass balance of the Antarctic ice sheet (e.g. Ramillien et al., 2006). Furthermore, it has been recently demonstrated that the dynamical behavior of the Greenland ice shield depends not only on the climate changes but is also controlled to a large extent by the heat flow from the Earth interior (Petrunin et al., 2013b). Therefore, this effect can also be important for Antarctica. To this day, Antarctica remains one of the least studied and understood areas in the world. Due to its remoteness and the thick ice sheet covering over 99% of its surface (Lythe et al., 2001), geophysical in-situ measurements are still sparse over large parts of the continent. Heat flow measurements, which are the only direct constraints on the thermal state of the lithosphere, are extremely sparse in Antarctica, especially in the areas covered by the ice shield (e.g. Fisher et al., 2015). The thermal structure of the lithosphere can also be evaluated based on seismic tomography models (Goes et al., 2000; Tesauro et al., 2015) and magnetic anomalies (Maule et al., 2005). However, such models provide very low resolution for the Antarctic upper mantle. Basically, they only show the difference between the relatively hot West Antarctica (WANT) and the cold East Antarctica (EANT) with very thick lithosphere (Schaeffer and Lebedev, 2013; Shapiro and Ritzwoller, 2004).

Only few studies were conducted to study the lithospheric structure in the internal areas of Antarctica. Seismic studies for example have been hindered by the sparsity of stations and very low intracontinental seismicity (Reading, 2007), yet improvements in surface wave studies provide S-velocity maps both on global (Schaeffer and Lebedev, 2013) and continental scales (An et al., 2015b). The latter also present information on Moho depth from their surface wave tomography as well as from a compilation of previous seismic studies. An Antarctic-wide collection of gravity data has been presented by Scheinert et al. (2016). All of these studies image very well the difference between the younger WANT and the older EANT, while smaller structures within the East Antarctic Craton remain unresolved.

Alternatively, there exists an integrative parameter, namely the effective elastic thickness of the lithosphere (T_e), which directly relates to the thermal state and rigidity of the lithosphere and can be used as their proxy. T_e is the thickness of an idealized elastic plate that

would bend as the lithosphere under the same applied loads and can be used to quantify the lithospheric strength (Burov and Diament, 1995). This parameter can be determined based on cross-spectral analysis of the gravity field and surface topography by applying various methods (Forsyth, 1985; Watts, 2001). Only a limited number of studies on T_e have been conducted in Antarctica, which still provide very inconsistent estimates of this parameter. Based on old and sparse data sets, Stern and ten Brink (1989) have already found indications for a transition from weak lithosphere in West Antarctica (WANT) to stronger lithosphere in East Antarctica (EANT) underneath the Transantarctic Mountains (TAM). ten Brink et al. (1997) analyzed a 312-km-long traverse in the hinterland of the TAM and fitted the topography and gravity with a 85-km-thick elastic plate. Furthermore, Yamasaki et al. (2008) studied T_e by looking at the half-wavelength of the TAM and determined a very high value of this parameter (~ 100 km). Ferraccioli et al. (2011) calculated variations of T_e in the Gamburtsev province in East Antarctica and found that T_e varies from 30 km to more than 70 km in the central part. Recent satellite missions provide us with homogeneous gravity models on global scales (Förste et al., 2014), including areas where no other data are available. These data can be supplemented by detailed terrestrial and airborne gravity measurements, which have been strongly expanded during the last decade (Scheinert et al., 2016). Furthermore, Fretwell et al. (2013) collected data from various methods to compile improved grids of ice thickness, surface and bedrock elevation within Bedmap2, providing clearer images of the surface loading of the Antarctic continent. On the basis of these models, cross-spectral analysis of topography and gravity data can be used to determine T_e. McKenzie et al. (2015) have made estimates of T_e for Antarctica based on these data. However, they are limited to a comparison between East and West Antarctica. Also, the obtained values (21 km and 5 km, correspondingly) are unusually low for continental areas. In this study, we determine variations of the effective elastic thickness over the Antarctic continent by using modern methods based on a fan wavelet technique for the cross-spectral analysis of the gravity data and the topography adjusted for variations of the bedrock topography and ice thickness (Kirby and Swain, 2011, 2004). We determine both admittance and coherence of the Bouguer gravity anomalies and topography. A comparison of these results allows to resolve reliable features of the T_e pattern and compare them with the Antarctic tectonics and dynamic behavior of the ice shield.

4.2. Tectonic setting of Antarctica

Antarctica is almost entirely covered by thick ice caps with a maximum thickness of nearly 4500 m (Fig. 4.1). Large parts of its bedrock topography lie below sea level (Fretwell et al., 2013). At large scales, it can be divided into two main tectonic provinces: The stable Precambrian shield of East Antarctica and West Antarctica, an amalgamation of thinner and hotter Cenozoic crustal micro-blocks (Dalziel and Elliot, 1982). EANT can be divided into several subglacial orogens and rifts. The largest structure is a subglacial plateau spanning 0°-100°E with its highest elevations in the Gamburtsev Subglacial Mountains and Dronning Maud Land (Fretwell et al., 2013). Enderby Land is characterized by only slightly less topography, yet previous studies of crustal thickness (e.g. O'Donnell and Nyblade, 2014) show it to reach similar values as the Basin structures of Wilkes and Aurora Subglacial Basins. The latter is a topographic depression lying up to 1 km below sea level, that may have been formed by erosion (Close et al., 2007). The Prince Charles Mountains are characterized by intraplate deformation and igneous intrusions caused by the collision of East and West Gondwanaland (565-500 Ma) (Veevers, 2007). The plateau is interrupted by a late Mesozoic transtensional basin that holds Antarctica's largest glacier, the Lambert Glacier (Reading, 2006).

WANT is a complex of several younger (mostly Jurassic and Cretaceous) microcontinental blocks that have moved independently from each other and from EANT until their amalgamation in the Cenozoic (Veevers, 2012). The most notable western Antarctic feature is the West Antarctic Rift System (WARS), a 750-1000 km wide crustal rift structure that mostly lies below sea level. Extension took place in two distinct phases: a prolonged period of broadly distributed extension in the Cretaceous and a phase of more focused extension in the Paleogene (Huerta and Harry, 2007). It is bordered by Mary Byrd Land, a region characterized by intraplate volcanism (Hole and LeMasurier, 1994).

EANT and WANT are separated by the Transantarctic Mountains (TAM), a 3500 km long and 200 km wide mountain chain with elevations of up to 4500 m (Morelli and Danesi, 2004). The TAM are the largest non-contractional mountains in the world (ten Brink et al., 1997) and their exact formation remains controversial. Three main uplift mechanisms have been suggested in the past: 1) Thermally driven uplift due to high temperatures at shallow depths (e.g. Smith and Drewry, 1984) possibly related to mantle plume activity (e.g. Behrendt, 1999); 2) Mechanically driven uplift caused by flexure and uplift of a broken plate edge (e.g. ten Brink and Stern, 1992); 3) The TAM were suggested to be the remaining margin of a Mesozoic West Antarctic plateau that collapsed (e.g. Huerta and Harry,

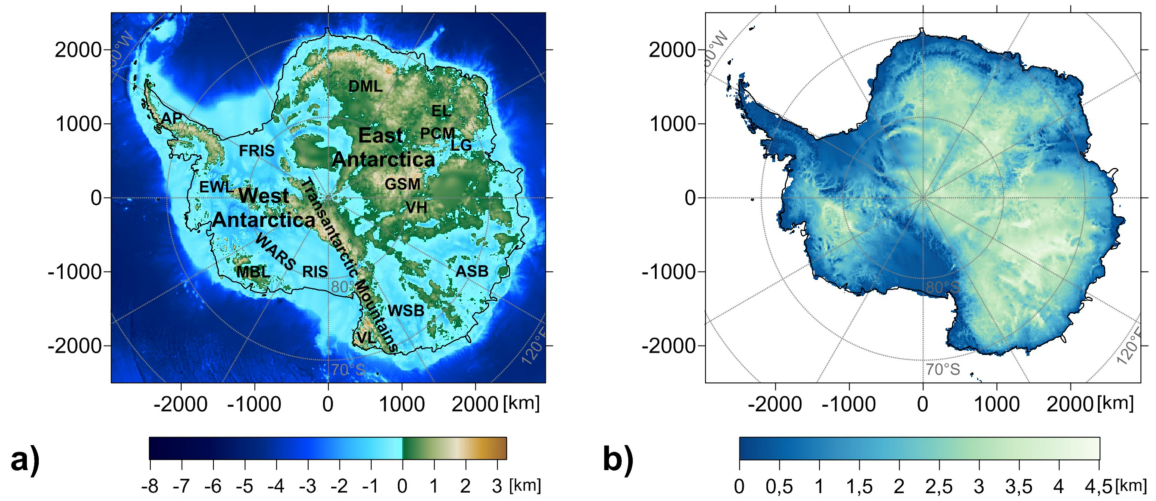

Figure 4.1.: **(a)** Bedrock topography of Antarctica (Fretwell et al., 2013) and bathymetry of the surrounding ocean (Schaffer et al., 2014). Key tectonic units: AP, Antarctic Peninsula; ASB, Aurora Subglacial Basin; DML, Dronning Maud Land; EL, Enderby Land; EWL, Ellsworth Land; FRIS, Filchner-Ronne Ice Shelf; GSM, Gamburtsev Subglacial Mountains; LG, Lambert Glacier; MBL, Marie Byrd Land; PCM, Prince Charles Mountains; RIS, Ross Ice Shelf; VH, Vostok Highlands; VL, Victoria Land; WARS, West Antarctic Rift System; WSB, Wilkes Subglacial Basin. **(b)** Ice thickness.

2007). Recently, van Wijk et al. (2008) proposed a new, rifting related model for the formation of the TAM. Since Antarctica occupied a central position in Gondwana prior to its breakup in the late Mesozoic, the Antarctic plate is bordered by eight different plates. The plate boundaries almost entirely consist of mid-ocean ridges (Torsvik et al., 2010) creating deviatoric stresses that eventually cause the onset of rifting near the border of East and West Antarctica. The West Antarctic Rift System develops in the weak crust of WANT while the stronger EANT craton remains unaffected. Rifting causes crustal material from the central rift zone to be transported towards its margins, its eastern margin being characterized by much higher (cratonic) strength. Hence, the crustal material accumulates at the boundary causing thickening and uplift of the crust. The van Wijk model also predicts the formation of a surface depression adjacent to the mountain chain that might correspond to the Wilkes Subglacial Basin. In this case, the Wilkes Subglacial Basin would be a flexural basin without crustal thinning.

4.3. Method

In order to estimate the effective elastic thickness, the lithosphere is commonly modelled as a thin elastic plate overlying a fluid substratum. It is bending under various types of loads, producing the gravity anomalies that we observe at the surface. The amount of the plate deflection primarily depends on an integrative parameter, namely the flexural rigidity D, which is related to the effective elastic thickness (T_e) as

$$D = ET_e^3/[12(1-\sigma^2)] \tag{4.1}$$

where E is the Young's modulus (100 GPa) and σ is the Poisson's ratio (0.25). Analysis of the relationship and correlation (admittance or coherence, correspondingly) between the observed adjusted topography (topography, water, ice and, to some extent, density variations in the upper crust) and gravity anomalies in the spectral domain could provide potential information on the isostatic compensation of the lithosphere and give a measure of its mechanical properties (e.g. Audet and Mareschal, 2007; Watts, 2001).

The admittance method was first developed by Dorman and Lewis (1970), subsequently it was applied and improved in many studies (e.g. Banks et al., 1977; Forsyth, 1985; Mckenzie and Bowin, 1976; Watts, 1978). A major development was contributed by Forsyth (1985) who combined the effects of surface and subsurface loading into the admittance method, and developed the coherence technique for T_e estimations. Currently, the admittance and coherence methods are widely used to estimate T_e of the lithosphere (e.g. Audet and Bürgmann, 2011; Chen et al., 2015a,b; McKenzie et al., 2015; Pérez-Gussinyé and Watts, 2005; Watts, 2001). In this study, we apply both Bouguer admittance and coherence methods to estimate variations of T_e over Antarctica.

A number of different techniques have been used to calculate the spectrum of gravity and topography for admittance and coherence. The two extensively used ones are multitapers (McKenzie and Fairhead, 1997; Pérez-Gussinyé et al., 2004, 2009; Simons et al., 2000) and wavelets (Kirby and Swain, 2004, 2011; Stark, 2003). The multitaper technique was developed by Thomson (1982). It deals with spectral leakage well and has a good performance at short wavelengths, but its efficiency is restricted by the window size (Kirby, 2014). The wavelet technique was introduced in flexural studies by Stark (2003) and Kirby and Swain (2004). Due to the wavelets' localization and variable spatial and wavenumber resolution, this method permits to locate T_e patterns with different wavelength, avoiding the restrictions due to the size of the computing window (Kirby, 2014). Furthermore, Kirby and Swain (2011) adjusted the central wavenumber of the Morlet wavelet to recover T_e variations with

variable spatial resolution. The fan wavelet technique (Kirby and Swain, 2011, 2004) is applied to calculate the gravity and topography auto-spectra and the cross-spectrum in this study.

4.3.1. Calculation of admittance with the fan wavelet method

The admittance $Q(\mathbf{k})$ is the transfer function that relates the observed gravity anomaly and topography in the wavenumber domain (Dorman and Lewis, 1970),

$$B(\mathbf{k}) = Q(\mathbf{k})H(\mathbf{k})\,. \tag{4.2}$$

where $B(\mathbf{k})$ and $H(\mathbf{k})$ are the spectral representations of the Bouguer gravity anomalies and topography, $\mathbf{k}$ is the two-dimensional wavenumber.
In practice, the calculated admittance is averaged in some wavelength interval to supress the effect of noise. In the wavelet method, the admittance for Bouguer gravity anomaly and topography is defined as (Kirby and Swain, 2008):

$$Q_{\mathrm{obs}}(s,\mathbf{x}) = \frac{Re\left[\langle B_{s\mathbf{x}\theta} H^{*}_{s\mathbf{x}\theta}\rangle_{\theta}\right]}{\langle H_{s\mathbf{x}\theta} H^{*}_{s\mathbf{x}\theta}\rangle_{\theta}}\,, \tag{4.3}$$

where B and H are the wavelet transforms of the Bouguer gravity and topography, respectively; $Re[\,]$ represents the real part. s and θ are the scale and azimuth of the Morlet wavelet, * indicates complex conjugation; $\langle\,\rangle_{\theta}$ represents the averaging over azimuth. The wavelet admittance is a function of position $\mathbf{x}$ and wavelet scale s, which is related to an equivalent 1D Fourier wavenumber ($|\mathbf{k}|$) by the relation $|\mathbf{k}| = |\mathbf{k}_0|/s$, where $|\mathbf{k}_0|$ is the central wavenumber of the Morlet wavelet (Kirby and Swain, 2011).
This parameter $|\mathbf{k}_0|$ controls the spatial resolution of the T_{e} variations. The lowermost number provides better spatial resolution, but the result could be biased by noise. By increasing $|\mathbf{k}_0|$, we can supress the effect of noise, however the resolution is decreasing. Therefore, it is necessary to choose a reasonable compromise. We use four values of the central wavenumber $|\mathbf{k}_0|$ given by Kirby and Swain (2011), 2.668, 3.081, 3.773 and 5.336, which correspond to the Morlet wavelets with the first sidelobes 1/16, 1/8, 1/4 and 1/2 of the central amplitude correspondingly. Since the wavelet transform is performed at a series of scales (s), the wavelength interval is determined by the choice of scales. Here we choose the scales spanning a dyadic grid from the Nyquist wavelength to the maximum dimension of the study area (Kirby, 2005; Kirby and Swain, 2011).
To model the admittance for specific values of T_{e}, a two-layer crustal model with both

surface and subsurface loads is constructed under the assumption that the initial loading processes are statistically independent (Forsyth, 1985). Both the subsurface load and the compensation interface are assumed to be at the Moho depth (z_m), which corresponds to the Crust1.0 model (Laske and Masters, 2013). The combined-loading predicted Bouguer admittance is given by Kirby (2014):

$$Q_\mathrm{pre}(s,\mathbf{x}) = \frac{\mu_\mathrm{T} k_\mathrm{T} + \mu_\mathrm{B} k_\mathrm{B} f^2 r^2}{k_\mathrm{T}^2 + k_\mathrm{B}^2 f^2 r^2}\,, \tag{4.4}$$

where f is the ratio of the internal load to the surface load, defined by (Forsyth, 1985; Kirby and Swain, 2011)

$$f^2(s,\mathbf{x}) = \frac{\langle |W_\mathrm{i}^2| \rangle_\theta}{r^2 \langle |H_\mathrm{i}^2| \rangle_\theta}\,, \tag{4.5}$$

$r = (\rho_\mathrm{c} - \rho_\mathrm{f})/(\rho_\mathrm{m} - \rho_\mathrm{c})$, ρ_c and ρ_m are the crustal ($2800\,\mathrm{kg/m^3}$) and mantle ($3300\,\mathrm{kg/m^3}$) densities, respectively; ρ_f is the density of the overlying fluid, $\rho_\mathrm{f} = 0$ for the continent or $\rho_\mathrm{f} = 1030\,\mathrm{kg/m^3}$ for the ocean; $\mu_\mathrm{T}, k_\mathrm{T}, \mu_\mathrm{B}$ and k_B are the wavenumber-dependent coefficients that relate the initial surface and subsurface loads and the observed Bouguer gravity anomaly and topography (Kirby and Swain, 2011),

$$\begin{pmatrix} B \\ H \end{pmatrix} = \begin{pmatrix} \mu_\mathrm{B} & \mu_\mathrm{T} \\ k_\mathrm{B} & k_\mathrm{T} \end{pmatrix} \begin{pmatrix} W_\mathrm{i} \\ H_\mathrm{i} \end{pmatrix}\,, \tag{4.6}$$

$$\begin{gathered} k_\mathrm{B} = -(\rho_\mathrm{m} - \rho_\mathrm{c})/\Phi \\ k_\mathrm{T} = 1 - (\rho_\mathrm{c} - \rho_\mathrm{f})/\Phi \\ \mu_\mathrm{B} = 2\pi G(\rho_\mathrm{m} - \rho_\mathrm{c})[1 - (\rho_\mathrm{m} - \rho_\mathrm{c})/\Phi] e^{-|\mathbf{k}| z_\mathrm{m}} \\ \mu_\mathrm{T} = 2\pi G(\rho_\mathrm{m} - \rho_\mathrm{c})[-(\rho_\mathrm{c} - \rho_\mathrm{f})/\Phi] e^{-|\mathbf{k}| z_\mathrm{m}} \\ \Phi = D|\mathbf{k}|^4/g + \rho_\mathrm{m} - \rho_\mathrm{f} \end{gathered}\,,$$

where W_i and H_i are the fan wavelet transforms of the initial surface and subsurface loads, respectively; g is the gravitational acceleration ($9.8\,\mathrm{m/s^2}$); G is the gravitational constant ($6.67\,\mathrm{e}^{-11}\,\mathrm{m^3 kg^{-1} s^{-2}}$); z_m is the Moho depth.

4.3.2. Calculation of coherence with the fan wavelet method

The coherence is a measure of the phase relationship between the gravity anomalies and topography. Using the wavelet cross-spectrum of these fields and the auto-spectra of topography and gravity averaged over azimuth, the observed wavelet coherence is given by

(Kirby and Swain, 2011, 2006)

$$\gamma^2_{\text{obs}}(s,\mathbf{x}) = \frac{\left(Re\left[\langle B_{s\mathbf{x}\theta} H^*_{s\mathbf{x}\theta}\rangle_\theta\right]\right)^2}{\langle B_{s\mathbf{x}\theta} B^*_{s\mathbf{x}\theta}\rangle_\theta \langle H_{s\mathbf{x}\theta} H^*_{s\mathbf{x}\theta}\rangle_\theta}\,, \tag{4.7}$$

where we use the square of the real part of the coherency after Kirby and Swain (2009, 2011), and still name it"coherence" for simplicity. When the Bouguer gravity and topography are uncorrelated, the phases of the cross-spectra are randomly distributed and averaging cancels their coherence, whereas when the Bouguer gravity and topography are correlated, the averaging yields a high coherence (Audet and Mareschal, 2007; Kirby, 2014).

In the coherence and admittance methods, we assume that the gravity and topography are a result of flexural compensation of surface and subsurface loads. "Gravitational noise" may occur, which is that part of the observed gravity filed not considered in the model (McKenzie, 2003; Kirby and Swain, 2009). For Antarctica, the "gravitational noise" may stem from the correlated internal loads without topographic expression (e.g. Kirby and Swain, 2009). In addition, the unrecovered surface topography after the removal of Quaternary ice loads (Pérez-Gussinyé et al., 2004) may also be a potential source of noise in the coherence and admittance analysis.

Reliability of the estimates with the coherence method can be evaluated by calculating the normalized squared imaginary part (NSIP) of the free air coherency ($\overline{\Gamma}^2_{\text{F,I}}$) (Kirby and Swain, 2009):

$$\Gamma_{\text{F}}(s,\mathbf{x}) = \frac{\langle G_{s\mathbf{x}\theta} H^*_{s\mathbf{x}\theta}\rangle_\theta}{\langle G_{s\mathbf{x}\theta} G^*_{s\mathbf{x}\theta}\rangle^{\frac{1}{2}}_\theta \langle H_{s\mathbf{x}\theta} H^*_{s\mathbf{x}\theta}\rangle^{\frac{1}{2}}_\theta}\,,\ \overline{\Gamma}^2_{\text{F,I}} = \frac{\left(\text{Im}\left[\Gamma_{\text{F}}\right]\right)^2}{|\Gamma_{\text{F}}|^2}\,, \tag{4.8}$$

where $G_{s\mathbf{x}\theta}$ is the wavelet transform of the free air gravity anomalies; Im[] represents the imaginary part. As suggested by Kirby and Swain (2009), the coherence (and consequently T_{e}) may be biased by "gravitational noise", when the maximum value $\overline{\Gamma}^2_{\text{F,I}}$ around the Bouguer transition wavelength exceeds 0.5. The Bouguer transition wavelength corresponds to an often-sharp rollover from 1 to 0 in a coherence curve, and is strongly dependent on the magnitude of T_{e} (Kirby, 2014).

Similar to the admittance method, the same two-layer crustal model with both surface and subsurface loads is employed to model the predicted coherence. Using the assumption of uncorrelated loading (Forsyth, 1985), the predicted coherence can be determined as (Kirby and Swain, 2011):

$$\gamma^2_{\text{pre}}(s,\mathbf{x}) = \frac{\left(\mu_{\text{T}} k_{\text{T}} + \mu_{\text{B}} k_{\text{B}} f^2 r^2\right)^2}{\left(\mu^2_{\text{T}} + \mu^2_{\text{B}} f^2 r^2\right)\left(k^2_{\text{T}} + k^2_{\text{B}} f^2 r^2\right)}\,. \tag{4.9}$$

The observed admittance or coherence are compared with the model predictions for a range of T_e values. T_e is obtained by minimizing the root-mean-square difference between the observations and model predictions at each grid node of the study area. In order to suppress the increased effect of noise at short wavelengths, the misfit (ϵ) is weighted by the inverse of the equivalent Fourier wavenumber (Kirby and Swain, 2006, 2008), and is calculated through

$$\epsilon = \sqrt{\frac{\sum_{i=1}^{N} \left[\gamma_{\text{obs}}^2(|\mathbf{k}|_i)\right]^2 / |\mathbf{k}|_i^2}{\sum_{i=1}^{N} 1/|\mathbf{k}|_i^2}}\,, \tag{4.10}$$

where N is the number of the equivalent wavenumber.

4.4. Initial data

The free air gravity disturbances were obtained combining the models Eigen-6C4 (Förste et al., 2014) and AntGG (Scheinert et al., 2016). The Eigen-6C4 dataset combines terrestrial and satellite (GRACE, GOCE and LAGEOS) data to a global grid with a resolution of up to 2190 spherical harmonics degree/order. However, actual horizontal resolution of this data set depends on the used terrestrial data, which for Antarctica doesn't exceed 200 km, therefore limiting it to the satellite only solution. AntGG is a compilation of ground-based, airborne and shipborne gravity anomaly measurements over Antarctica providing short wavelength gravity information not present in the satellite data. It consists of 13 million data points covering $\sim$73% of the continent at 10 km resolution. However, this data set contains many gaps causing its long-wavelength part to be biased. Therefore, we combine it with the satellite based gravity maps. Above the wavelength 250 km, chiefly the satellite model is used, below 150 km, the data from AntGG are employed with gradual transition within this wavelength interval.

In order to obtain the Bouguer gravity anomalies (Fig. 4.2a), we remove the gravity effect of the topography, ice and water columns from the free air gravity disturbances. Information on surface elevation, bed elevation and ice thickness up to 60°S were provided by Bedmap2 (Fretwell et al., 2013), bathymetry north of 60°S is taken from the global bathymetry grids from RTopo-2 (Schaffer et al., 2014). The gravity effect is calculated within a 222.4 km (2°) radius around each point. All spherical effects are taken into account in the calculations (Kaban et al., 2016a). The reference density of the upper crust is $\rho_t = 2670\,\text{kg/m}^3$ and the density of water is $\rho_w = 1030\,\text{kg/m}^3$. Since the density of ice is temperature-pressure dependent, and ice temperatures vary strongly with depth within the ice shield, we tested the influence of these variations on the gravity effect. Within reasonable temperature variations

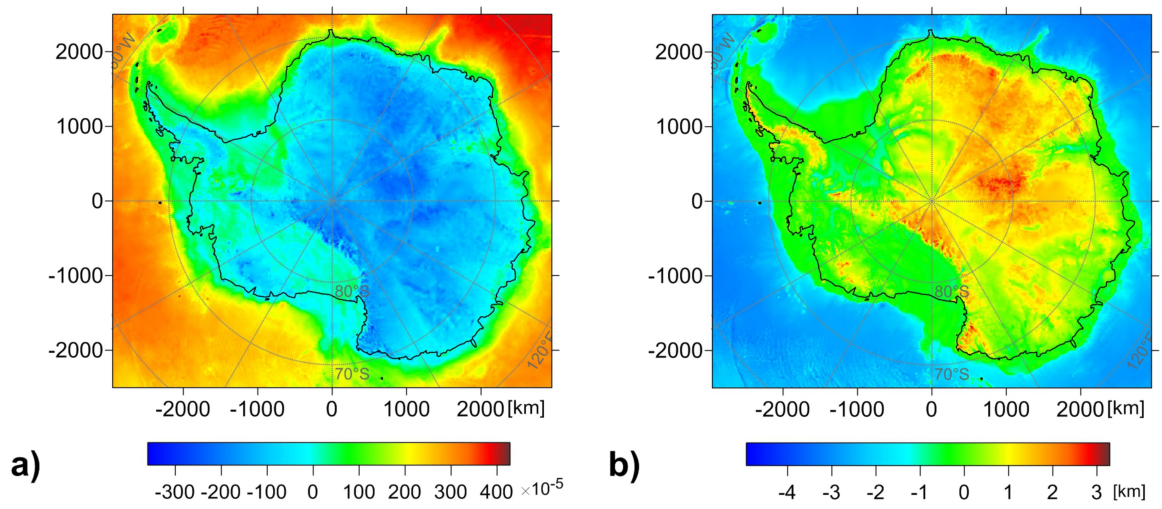

Figure 4.2.: **(a)** Bouguer gravity anomalies. **(b)** Adjusted topography combining variations of the bedrock elevation, ice and water.

in Antarctic glacial settings of $\sim$ -10 to -50°C (Price et al., 2002), we found the gravity variation to be negligible ($\pm 0.35 \times 10^{-5}\,\mathrm{m/s^2}$) thus assuming from here on out the constant average ice density $\rho_\mathrm{i} = 920\,\mathrm{kg/m^3}$. Based on these values, we have also calculated the adjusted topography (H) by compressing the ice and water columns to the standard density of the crust:

$$H = h_\mathrm{b} + \frac{\rho_\mathrm{w}}{\rho_\mathrm{t}} h_\mathrm{w} + \frac{\rho_\mathrm{i}}{\rho_\mathrm{t}} h_\mathrm{i} \tag{4.11}$$

where h_b is the bedrock topography, h_w and h_i are the heights of the water and ice, respectively.

All data grids were produced using Polar Stereographic Projection (Snyder, 1987) based on the WGS84 ellipsoid with true scale at 71°S with a grid size of 10 by 10 km. The calculated adjusted topography is shown in Fig. 4.2b.

4.5. Results

Variations of T_e of the Antarctic lithosphere were estimated using the fan wavelet method to determine the admittance and coherence of the Bouguer gravity anomalies and adjusted topography. As described above, we have used four values of the central wavenumber $|\mathbf{k}_0|$, 2.668, 3.081, 3.773 and 5.336.

4.5.1. Spatial variations of T_e by coherence inversion

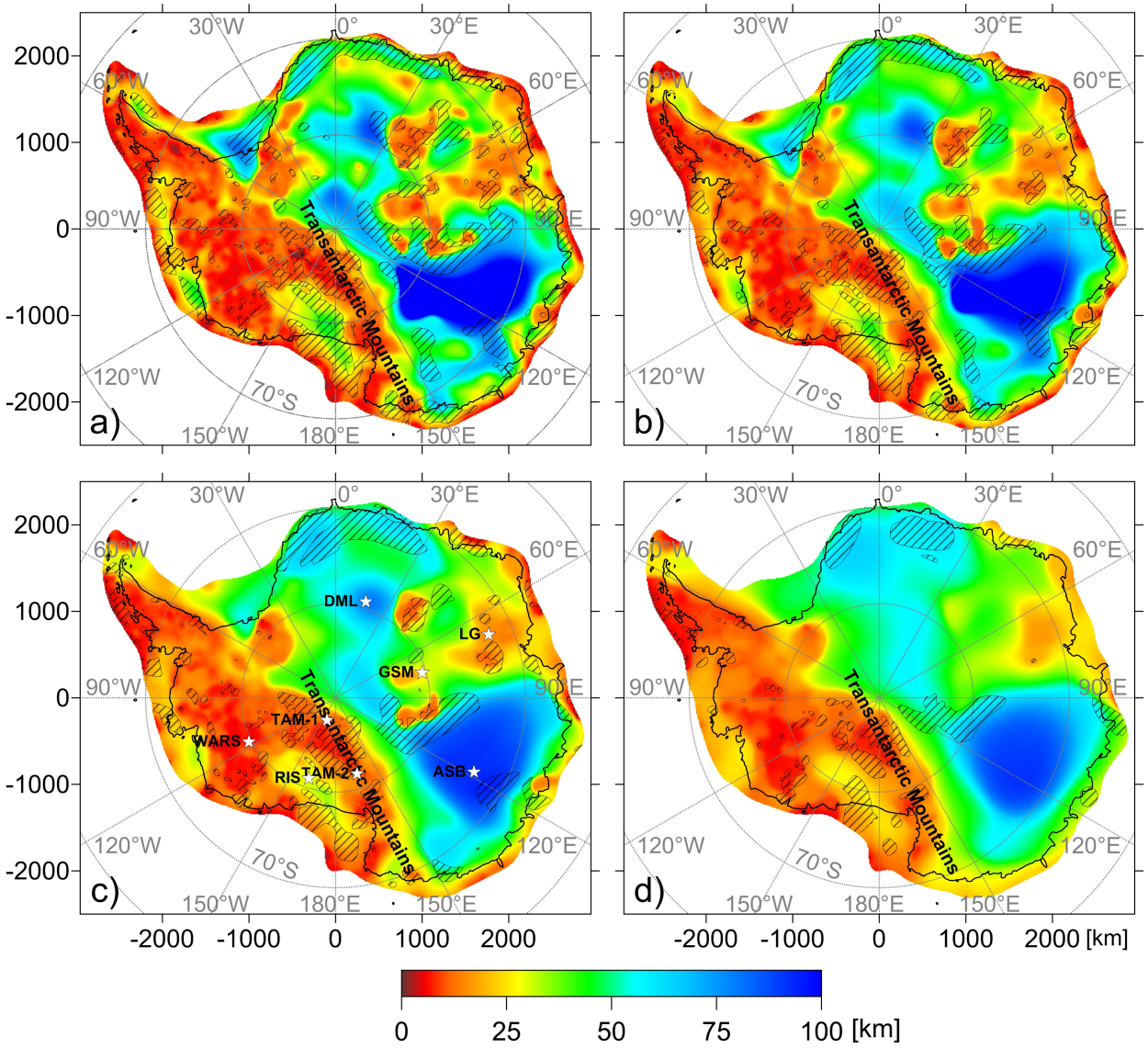

Figure 4.3.: Variations of T_e obtained with the coherence method. Four different values of the central wavenumber of the Morlet wavelet $|\mathbf{k}_0|$ are considered: **(a)** 2.668, **(b)** 3.081, **(c)** 3.773 and **(d)** 5.336. The hatched patterns show the areas, where the maximum value of the normalized squared imaginary part of the free air coherency (Eqs. 4.7) is larger than 0.5 and the results might be biased. The white stars show locations, for which the calculation results are demonstrated. Abbreviations as in Figure 4.1.

Variations of the effective elastic thickness computed with the coherence method for different

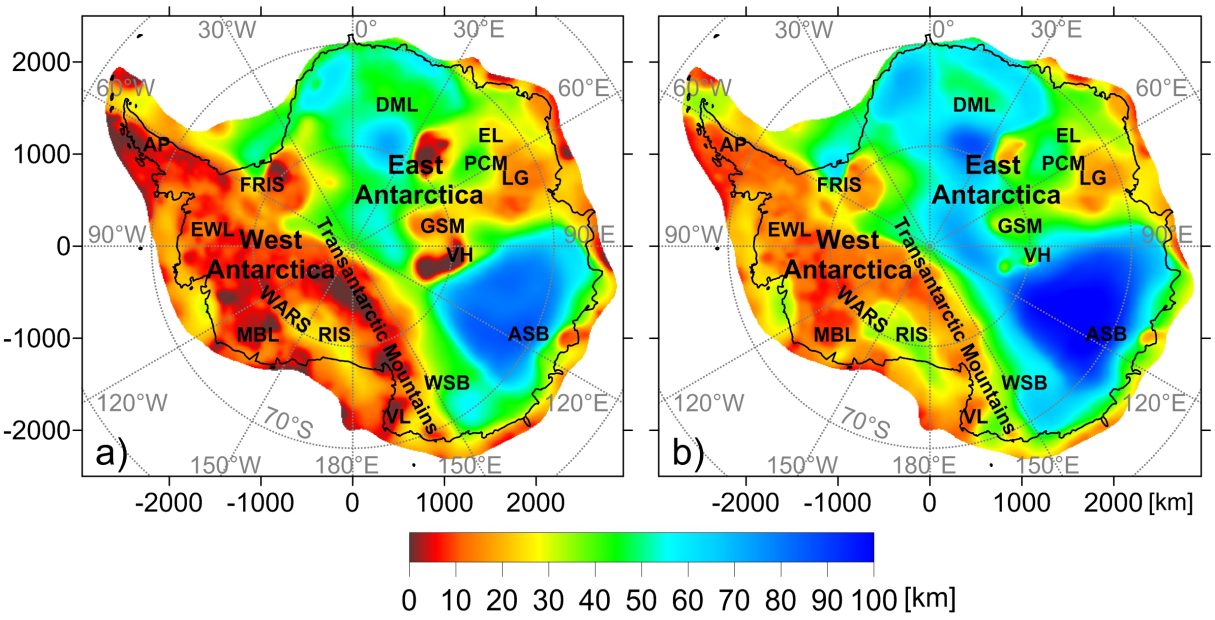

Figure 4.4.: Lower **(a)** and upper **(b)** boundaries of the T_e estimation with the coherence method for $|\mathbf{k}_0| = 3.773$. These values correspond to the misfit $\epsilon = 1.05\epsilon_{\min}$ (Watts et al., 2006). Abbreviations as in Figure 4.1.

values of the central wavenumber of the Morlet wavelet $|\mathbf{k}_0|$ are shown in Fig. 4.3. All figures are consistent. One of the dominant features is the division of Antarctica along TAM. West Antarctica including TAM is chiefly characterized by a very weak lithosphere, while to the east, high values of T_e are prevalent excluding the area around the Lambert Graben (LG). Later on, we discuss specific patterns of these variations. The maximum spatial resolution of the obtained map corresponds to the minimum central wavenumber of the Morlet wavelet $|\mathbf{k}_0| = 2.668$. However, the patterns of this map are unstable, so a lot of the small anomalies likely represent artefacts because the lower $|\mathbf{k}_0|$ wavelets indicate greater uncertainty on the T_e estimation (Kirby and Swain, 2011). This is also confirmed by a relatively wide area, where the parameter $\overline{\Gamma}^2_{F,I} > 0.5$ and the results are unreliable (Fig. 4.3a). In contrast, the maximum $|\mathbf{k}_0| = 5.336$ provides a stable and smooth map, but amplitudes of the main anomalies are damped and some of them disappear (Fig. 4.3d). The two intermediate values give a reasonable compromise (Fig. 4.3b-c). Possible uncertainty of the T_e estimations is assessed based on the misfit curve. Following Watts et al. (2006) we determine lower and upper limits of T_e for the misfit, which exceeds the minimum by 5% ($\epsilon = 1.05\epsilon_{\min}$). The upper and lower values for $|\mathbf{k}_0| = 3.773$ are shown in Fig. 4.4.

In order to discuss reliability of the results, we analyze the coherence and other parameters calculated in eight points (Fig. 4.3c) for several key features of Antarctica. The graphs

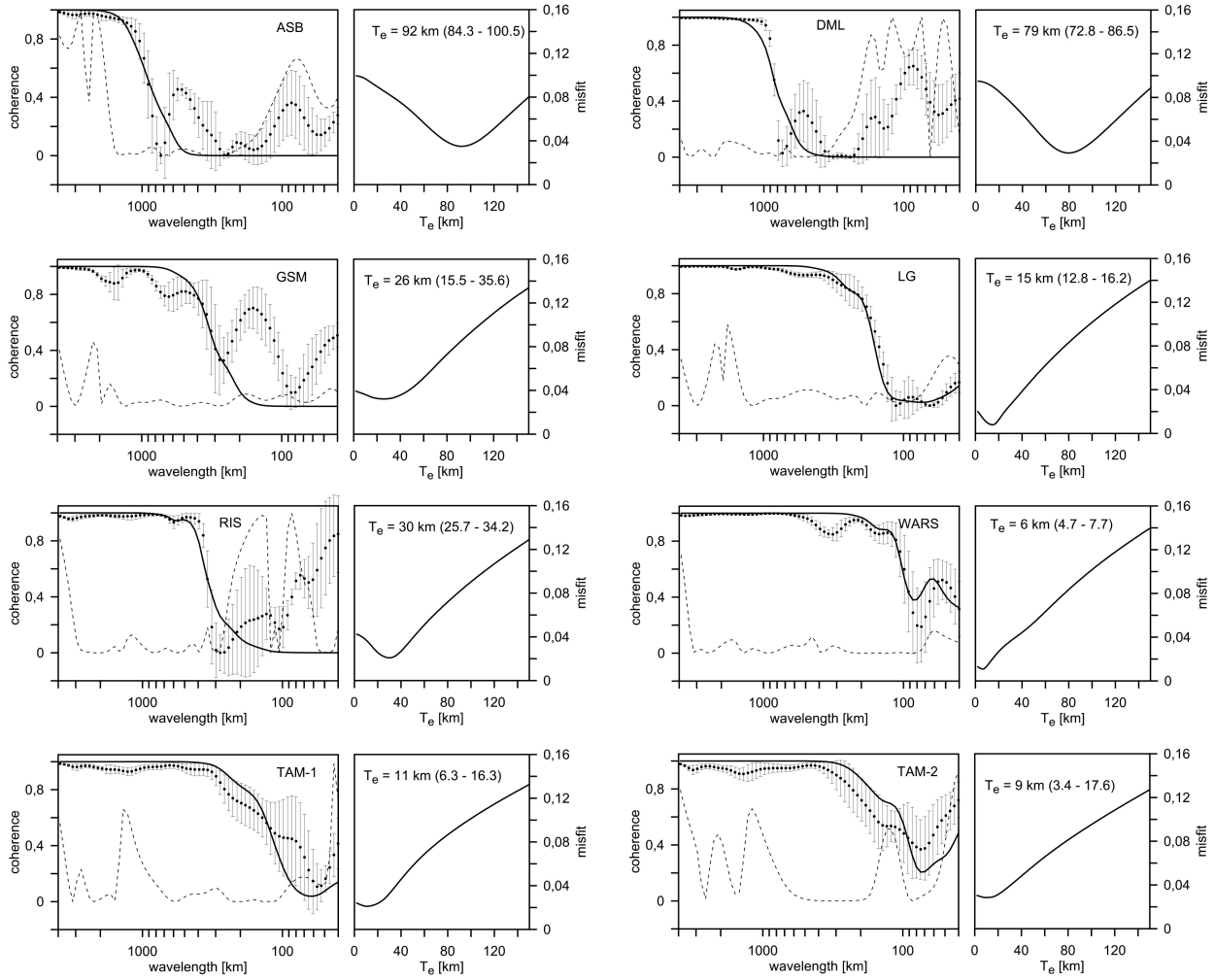

Figure 4.5.: Coherence and misfit for eight locations in Antarctica (Fig. 4.3c) for $|\mathbf{k}_0| = 3.773$. Left graphs show coherence depending on the wavelength. Points with uncertainties represent observations, solid line – predicted (model) values, and dashed line – the parameter NSIP (Eqs. 4.8). Right graphs show misfit depending on T_e. The lower and upper boundaries corresponding to the misfit $\epsilon = 1.05\epsilon_\mathrm{min}$ are shown in parentheses. Abbreviations as in Figure 4.1.

showing the observed and predicted coherence with other parameters of the calculations are shown in Fig. 4.5. The maximum $T_\mathrm{e} = 92\,\mathrm{km}$ is found for ASB. This value corresponds to a drop of the coherence at the wavelength 800-900 km. The misfit demonstrates a pronounced minimum, which supports that the result is reliable. Below 200 km, the parameter NSIP quickly increases with decreasing wavelength. Therefore, the quality of the initial data is limited to this wavelength (ca. 100 km in the spatial domain). Similar results are obtained for DML, which represents another area with high $T_\mathrm{e} = 79\,\mathrm{km}$. In contrast, for GSM in

the center of Antarctica we obtain a relative low $T_e = 26\,km$. Moreover, this is likely the maximum value corresponding to the first decrease of the observed coherence, since the misfit is weighted by the inverse of the equivalent Fourier wave number. This is clearly demonstrated by the misfit curve, which is almost flat below 26 km up to zero. This proves that the lithosphere is relatively weak in the area of GSM compared to DML and ASB. The weakest lithosphere in East Antarctica is found in the area of LG ($T_e = 15\,km$). This value is very well determined, in particularly due to the high quality data, which is demonstrated by near zero NSIP until the wavelength $\sim 50\,km$.
One of the new findings is the low value of T_e (9-11 km), which is determined for TAM. The quality of the data is not as good as in the previous cases, but the range of acceptable T_e values (approximately from 0 to 25 km) indicates that this structure is really characterized by a relatively weak lithosphere. Consequently, also the fits between observed and predicted coherence values are not as clear as in other locations, since the fitted decrease is slightly steeper than the overall decrease for both examples. Yet, the fitted curve still remains within the observation uncertainties in almost all points. These results are consistent for the whole TAM chain. Therefore, TAM can be linked to the weak lithosphere of West Antarctica. The last one is chiefly characterized by $T_e < 15\,km$, as demonstrated for the West Antarctic rift system ($T_e = 6\,km$, Fig. 4.5). The only exclusion is the area of the Ross Ice Shelf (RIS), for which relatively high values of $T_e = 20 - 40\,km$ are obtained. As it is visible from Fig. 4.5-RIS, the abrupt decrease of the coherence at the wavelength $\sim 300\,km$ indicates that this result is trustworthy.

4.5.2. Spatial variations of T_e by admittance inversion

Variations of T_e computed with the admittance method are shown in Fig. 4.6. In general, they are consistent with the coherence results. We also observe a clear difference between the western and eastern parts of Antarctica and TAM are also linked to the weak lithosphere of WANT. However, there exist several principal differences, for example, GSM are characterized by high values of T_e similar to DML and ASB. The upper and lower values of T_e, which are determined based on the misfit curves for $|\mathbf{k}_0| = 3.773$, are shown in Fig. 4.7. We analyze the calculated admittance for the same eight locations as for the coherence results. The observed and predicted admittance with the misfit for eight selected points (Fig. 4.6c) are shown in Fig. 4.8. It is clear from these graphs as well as from the comparison of the lower and upper limits of T_e (Figs. 4.4 and 4.7) that the admittance determinations of T_e are more uncertain than corresponding estimates with the coherence method. Comparison of Figs. 4.5 and 4.8 reveals that the Bouguer coherence inversion provides a better

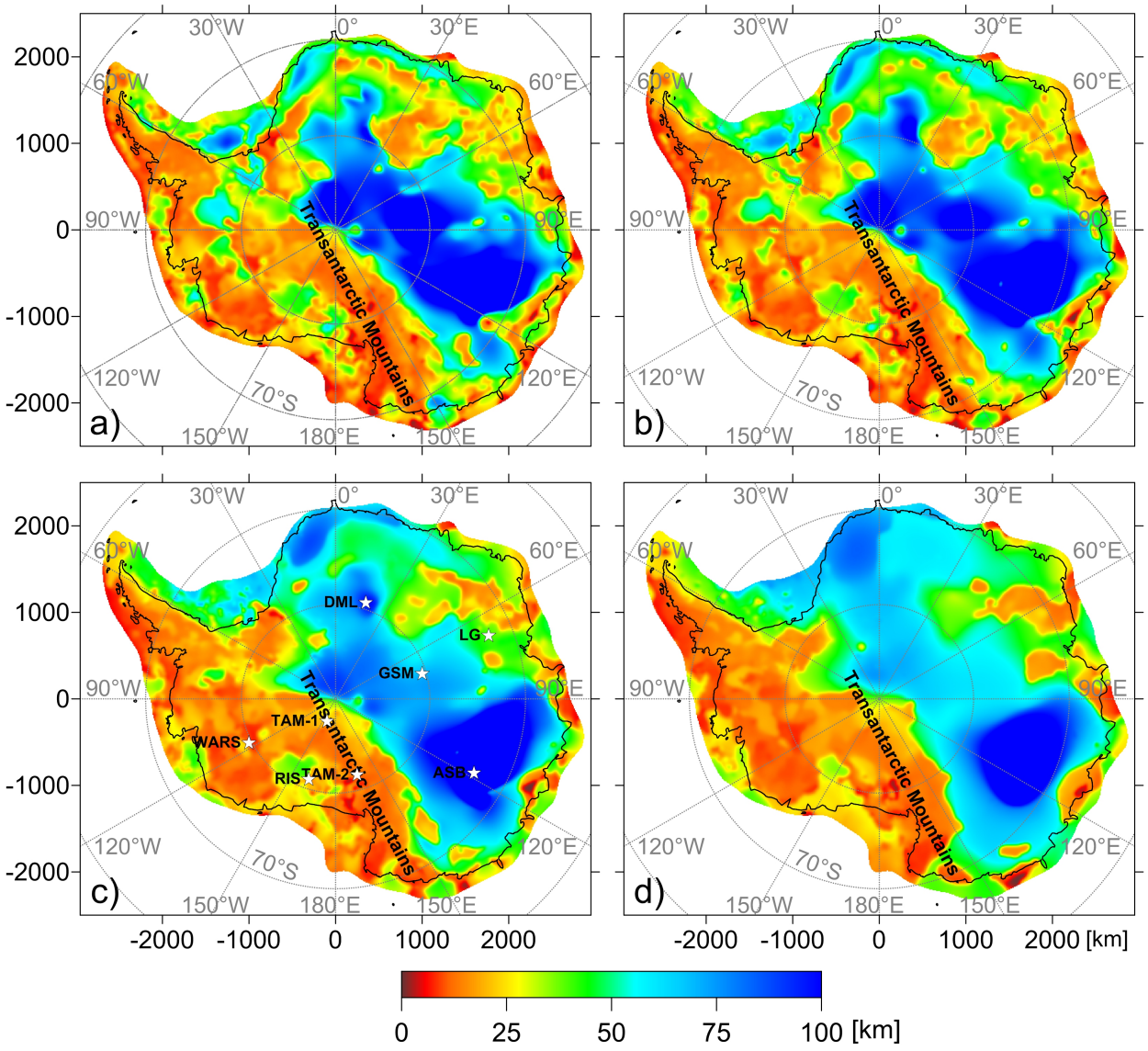

Figure 4.6.: Variations of T_e obtained with the admittance method. Four different values of the central wavenumber of the Morlet wavelet $|\mathbf{k}_0|$ are considered: **(a)** 2.668, **(b)** 3.081, **(c)** 3.773 and **(d)** 5.336. The white stars show locations, for which the calculation results are demonstrated. Abbreviations as in Figure 4.1.

fit between the observations and predictions. In fact, a good fit of the observed and predicted admittance is obtained for two locations only (TAM-2 and WARS). As pointed out by Forsyth (1985) and Kirby and Swain (2008), the admittance estimates of T_e are highly sensitive to the internal load (unknown crust and mantle density anomalies) compared to the coherence estimations; and the first ones frequently overestimate T_e.

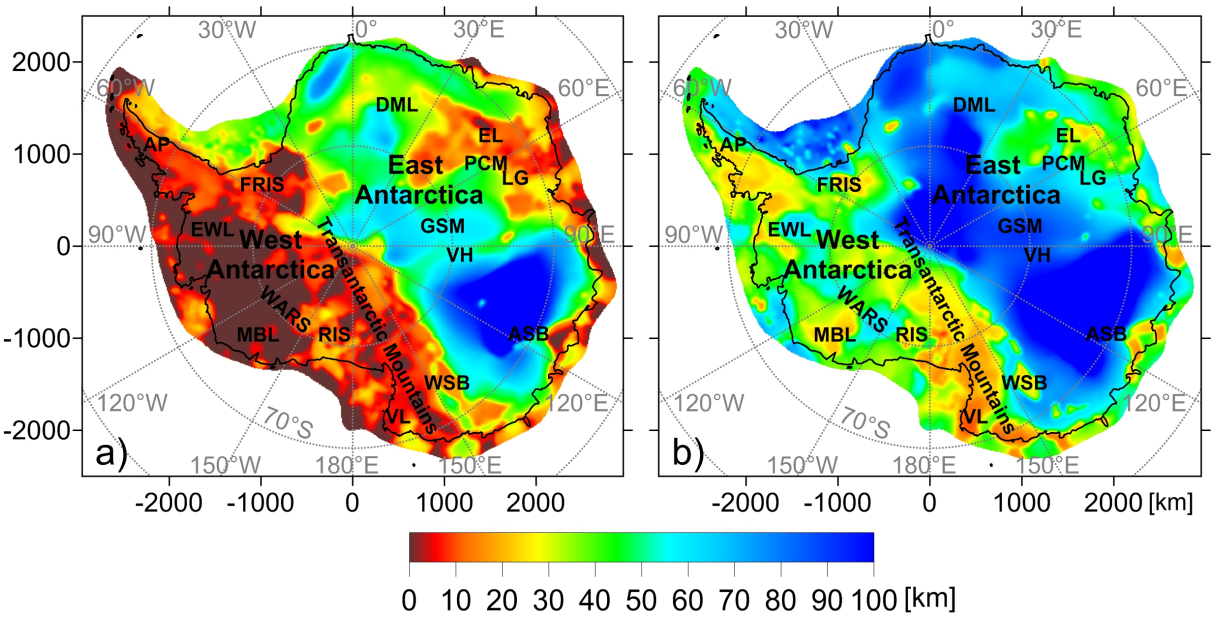

Figure 4.7.: Lower **(a)** and upper **(b)** boundaries of the T_e estimation with the admittance method for $|\mathbf{k}_0| = 3.773$. These values correspond to the misfit $\epsilon = 1.05\epsilon_{\min}$ (Watts et al., 2006). Abbreviations as in Figure 4.1.

However, in most cases the admittance results agree with the T_e estimations obtained with the coherence method. Both ASB and DML regions are characterized by very high T_e evidencing for a very strong lithosphere. In contrast, T_e values for WARS are generally very low. For the TAM we obtain different values for two locations (23 km and 10 km). However, in both cases, the misfit between the observed and predicted values has no clear minimum. Therefore, any value within the interval from 0 km to 35 km would almost equally fit the observations. The high T_e for GSM is based on the very long wavelengths (> 1000 km) and doesn't fit the observed values at the mid and short wavelengths. The long wavelength signal in this area is likely biased by extraneous factors, which is visible in the normalized squared imaginary part (NSIP) of the free air coherency (Fig. 4.5). For LG, the obtained value ($T_e = 40$ km) is relatively high. However, the misfit curve is nearly flat from 0 km to approximately 60 km implying that T_e may be equal to any value within this interval.

4.6. Discussion

In the discussion we chiefly refer to the results obtained with the coherence method since they better fit to the observed values and are less uncertain.
Analysis of the variations of the effective elastic thickness within the Antarctic continent

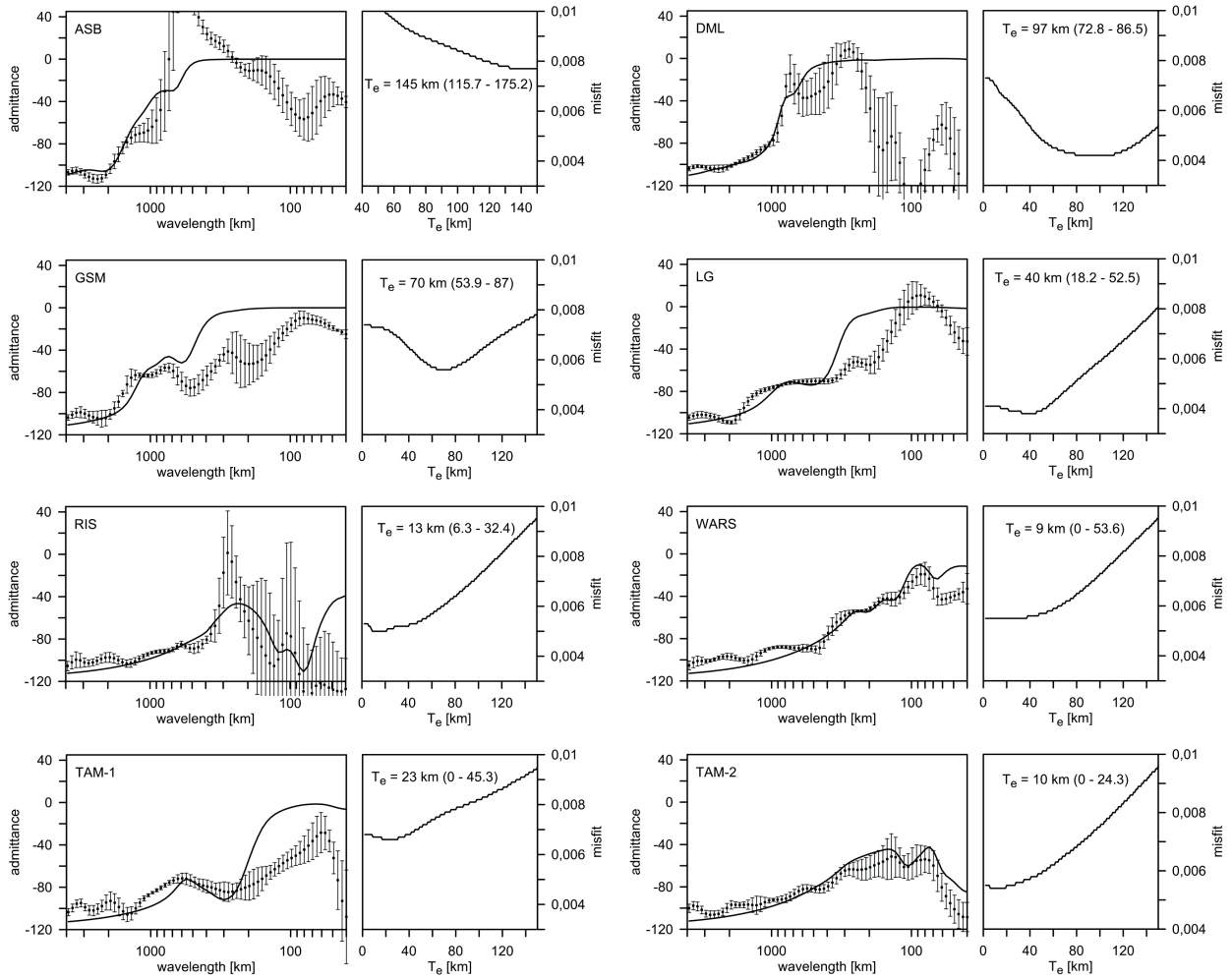

Figure 4.8.: Admittance and misfit for eight locations in Antarctica (Fig. 4.6c) for $|\mathbf{k}_0| = 3.773$. Left graphs show admittance depending on the wavelength. Points with uncertainties represent observations, solid line – predicted (model) values. Right graphs show misfit depending on T_e. The lower and upper boundaries corresponding to the misfit $\epsilon = 1.05\epsilon_{\min}$ are shown in parentheses. Abbreviations as in Figure 4.1.

reveals a clear distinction between strong lithosphere in the east and weak lithosphere in the west, correlating well with the position of the East Antarctic Craton and the thinner, hotter West Antarctic terrains. Major geological features of East Antarctica formed in the Precambrian with a tectonic reactivation during the Paleozoic and early Mesozoic (Boger, 2011). Consequently, it is chiefly characterized by thick cold lithosphere with relatively high values of T_e and presumably low heat flow values (e.g. Shapiro and Ritzwoller, 2004). In

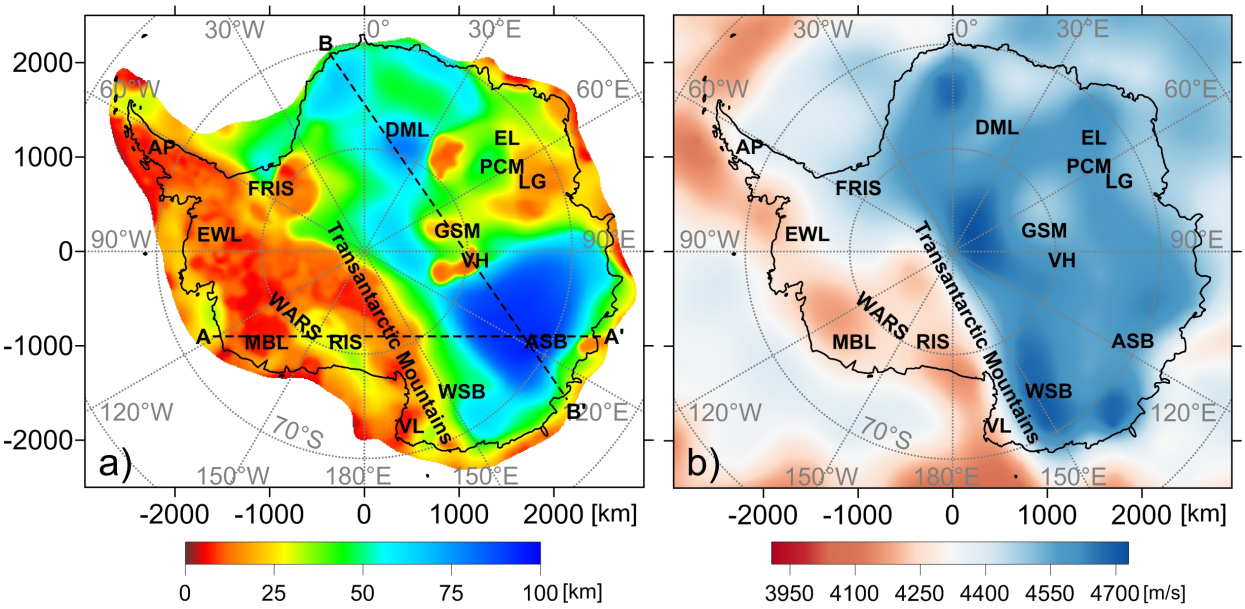

Figure 4.9.: **(a)** Variations of T_e obtained by the coherence method for a central wavenumber of the Morlet wavelet $|\mathbf{k}_0| = 3.773$. Dashed lines represent the locations of the profiles shown in Fig. 4.10. **(b)** Tomography model SL2013-2.1 (Schaeffer and Lebedev, 2013) of S-velocities at a depth of 100 km. Abbreviations as in Figure 4.1.

contrast, West Antarctica is dominated by relatively young terrains formed and developed in the Mesozoic and Early-Mid Cenozoic. The large scale features in our T_e map generally correlate well with seismic tomography studies, which imaged low S-velocities in WANT and high velocities in EANT at a depth of 100 km according to the model SL2013-2.1 (Schaeffer and Lebedev, 2013) (Fig. 4.9b). Apart from the general distinction, the SL2013-2.1 model only shows little structure and we should take care not to over interpret these small scale features. A study of McKenzie et al. (2015) examining average T_e for EANT and WANT using admittance calculations also gives a clear distinction between these provinces. Yet their values (21 km and 5 km respectively) are substantially lower than our findings. There might be several reasons for these discrepancies. First, we use the gravity model, which includes high resolution terrestrial observations. Second, in our method, the load ratio is wavenumber-dependent, which is determined by the load deconvolution process (Lowry and Smith, 1994) from the observed gravity and topography data. In contrast, McKenzie et al. (2015) used an analytical formula for the model admittance with a uniform load ratio to fit the observed admittance. Third, the misfit curve for EANT calculated by McKenzie et al. (2015) has no clear minimum and any value of T_e exceeding $\sim$17 km would provide an al-

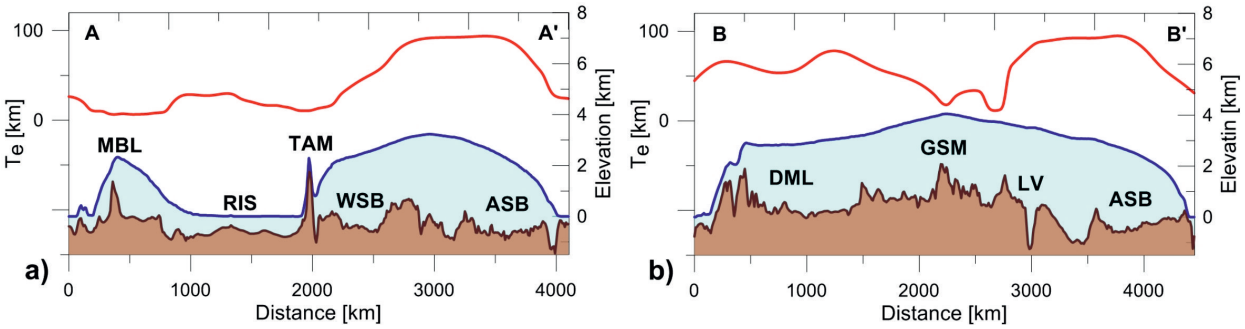

Figure 4.10.: Profiles across Antarctica showing the Effective Elastic Thickness T_e determined by the coherence analysis (red), surface elevation (blue) and bedrock elevation (brown). Locations are shown in Fig. 4.9. Abbreviations as in Figure 4.1.

most equal fit to the observed admittance. Therefore, the observed value of 21 km does not represent an exact estimate, but a lower bound for T_e. On the other hand, our results based on the coherence analysis well correspond globally to the T_e estimates for similar tectonic provinces (e.g. Audet and Bürgmann, 2011; Tesauro et al., 2012).

As previously mentioned, EANT and WANT are separated by the Transantarctic Mountains. In a previous study, ten Brink et al. (1997) derived an effective elastic thickness of 70 km for the TAM based on the analysis of a very limited area, thus attributing the mountain side to Eastern Antarctica with its thick and strong lithosphere. Our results reveal a very weak lithosphere with T_e about 10 km, which characterizes the whole mountain chain. This suggests that the TAM are located on the western side of the margin between EANT and WANT, supporting the theory of van Wijk et al. (2008) that formation and further uplift of the TAM is connected to the tectonic history of the West Antarctic rift system (WARS) starting at the Late Cretaceous with an active uplift phase at the Mid-Late Cenozoic. At the first stage (about 100 Ma) the entire area of the WARS was subjected to uniform extension. During the second stage in the Late Paleogene, the distributed extension has localized within a narrow zone close to the TAM (Huerta and Harry, 2007) that was accompanied by volcanic activity and initiation of the main stage of the TAM uplift. Our results support this scenario in general (Figs. 4.9 and 4.10), however one should note, that the T_e map reflects only present-day thermo-mechanical state of the lithosphere and can provide an additional knowledge on tectonic history only indirectly. The Wilkes Subglacial Basin (WSB) in the hinterland of the TAM exhibits a transition between WANT and EANT with a gradual increase of T_e (Fig. 4.10a).

According to our results, East Antarctica (EANT) doesn't represent a homogeneous litho-

spheric block, but is clearly divided into several parts (Fig. 4.9a) and thus offers insight into the lithospheric structure of EANT that has not been imaged in the past, e.g. by seismic tomography (compare Fig. 4.9). The strongest lithosphere with T_e up to 90 km is found between 90°E and 130°E around the Aurora subglacial basin (ASB) (Fig. 4.9). Tectonic and geological reconstructions suggest that the ASB basement consists of Mesoproterozoic to Archean rocks of the Mawson and Crohn Craton that sutured in the late Mesoproterozoic and remained comparably unaffected by tectonic processes since then (Boger, 2011). Several studies identified Terre Adélie Land just east of the ASB as the nucleus of Antarctica (e.g. Fanning et al., 1988; Flöttmann and Oliver, 1994). Hence, the ASB and surrounding are formed of very old, cold and dense lithosphere explaining the sub-sea-level topography, fast seismic velocities and high lithospheric strength (Fig. 4.9). Another block characterized by high T_e, which is only slightly lower than in the ASB, is represented by the Central Dronning Maud Land (DML) (Figs. 4.9-4.10). According to Boger (2011), this is also an Archean fragment of the Kaapvaal Craton of southern Africa that collided with central Antarctica in the Cambrian.

The strong nuclei associated with the DML and ASB are divided by a zone of relatively low T_e as demonstrated by the results based on the coherence analysis (Figs. 4.3, 4.9 and 4.10). The minimum T_e within EANT (~ 15 km) is found in the area of the Lambert Graben (LG). LG is described as a failed rift system that formed during the Carboniferous to Cretaceous (Harrowfield et al., 2005; Lisker et al., 2003; Powell et al., 1988) that holds the Lambert Glacier (Reading, 2006). The presence of the glacier also caused strong localized erosion (≥ 2 km) since the Oligocene (Thomson et al., 2013). The low values of T_e might be also explained by possible passing of a Cenozoic mantle plume below the LG and GSM (Sleep, 2006) causing the LG valley incision. Both explanations would be consistent with our observations, yet a distinction between them cannot be given by our results at this time, but would require further study. The anomalously low values of T_e in the LG correlate well with high ice velocities within the area (Rignot et al., 2011) that might assume interconnection between the T_e, heat flow, and ice dynamics. The results obtained for the Gamburtsev Subglacial Mountains (GSM) are controversial. According to the coherence analysis, T_e is reduced to 25-30 km compared to the DML and ASB (Fig. 4.9). As already mentioned, this result seems to be reliable because the normalized squared imaginary part (NSIP) of the free air coherency is close to zero in the whole wavelength interval used for determination of T_e for GSM with the coherence method ($\lambda < 1500$ km, Fig. 4.5). Consequently, the Free-air coherence in the GSM is among the highest observed in the continent because the ice shield prevented significant erosion during the last 30 Ma, as already reported by Paxman

et al. (2016). Furthermore, the decrease in coherence fitted for $T_e = 26\,km$ (Fig. 4.5) is the drop with the maximum wavelength, therefore, this is the highest possible value of T_e. This result is close to the result of Paxman et al. (2016), who calculated free air admittance and Bouguer coherence suggesting very low T_e of 0-1 km and 5-14 km, respectively. We also observe a relative minimum of v_s in this area at a depth of 100 km as demonstrated by the model of Schaeffer and Lebedev (2013) (Fig. 4.9b), hinting at possibly anomalous lithosphere in the larger GSM area. Sleep (2006) suggested a presence of a plume head beneath the GSM and Vostok highlands, which reheated and weakened the lithosphere in this region and caused an uplift of the GSM explaining our observations of reduced T_e. Recently, a bifurcation of the rift bounding the GSM that would weaken the lithosphere and thus lower T_e, was also suggested by Phillips and Läufer (2009).
On the other hand, the admittance analysis gives relatively high values of T_e ($\sim 70\,km$) for the GSM, although the model admittance fits the observations at the long wavelengths only ($\lambda > 700\,km$, Fig. 4.8). This agrees with the result of Ferraccioli et al. (2011), who obtained approximately the same value based on the shape of the Moho, which is determined from the gravity data. It should be noted that this result, as well as our admittance analysis, could be seriously biased by the density heterogeneity of the crust and upper mantle, which is not taken into account in both studies. Actually, for measuring of elastic deformations one should determine horizontal gradients of the Moho, which are not well-constrained, even by seismic studies. Yet, we cannot completely reject the admittance model, although we give some preference to the result based on the coherence analysis determining reduced T_e for the GSM. To further clarify the thermo-mechanical state of the GSM lithosphere, a closer study of the region possibly with other, independent methods is necessary.

4.7. Conclusions

We used bedrock topography, ice thickness and a combination of new satellite and high resolution terrestrial gravity data to determine variations of the effective elastic thickness over the Antarctic continent. Both admittance and coherence were derived using modern cross-spectral analysis methods based on the fan wavelet technique. Analysis of the wavelength-dependent admittance and coherence results and other parameters for several principal locations has shown that the coherence based values are more reliable for the problem at hand and thus form the basis for interpretations in this study.
Generally, Antarctica's division into two distinct tectonic provinces is also seen in the lithospheric rigidity. While T_e is mostly high in the cratonic area of East Antarctica, West

Antarctica is characterized by much lower values. The Transantarctic Mountains separate these domains, but if they form part of EANT or WANT remains somewhat enigmatic. We determined low T_e with values around 10 km for the entire mountain chain similar to what can be found in the entire western Antarctic domain. We thus suggest that the TAM are part of WANT.

Apart from the general distinction between EANT and WANT, we were also able to resolve smaller scale fragmentation within these blocks. Especially East Antarctica is not homogeneous in lithospheric strength as previously thought, but shows strong variations of T_e for different provinces. The highest effective elastic thickness can be found in the Aurora Subglacial Basin with surroundings ($T_e \sim 90$ km). Slightly lower values of $T_e \sim 70 - 80$ km can be found in Dronning Maud Land. We interpreted this as a sign for very old, cold and strong lithosphere, which is also supported by tectonic and geological reconstructions (Boger, 2011). The weakest lithosphere ($T_e \sim 15$ km) within EANT appears in the Lambert Graben (LG). Such an anomalously low value, compared to the mean for EANT, might be explained by a combination of several factors such as primary tectonic weakness inherited from the Permian-Triassic active rifting phase of the LG (Harrowfield et al., 2005), strong localized erosion (≥ 2 km) along the LG since the Oligocene (Thomson et al., 2013), and possible influence of a Cenozoic mantle plume (Sleep, 2006).

According to the coherence based results, the weak zone extends from the LG towards the Gamburtsev Subglacial Mountains. The effective elastic thickness of the GSM has been the subject of discussion (e.g. Ferraccioli et al., 2011; Paxman et al., 2016). The results based on the coherence analysis indicate that the effective elastic thickness is reduced to $T_e \sim 26$ km and support the assumption of low lithospheric strength within the GSM area. Anticipated heating by a mantle plume might be the cause of the lithospheric weakening (Sleep, 2006). On the other hand, the admittance results for the GSM give $T_e \sim 70$ km, which is not remarkably different from the ASB and DML. We suppose that the admittance results might be substantially biased by density variations within the lithosphere and therefore give some preference to the coherence analysis, which evidences for the reduced effective elastic thickness of the lithosphere.

The West Antarctic lithosphere is characterized generally by very low values of T_e (5-20 km), which agrees with the tectonic history of WANT. Since the Late Cretaceous the entire area of WANT has been affected by complex tectonic processes associated with late fragmentation of Gondwana, the WARS formation and accompanying magmatism. Local variations of T_e (e.g. such as a relative maximum in the Ross Ice Shelf) likely correspond to ancient and more strong terrains initially forming WANT (e.g. Mukasa and Dalziel, 2000).

Therefore, our T_e models present new insight into the lithospheric structure of Antarctica, because it shows lateral heterogeneity of the lithosphere that has not been provided previously by other (chiefly seismic tomography) methods. Instead of a comparably uniform strong cratonic lithosphere in EANT, our study reveals lithospheric fragmentation with both methods employed here. However, the exact extend and origin of this low T_e region within EANT remains somewhat unclear and would require further studying based on independent geophysical methods like for example thermo-mechanical modeling of the lithosphere.

Context

In order to comprehend the link between lithosphere and near-surface dynamics, a thorough understanding of the solid Earth is vital. The variation of the effective elastic thickness that was estimated in the previous chapter (chapter 4) allows to infer information on the thermo-mechanical state of the lithosphere. For Greenland, Petrunin et al. (2013b) have shown that the lithospheric heat flow is a crucial factor for dynamical ice shield modeling. Yet, quantification of temperatures and distinction from other factors influencing the effective elastic thickness is necessary to estimate the sub-glacial surface heat flux. A better image of the thermal state of the lithosphere can be obtained by employing seismic tomography (chapter 5). Seismic velocities depend to a large extent on temperature, therefore they can be used to estimate temperature variations (Tesauro et al., 2014) and thermal density variation through mineral physics equations (Stixrude and Lithgow-Bertelloni, 2005). Through the iterative combination of the temperature modeling with a joint inversion of gravity and residual topography, it is possible to determine the density distributions within the lithosphere. Additionally, this approach allows to determine whether density variations originate from either thermal or compositional changes. A composition model in terms of the magnesium number Mg # is also provided from the iterative scheme and used for temperature estimate corrections.

In the first study (chapter 4), both coherence and admittance of the gravity field and the residual topography were used to estimate T_e variations over Antarctica. This approach yielded comparable results for large scale structures. On smaller scales however, differences become visible. Both models predict lithospheric fragmentation through weakening within EANT. The position, however, is shifted between the two models. Depletion in heavy elements such as iron is an indication for aged lithosphere, while lower Mg # can signal rejuvenation of the crust and lithosphere. The latter can be accompanied by structural weakening, creating a potential link between depletion and strength analysis. Hence, the composition model as well as the temperature model obtained in the second study (chapter 5) will help to ascertain the validity of both T_e models. With the same input gravity field, chapters 4 and 5 share a common data source, but analyze it in distinctly different ways.

Consequently, they represent two independent studies that complement and cross-validate each other in better characterizing the Antarctic lithosphere in terms of flexural rigidity, temperature, density and composition.

5 | 3D density, thermal and compositional model of the Antarctic lithosphere and implications for its evolution

Chapter abstract

We create a 3D density, temperature and composition model of the Antarctic lithosphere using an integrative approach combining gravity, topography, tomography data with mineral physics constraints and seismic data on crustal structures. The latter is used to create a new Moho and crustal density model. Temperature and thermal density variations are estimated based on S-wave velocities from two independent tomography models (SL2013sv and AN1-S). Results of the Antarctic continent show the well-known distinction between East and West Antarctica in temperature and density to a depth of about 200 km. Incorporating compositional variations in the temperature calculations increases temperatures in depleted regions by up to 150°C, giving improved insights into thermal structures. The thickness of the lithospheric root also varies strongly between these regions, with values below 100 km in the west and above 200 km in the east. Regions with negative compositional density variations (<-0.040 g/cm^3 at 100 km), high depletion (Mg # >91.5) and low temperatures (<800°C) (central Dronning Maud Land, along the east flank of the Transantarctic Mountains) are interpreted as Precambrian cratonic fragments. Nearly undepleted lithosphere is found in the Lambert Graben and the Aurora Subglacial Basin and is attributed to Mesozoic rifting activity that has caused lithospheric rejuvenation.

Published manuscript:

Haeger, C., Kaban, M. K., Tesauro, M., Petrunin, A. G., Mooney, W. D. (2019). 3D density, thermal and compositional model of the Antarctic lithosphere and implications for its evolution. *Geochemistry, Geophysics, Geosystems*, 2005, 1–20.
http://dx.doi.org/10.1029/2018GC008033

Geochemistry, Geophysics, Geosystems

RESEARCH ARTICLE
10.1029/2018GC008033

Special Section:
Polar region geosystems

3-D Density, Thermal, and Compositional Model of the Antarctic Lithosphere and Implications for Its Evolution

C. Haeger[1,2], M. K. Kaban[1,3], M. Tesauro[4], A. G. Petrunin[1,3], and W. D. Mooney[5]

[1]GFZ German Research Centre for Geosciences, Potsdam, Germany, [2]Free University of Berlin, Berlin, Germany, [3]Schmidt Institute of Physics of the Earth, Moscow, Russia, [4]Dipartimento di Matematica e Geoscienze, Universita degli studi di Trieste, Trieste, Italy, [5]United States Geological Survey, Earthquake Science Center, Menlo Park, CA, USA

Key Points:
- Inversion of gravity, topography and seismic tomography data yields improved thermal, density and compositional models of the upper mantle
- Precambrian cratonic fragments were identified in Eastern Antarctica
- Almost undepleted lithosphere is found in the Lambert Graben and the Aurora Subglacial Basin

Supporting Information:
- Supporting Information S1
- Data Set S1

Correspondence to:
C. Haeger,
carina.haeger@gfz-potsdam.de

Citation:
Haeger, C., Kaban, M. K., Tesauro, M., Petrunin, A. G., & Mooney, W. D. (2019). 3-D density, thermal, and compositional model of the Antarctic lithosphere and implications for its evolution. *Geochemistry, Geophysics, Geosystems*, *20*. https://doi.org/10.1029/2018GC008033

Received 30 OCT 2018
Accepted 9 JAN 2019
Accepted article online 13 JAN 2019

Abstract We create a 3-D density, temperature, and composition model of the Antarctic lithosphere using an integrative approach combining gravity, topography, and tomography data with mineral physics constraints and seismic data on crustal structures. The latter is used to create a new Moho and crustal density model. Temperature and thermal density variations are estimated based on *S* wave velocities from two independent tomography models (SL2013sv and AN1-S). Results of the Antarctic continent show the well-known distinction between East and West Antarctica in temperature and density to a depth of about 200 km. Incorporating compositional variations in the temperature calculations increases temperatures in depleted regions by up to 150 °C, giving improved insights into thermal structures. The thickness of the lithospheric root also varies strongly between these regions, with values below 100 km in the west and above 200 km in the east. Regions with negative compositional density variations (<-0.040 g/cm^3 at 100 km), high depletion (Mg # > 91.5), and low temperatures (<800 °C; central Dronning Maud Land, along the east flank of the Transantarctic Mountains) are interpreted as Precambrian cratonic fragments. Nearly undepleted lithosphere is found in the Lambert Graben and the Aurora Subglacial Basin and is attributed to Mesozoic rifting activity that has caused lithospheric rejuvenation.

Plain Language Summary Antarctica remains one of the least studied areas on Earth, because large ice masses and climate conditions strongly hinder measurements. It plays an important role in global phenomena such as sea level change. In order to understand and predict these processes, we need knowledge about the heat coming from the Earth's interior. It has been recently recognized that the thermal state of the lithosphere, the rigid outer shell of the Earth, plays an important role in controlling dynamics of the ice shield and, thus, global sea level changes. Therefore, we create a model of the lithosphere describing the variation in temperature, density, and composition. Before, such models were created by using some single data set (usually seismic tomography). We employ a new integrative approach, combining several data sets to create a comprehensive 3-D model of the Antarctic lithosphere. Combination of various data sets gives more robust models than when using a single approach. Our results of the Antarctic continent show strong differences between East and West Antarctica in temperature and density to a depth of about 200 km. Regions with negative compositional density variations and low temperatures are identified within East Antarctica and are interpreted as being substantially older than the surrounding continent.

1. Introduction

Density, temperature, and compositional variations in the uppermost mantle are important factors in determining the dynamics of the lithosphere. Therefore, in order to fully understand these dynamic processes, it is crucial to determine the location, magnitude, and origin of their heterogeneities. Also, as recently shown for Greenland, the heat flux from the lithosphere strongly affects ice dynamics (Petrunin, Rogozhina, et al., 2013). Hence, lithospheric temperature and heat flux estimates are important when modeling changes in the ice mass balance, glacial isostatic adjustment, and sea level changes caused by these processes. For Antarctica, our region of interest, information about the composition and temperature fields of the upper mantle is sparse. Geophysical in situ measurements are hindered by the logistical challenges presented by the thick ice sheet. Several studies estimate surface heat flux of Antarctica, including Maule et al. (2005) and Shapiro and Ritzwoller (2004) who used calculations of the thickness of the magnetic crust (Curie depth) and global surface wave tomography data, respectively. Later, An et al. (2015a) used their

Geochemistry, Geophysics, Geosystems 10.1029/2018GC008033

tomography model and a similar mineral physics approach to estimate temperatures in the upper mantle, as well as surface heat flux, but without considering compositional variations. The results of these studies are very controversial. While Maule et al. (2005) predict comparably uniform heat flux throughout Antarctica with local maxima along the shoulder of the West Antarctic Rift System, and in Victoria Land, An et al. (2015a) and Shapiro and Ritzwoller (2004) find a clear distinction between East Antarctica (EANT) and West Antarctica (WANT) and attribute low heat flux to the shoulder of the West Antarctic Rift System. These studies differ strongly in the distribution of local variations and in amplitude, though, with Shapiro and Ritzwoller (2004) predicting much lower values and homogeneous variations in EANT. Radiogenic heat production is another important aspect to consider, when predicting heat flow. Yet high uncertainties are still linked to the distribution of radiogenic elements in the Antarctic crust (e.g., Burton-Johnson et al., 2017).

Even less is known about the compositional variations in the Antarctic upper mantle. Kuge and Fukao (2005) examined *S* and *P* velocity variations using broadband seismograms recorded at several stations within EANT and explained these with the presence of depleted continental lithosphere meaning high concentrations of olivine and a high magnesium number (Mg # = 100 Mg/(Mg + Fe)). On small scales, composition analysis has been conducted using xenolith data from rock exposure and glacier outlets (e.g., Goodge, 2018; Jacobs et al., 2015; Owada et al., 2013). Yet no continent-wide model of compositional variations exists to date for Antarctica.

Whereas existing thermal models of the Antarctic lithosphere have been calculated from a single type of data, such as satellite magnetics (Maule et al., 2005) or seismic tomography (An et al., 2015b; Shapiro & Ritzwoller, 2004), the joint analysis of several data sets can provide a more reliable model of temperature and compositional variations in the lithosphere (e.g., Ebbing et al., 2016; Kaban et al., 2015; Mooney & Kaban, 2010; Pappa et al., 2018). One effective method of analysis is the joint interpretation of seismic, gravity, and topographic data. Seismic velocity and density depend on temperature variations and composition of the upper mantle material but in fundamentally different ways (e.g., Cammarano et al., 2003; Stixrude & Lithgow-Bertelloni, 2005; Tesauro et al., 2014). This makes it possible to constrain both compositional and temperature variations within the lithosphere. Here we apply an integrative approach of Kaban et al. (2014) and Tesauro et al. (2014) to jointly analyze seismic tomography and gravity data to obtain a 3-D compositional, density, and temperature model of the Antarctic upper mantle. Since the choice of the tomography model may affect the calculated temperatures (e.g., Tesauro et al., 2014), we employ two independent tomography models (An et al., 2015b; Schaeffer & Lebedev, 2013) and compare the results obtained.

2. Tectonic Setting of Antarctica

About 99% of Antarctica is covered by an ice sheet that reaches a thickness maximum of 4,500 m (Figure 1b). Beneath the ice, the continent can be divided into EANT and WANT, two regions characterized by very different tectonics. While EANT is a stable Precambrian craton with a thick and relatively cold lithosphere, the lithosphere in WANT is thinner and hotter (Danesi & Morelli, 2001). WANT consists of several crustal microblocks that amalgamated in the Cenozoic and have undergone late-Cenozoic crustal extension (Dalziel & Elliot, 1982).

On smaller scales, both regions can be divided into subglacial orogens, basins, and rifts with the exact structure being under constant study (e.g., Ferraccioli et al., 2016). Figure 1a shows the bedrock topography with the names of the most relevant structures. The largest structure in EANT spans 0°–100°E and consists of a subglacial plateau that is interrupted by the Lambert Graben, a Mesozoic failed rift system that holds Antarctica's largest glacier, called Lambert Glacier (Harrowfield et al., 2005; Lisker et al., 2003; Powell et al., 1988). The highest elevations can be found in the Gamburtsev Subglacial Mountains (2,400 m) and Dronning Maud Land (2,500 m). The latter is a key region to understanding the amalgamation of Gondwana, because of its central location in the supercontinent. In the west, the Archean Grunehogna craton is bordered by the Mesoproterozoic Maud Belt. Adjacent to this craton, the Tonian Oceanic Arc Super Terrane represents juvenile Neoproterozoic remnants of the Mozambique Ocean (Jacobs et al., 2015). The southern margins of this region have still an enigmatic origin, but Jacobs et al. (2017) argue that it is bounded by a yet unidentified, possibly cratonic, tectonic feature. The most notable depressions within EANT are the Wilkes and the Aurora Subglacial Basins that lie up to 1 km below sea level. Recently, Chen et al. (2017) have

Geochemistry, Geophysics, Geosystems 10.1029/2018GC008033

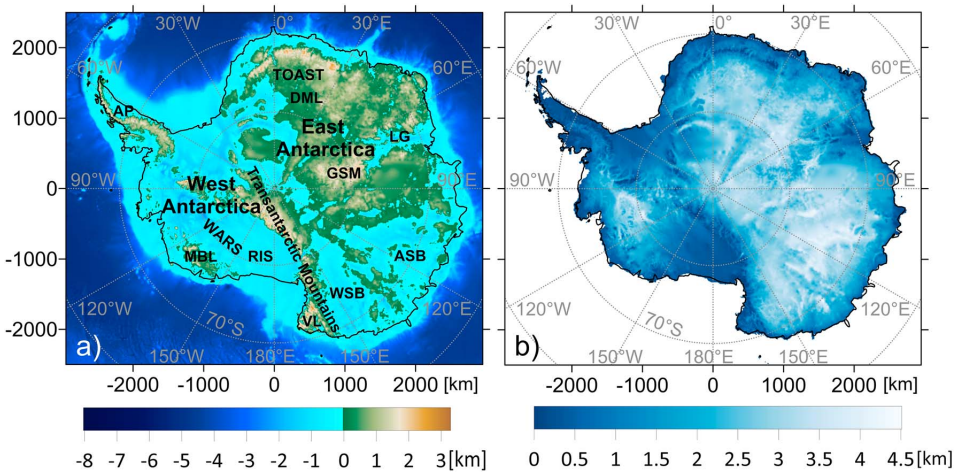

Figure 1. (a) Bedrock topography of Antarctica (Fretwell et al., 2013) and bathymetry of the surrounding ocean (Schaffer et al., 2014). Key tectonic units: AP = Antarctic Peninsula, ASB = Aurora Subglacial Basin, DML = Dronning Maud Land, GSM = Gamburtsev Subglacial Mountains, LG = Lambert Glacier, MBL = Marie Byrd Land, RIS = Ross Ice Shelf, TOAST = Tonian Oceanic Arc Super Terrane, VL = Victoria Land, WARS = West Antarctic Rift System, WSB = Wilkes Subglacial Basin. (b) Ice thickness (Fretwell et al., 2013).

shown that also the lithosphere of the East Antarctic shield is not as uniform as previously thought but is fragmented by the Lambert Graben.

Most of the West Antarctic lithospheric blocks are of Jurassic-Cretaceous age and moved independently prior to their amalgamation with EANT in the Cenozoic (Veevers, 2007). WANT is mostly characterized by sub-sea level bedrock topography with some areas of higher elevations like the Antarctic Peninsula or Marie Byrd Land, a region of intraplate volcanism (Hole & LeMasurier, 1994). Bordering Marie Byrd Land is the West Antarctic Rift System, a 750–1,000-km, largely aseismic rift system (O'Donnell & Nyblade, 2014) that had two distinct phases of extension: a prolonged period of diffuse extension in the Cretaceous and a period of extension focused in the Victoria Land Basin in the Paleogene (Huerta & Harry, 2007).

With a length of 3,500 m, a width of 200 km, and elevations of up to 4,500 m, the Transantarctic Mountains (TAM) are the largest noncontractional mountains in the world, meaning that the uplift was not caused by subduction or contraction (Morelli & Danesi, 2004; ten Brink & Stern, 1992) and mark the border of EANT and WANT. The tectonic process for their formation is debated and several uplift mechanisms have been proposed, including thermal uplift (e.g. Behrendt, 1999), mechanical uplift caused by a broken plate edge (e.g. ten Brink & Stern, 1992), or postrifting uplift (van Wijk et al., 2008).

3. Method

3.1. Modeling Concept

Since both composition and temperature variations can cause density variations, the distinction between these mechanisms has been the subject of multiple studies, both on the global (e.g., Deschamps et al., 2002; Simmons et al., 2009) and continental (e.g., Godey et al., 2004; Khan et al., 2013) scale. Many studies calculate thermal and compositional variations from seismic data alone, making the distinction difficult. To overcome this limitation, we apply a new technique developed by Kaban et al. (2014) that jointly inverts for seismic tomography, residual topography, and gravity data to simultaneously estimate temperature and composition in an iterative approach (Figure 2). We start by correcting the gravity field using available geophysical information, including topography, Moho depth, crustal densities, and deep density variations to obtain the residual mantle gravity field. Further, we correct the topography using the same fields to obtain the residual topography. Both fields are caused by subsurface density anomalies but respond to these

Geochemistry, Geophysics, Geosystems 10.1029/2018GC008033

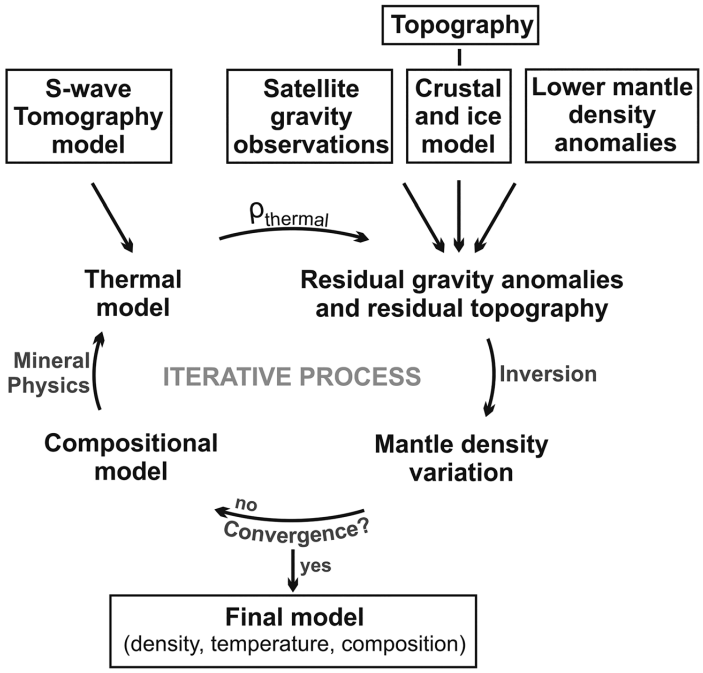

Figure 2. Schematic workflow of the iterative technique applied in this study.

anomalies in a fundamentally different way, thus allowing the inversion for density variations and their depths, more reliably than if only one observation was used. Using these density variations, new compositional models can be calculated. The initial thermal model was calculated using the mineral physics approach presented by Stixrude and Lithgow-Bertelloni (2005) assuming a uniform primitive mantle composition in the first step and then using the newly calculated composition model in the subsequent steps. Density variations related to the temperature variations are calculated and used to correct the density field for the next iteration. This scheme continues until the density changes between iterations are within 1% of the value and convergence is reached.

3.2. Thermal Modeling

To estimate temperature variations within the upper mantle, we calculate synthetic velocities taking into account anharmonic and anelastic properties. We assume a peridotite consisting of four mineral phases with an ideal solid solution of Mg and Fe end-member species with varying percentages: Olivine (Ol) with forsterite and fayalite, orthopyroxene (OPX) with enstatite and ferrosilite, clinopyroxene (CPX) with diopside and hedenbergite, and garnet (Gt) with pyrope and almandine. For Gt, a third Ca species (grossular) is considered to comprise a constant proportion of 20%. The mantle composition is varied between two end-members following Tesauro et al. (2014): A primitive mantle with Ol 58.5%, OPX 15%, CPX 11.5%, Gt 15%, and a magnesium number Mg # ($100 \times Mg/(Mg + Fe)$) of 89 and a depleted mantle with Ol 69.5%, OPX 21%, CPX 4%, Gt 5.5%, and Mg # 94. For the initial thermal model, a uniform primitive mantle composition is assumed.

In order to estimate synthetic shear wave velocities, the shear modulus and density for every mineral phase has to be calculated as a function of temperature and pressure using a mineral physics approach (Stixrude & Lithgow-Bertelloni, 2005). The parameters used for these calculations for each end-member mineral phase are taken from Cammarano et al. (2003) and Stixrude and Lithgow-Bertelloni (2005). For a given mantle composition, the shear modulus and density of the individual phases are averaged, and the anharmonic *S* wave velocity is calculated by

Geochemistry, Geophysics, Geosystems 10.1029/2018GC008033

$$v_{s(\mathrm{anh})} = \sqrt{\frac{\langle \mu \rangle}{\langle \rho \rangle}}. \quad (1)$$

Apart from the anharmonic effects, anelasticity also has to be estimated to determine synthetic velocities for varying temperature and pressure conditions. The synthetic S wave velocity can be described as (Cammarano et al., 2003)

$$v_{\mathrm{syn}} = v_{s(\mathrm{anh})}\left[1 - \frac{Q_s^{-1}}{2\tan\left(\frac{\pi a}{2}\right)}\right], \quad (2)$$

where Q_s is the S wave quality factor and a defines the frequency dependence of the attenuation. These factors describe anelasticity. The values for a as well as those necessary to calculate Q_s are taken from model Q4 from Cammarano et al. (2003). In order to finally estimate temperature variations from the input tomography models, we calculate synthetic velocity for distinct temperatures between 25 and 1,800 °C with a 5 °C spacing and for pressures corresponding to the depths for which the seismic tomography velocities (v_{meas}) have been estimated. Thus, we determine T for which $|v_{\mathrm{syn}}(T) - v_{\mathrm{meas}}|$is minimal in each grid cell.

3.3. Joint Inversion of the Residual Gravity Field and Topography Using an Initial Seismic Tomography Model

The inversion procedure employs minimization of the residual mantle gravity anomalies and residual topography constrained by the initial density model of the upper mantle based on seismic tomography. Both fields are induced by density variations in the mantle, but their amplitudes have distinct dependencies on depth and size of the density anomalies (Kaban et al., 2015). Therefore, inversion of both fields provides a better resolution of the 3-D structure that would not be possible if a single physical parameter (the residual gravity or residual topography) were interpreted. The objective function, which should be minimized, is defined as the following (Kaban et al., 2015):

$$\min\left\{\|A\rho - g_{\mathrm{res}}\|^2 + k\|B\rho - t_{\mathrm{res}}\|^2 + \alpha\|\rho - \rho_{\mathrm{ini}}\|^2\right\}, \quad (3)$$

where A and B are the integral operators converting densities to gravitational and topographic perturbations, respectively, $k = 2\pi G\rho$ is the factor normalizing topography with respect to gravity, and the third term represents a regularization condition, which requires that the final density variations should be close to the initial model or shall be minimized if such a model is not available ($\rho_{\mathrm{ini}} = 0$). This is an Occam-type inversion, and the strength of stabilization of the solution is controlled by the damping factor α.

The inversion is done in the spherical harmonic domain, where it can be made separately for each degree/order set of the coefficients, which significantly reduces computational problems. In this way, it is also possible to take into account dynamic effects in the viscous mantle with the use of a "kernel" technique (e.g., Forte & Peltier, 1991). This approach requires a global distribution of all parameters; therefore, the models of Antarctica have been embedded in the global ones as described below. The impact of mantle density variations is estimated by taking into account dynamic effects, for which purposes we use a predefined radial viscosity distribution, which is based on mineral physics constraints and geodynamic models (Steinberger & Calderwood, 2006). Viscosity variations in the upper mantle can be significant, especially between EANT and WANT. The potential effect of plausible viscosity changes on the inversion results has been tested (e.g., Kaban et al., 2015, supporting information), and it has been demonstrated that it is relatively insignificant since topography kernels for long wavelengths are close to 1 in the uppermost mantle. Additionally, this effect has been evaluated with the code ProSpher (Petrunin, Kaban, et al., 2013), which can cope with high lateral viscosity variations.

Density variations are determined for seven layers starting from the depth of 15 km and down to 300 km (from 50 to 300 km with a step of 50 km). The density best represents the middle point of each layer. The bottom of the model should be below the deepest lithospheric keels (<240 km, e.g., Kuge & Fukao, 2005), which are the main target of the present study. The uppermost layer with the central depth of 15 km is included to account for two possible uncertainties: (1) the crustal density and (2) the Moho depth in WANT and offshore, where it is relatively shallow. As well, we assume that the inverted densities for the

Geochemistry, Geophysics, Geosystems 10.1029/2018GC008033

50-km layer can be partially related to Moho uncertainties in EANT. A joint inversion of the residual topography and gravity provides the ability to locate depth of density anomalies; therefore, starting from the depth of 100 km, the calculated density variations are insignificantly influenced by the crustal uncertainties (Kaban et al., 2015). The relative damping factor α has been chosen based on numerical tests and corresponds to the point in which the calculated density perturbations start to increase rapidly while decreasing α. The results show only a small effect when the damping factor is changed by a factor of 2 in either direction from this point (Kaban et al., 2015).

Numerical tests showed that the method successively reproduces density variations. This method works even when density anomalies are not present in the initial model, as demonstrated by numerical tests (Kaban et al., 2015) and in the study of Asia and Western Pacific for the subduction zone beneath the Ryukyu and Marianna arcs, which is not resolved by the initial tomography model (Kaban et al., 2016b). However, in this case the amplitude of density variations might be reduced by up to 30–40% due to damping. Additional details and numerical tests that prove reliability of the inversion method can be found in Kaban et al. (2015).

3.4. Update of the Compositional Model

In the previous step, the inversion of residual gravity and residual topography yields density variations caused by compositional variations. In cratonic EANT, we assume that these variations are caused by depletion in heavy elements (iron), hence increasing the magnesium number Mg #. For quantification, we follow Tesauro et al., 2014, and calculate the density change that compensates a 0.1 increase in Mg # $\Delta\rho = -0.0016$ g/cm^3. Using this factor, we calculate the new Mg # in every grid point. In order to determine the new mineral fractions, we assume a linear variation between the two end-member compositions defined in section 3.2 in both mineral fractions and magnesium number Mg # of the bulk rock and pick the mineral fractions associated with the new Mg #. The minimal change in depletion is defined as a 0.1 increase in Mg #. Smaller density decreases, or positive values, are not compensated, and thus, the initial primitive composition assumed remains unchanged.

4. Initial Data

4.1. Tomography Models

The seismic velocity structure of Antarctica has been imaged using surface wave tomography at both global (SL2013sv; Schaeffer & Lebedev, 2013) and regional (AN1-S; An et al., 2015b) scales. For the SL2013sv data set, a total of three-fourth million broadband seismograms at a period range of 11–450 s were analyzed to create a global triangular grid with roughly 280-km horizontal spacing for 14 layers of depths between 56 and 720 km. Several resolution tests were conducted, and for Antarctica, columnar perturbations of $\pm$300 m/s with a width of 6.6° were well resolved at 80-km depth. At 260-km depth, these features could still be resolved but showed some smearing. Beneath Antarctica, the model mainly shows the division of the continent into the two regions, EANT and WANT, but also shows some local reduction of *S* wave velocity, such as that observed around the Gamburtsev Subglacial Mountains (Figure 3b), and maximum velocities along the eastern flank of the TAM and in central Dronning Maud Land. The general division is also clearly visible in the AN1-S model (Figure 3a), but small scale variations as well as amplitudes vary notably in comparison. At 100-km depth, amplitudes for the SL2013sv model vary between v_s = 4.73 km/s in EANT and v_s = 4.15 km/s in WANT. While the maximum value in EANT, located at the Lambert Graben, is similar for the AN1-S model (v_s = 4.78 km/s), velocities in WANT are much lower and reach anomalous minimal values of v_s = 3.94 km/s. For this model, which only covers Antarctica, a total of 10,000 Rayleigh wave fundamental-mode dispersion curves registered at 122 broadband seismic stations were used to create a grid with horizontal spacing of 120 km and 51 depth layers. The thickness of these layers varies from 2.5 km down to a depth of 20 km and a thickness of 25 km between 250 km and the maximum depth of 325 km. The horizontal resolution length varies with direction and depth between 150 km in 50-km depth and 500 km in 200-km depth for continental Antarctica. In this study, both tomography models are converted to temperature, allowing a better distinction between valid structures and artifacts caused by the inversion process.

Geochemistry, Geophysics, Geosystems 10.1029/2018GC008033

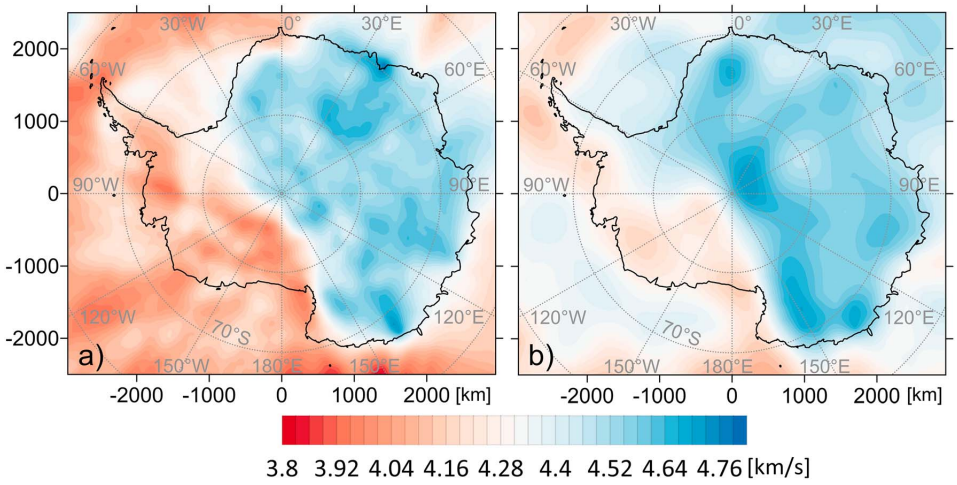

Figure 3. Horizontal cross sections through the seismic velocity models of (a) AN1-S (An et al., 2015b) and (b) SL2013sv (Schaeffer & Lebedev, 2013) at a depth of 100 km.

4.2. Model of the Crust

The lateral density variations in the Earth's crust induce very strong gravity variations that may mask upper mantle effects. Therefore, it is crucial to remove this crustal effect from the observed gravity field. The Moho discontinuity is an interface with one of the strongest density contrast within the lithosphere (Rabbel et al., 2013). Hence, accurate knowledge of the depth of this discontinuity is most important when modeling gravity fields. Existing Moho maps in Antarctica either contain large gaps in coverage (e.g., AN1 Moho; An et al., 2015b; Baranov & Morelli, 2013), are not well constrained seismically, or exhibit nonnegligible deviations from seismic measurements of Moho depths (e.g., AN1 Crust; An et al., 2015b; Laske & Masters, 2013). Therefore, we combine existing models to create a new and improved map of Moho depths for the Antarctic continent.

We built this new map using a compilation of all existing Moho depths from receiver function, reflection, and refraction measurements (AN1 Moho, An et al., 2015b; Janik et al., 2014; Lamarque et al., 2015; circles in Figure 4a). Interpolation is carried out within a 150-km radius around these data points applying a remove-compute-restore technique suggested by Stolk et al. (2013). Large gaps remain especially in EANT in Dronning Maud Land and between 90° and 150°E. These gaps are filled in with the AN1-Crust model from seismic surface wave tomography (An et al., 2015b). The resulting final Moho map (Figure 4a) shows the distinction between EANT and WANT with a minimum in the West Antarctic Rift System, while the Transantarctic Mountains are characterized by shallow to intermediate Moho. The deepest Moho can be found around the Gamburtsev Subglacial Mountains and in northern Dronning Maud Land.

In order to determine the mantle gravity field, the effect of the crust has to be removed from the observed gravity field. To date, no density model of the crystalline crust exists for Antarctica on a continental scale. Therefore, we create a new, first-order model of lateral density variation within the crust. We start by calculating the depth-average crustal S wave velocity using the AN1-S (An et al., 2015b) model from the bedrock topography down to the Moho depth as determined in the previous step. Subsequently, we compile v_p/v_s ratios measured over Antarctica (Bayer et al., 2009; Finotello et al., 2011; Kanao & Shibutani, 2012; Kumar et al., 2014; Miyamachi et al., 2003) and calculate an average value of $\langle v_p/v_s \rangle_{\mathrm{av}} = 1.77$ for the Antarctic continent to convert from average crustal v_s to v_p. In the final step, we employ the nonlinear conversion method by Christensen and Mooney (1995) to obtain crustal density from the lateral P wave velocity variation. Density perturbations were computed relative to a 1-D reference model, which is the same as that employed in previous studies for North America, Eurasia, and Middle East (Kaban et al., 2014, 2016a, 2016b). The results are shown in Figure 4b.

Geochemistry, Geophysics, Geosystems 10.1029/2018GC008033

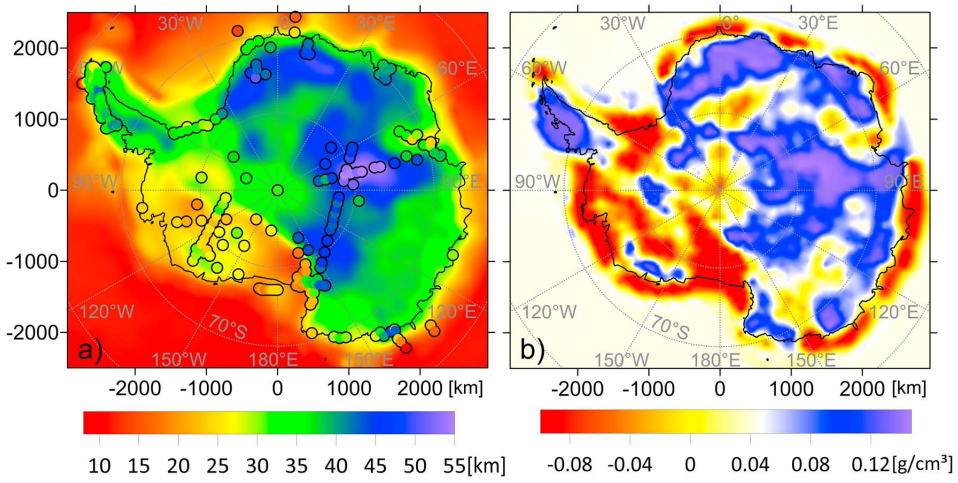

Figure 4. (a) Map of the Moho depth with superimposed determinations from refraction, reflection, and receiver function data (circles) (An et al., 2015b; Janik et al., 2014; Lamarque et al., 2015). (b) Average density perturbations of the crystalline crust.

It should be noted that the constructed crustal model is just a first approximation and is used as a starting point to reduce the ambiguity of the inverse problem. As described above, the inversion scheme includes the option to correct for its uncertainties.

4.3. Gravity Model

The initial gravity data set is a combination of the Eigen-6c4 (Förste et al., 2014) and the AntGG (Scheinert et al., 2016) model (Figure 5a). The former combines terrestrial and satellite data from GRACE, GOCE, and LAGEOS with a maximum resolution of 2,190 spherical harmonics degree and order. The actual resolution varies regionally and depends chiefly on the incorporated terrestrial data, thus limiting it to around 200 km in Antarctica for this model. The latter is a compilation of ground-based, shipborne, and airborne gravity anomaly measurements and includes 13 million data points, covering 73% of the Antarctic continent at 10 km resolution. It adds new and improved short wavelength structures to the Eigen-6c4 data set but is biased on longer wavelengths because of large gaps especially over EANT. Therefore, for our initial free air gravity model, the Eigen-6c4 data are used for wavelengths of $\lambda > 250$ km and the AntGG data for $\lambda < 150$ km with a gradual transition for 150 km $< \lambda <$ 250 km. As it was mentioned above, maximal horizontal resolution of the employed crustal model is about 110–150 km; therefore, the ground observations only marginally improve the satellite based model.

In order to obtain the residual mantle gravity field, we subsequently removed the effects of topography, water and ice columns, density variations in the crust, and Moho variations (Figure 5b). The anomalous effect of these layers was computed relative to the same 1-D reference model as used in section 4.2. This makes it possible to directly compare the results obtained for different continents. The reference model consists of two layers (0–15 km with the density of 2.7 g/cm^3 and 15–40 km of 2.94 g/cm^3), underlain by the upper mantle with the density of 3.35 g/m^3. Although this model is continental, it is isostatically balanced with the normal oceanic lithosphere of 180 Ma age (Kaban & Schwintzer, 2001). Therefore, the total gravity effect of all crustal layers down to the Moho will be the same when employing both reference models (oceanic and continental), as demonstrated by a smooth transition from the continental to the oceanic part (Figure 5b). Basically, plausible changes of the 1-D reference model only lead to a constant shift of the computed residual anomalies (Mooney & Kaban, 2010), which is not considered in this study.

The effect of each layer has been computed using a 3-D scheme on a spherical Earth as a sum of all tesseroids limited by geographical coordinates (in this case 1° × 1°) and upper/lower boundaries of the layer. A detailed description of this technique can be found in Kaban et al. (2016a). It has been demonstrated before (e.g.,

Geochemistry, Geophysics, Geosystems 10.1029/2018GC008033

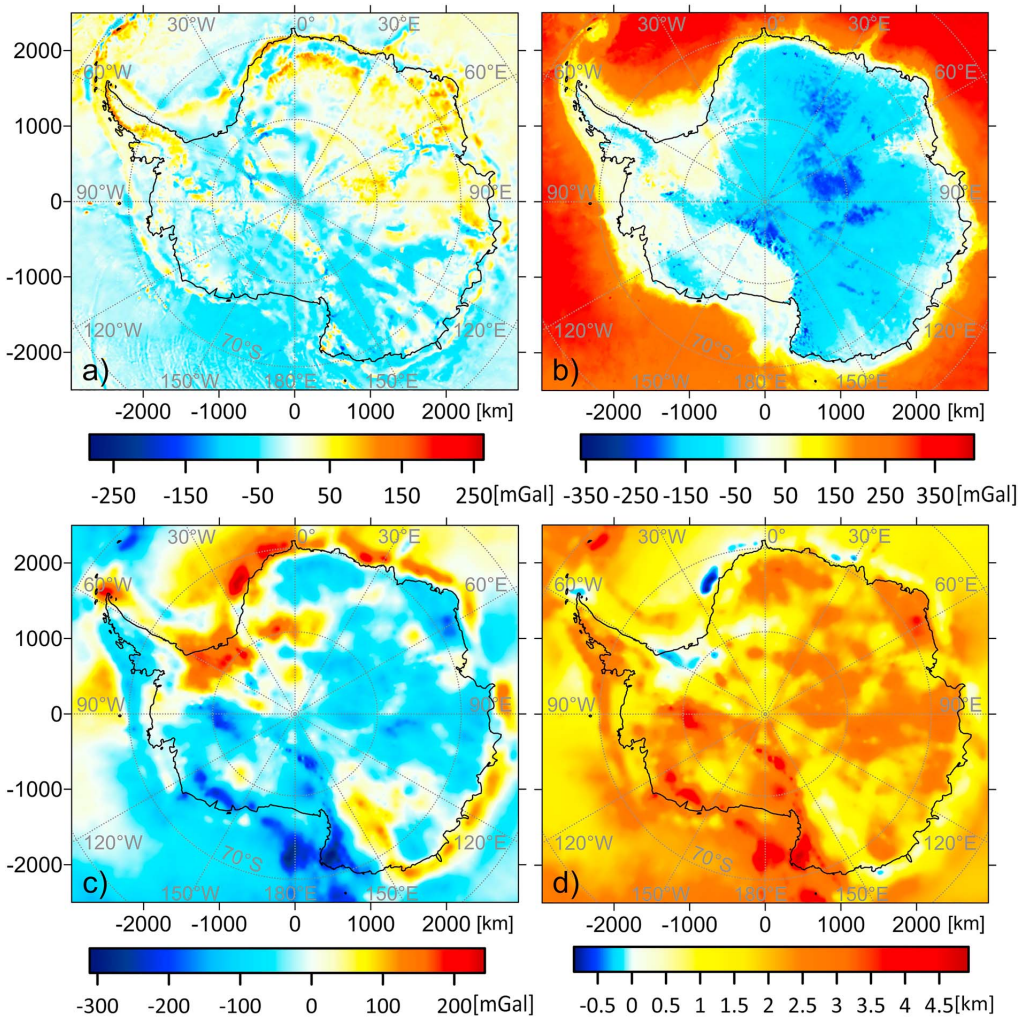

Figure 5. (a) Free air gravity anomalies and (b) Bouguer gravity anomalies. (c) Residual mantle gravity anomalies obtained after removal of the crustal gravity effects and the effect of deep density heterogeneities (below 325 km) from the observed data. (d) Residual topography calculated for a reference density of 2.67 g/cm^3. Zero level corresponds to the reference density model.

Kaban et al., 2004) that the effect of distant zones may produce very significant trends over continental-wide structures. Therefore, when calculating the effects of each crustal layer, we consider its variations for the whole Earth. Also, the inversion scheme based on spherical harmonic decomposition requires global coverage for all parameters. For these purposes, the crustal model of Antarctica has been embedded into a global one in the same way as it was previously done for North America (Kaban et al., 2014) and for Asia (Kaban et al., 2016b). For these purposes, we used the Crust1.0 model (Laske & Masters, 2013), which was improved in several regions (chiefly Eurasia, Australia, and North America) based on recent studies. Although the global model is not well defined in many regions, this is not important for remote areas since they produce only regional trends in limited areas comparable to Antarctica (Kaban et al., 2004).

Information on surface elevation, bedrock topography, and ice thickness are provided by Bedmap2 (Fretwell et al., 2013), bathymetry south of 60°S by RTopo-2 (Schaffer et al., 2014). We calculate the gravity effect of

Geochemistry, Geophysics, Geosystems 10.1029/2018GC008033

each load according to Kaban et al. (2016a). The densities used in these calculations are $\rho_w = 1.03$ g/cm^3 for the water column and $\rho_t = 2.67$ g/cm^3 as the reference density for the upper crust. For the ice column, we chose a constant average density of $\rho_i = 0.92$ g/cm^3 according to Chen et al. (2017). Subsequently, we subtract the gravity effect caused by lateral variations in Moho depth, which causes the most significant changes and the gravity effect caused by the density variations within the crust as observed in our crustal model. The corrections for the residual topography are calculated analogously. In addition, we remove the effect of deep mantle density heterogeneities below 325 km based on global dynamic models (Kaban et al., 2015). The effect of the glacial-isostatic adjustment can also affect the residual gravity anomaly. To remove it, we employed a long-wavelength part of the isostatic anomalies calculated by Kaban et al. (2004). In Antarctica these anomalies clearly show a minimum associated with the noncompensated depression after partial deglaciation. The residual gravity field and residual topography are shown in Figures 5c and 5d. These anomalies are negatively correlated since the original density anomalies oppositely affect the residual gravity and residual topography. For example, any positive density anomaly produces an increase of the gravity field while the effect on the residual topography is negative since it sinks the whole lithospheric column downward.

Mooney and Kaban (2010) discuss in detail the potential errors of the residual mantle gravity anomalies and residual topography. They concluded that in areas well covered by seismic determinations the total uncertainty combining all factors is about 40 mGal for the gravity field and 0.35 km for the residual topography. In areas with poor seismic coverage, these uncertainties increase to about 75 mGal and 0.65 km, correspondingly (Mooney & Kaban, 2010). However, these estimates cannot be directly used for Antarctica. First of all, we do not have a reliable model of the thickness and density of the subglacial sediments, which effect may amount to −100 mGal or even more. Second, uncertainties of the receiver function and tomography results, which are largely used in the crustal model of Antarctica, are not defined and likely exceed the uncertainties of models derived from seismic refraction and reflection profiles, data that form the basis for crustal models in other continents. Therefore, we consider the initial crustal model as an approximation, and this model will be improved in the inversion of the residual fields.

Generally, the amplitudes of the residual mantle gravity anomalies are not significant over Antarctica compared to other continents such as North America (Kaban et al., 2014) and Eurasia (Kaban et al., 2016b) and are dominated by medium to low negative anomalies (−100 to −170 mGal). Only limited areas in WANT show stronger anomalies than in north Victoria Land (<−300mGal). In EANT, negative gravity features have lower amplitudes (up to −170mGal) and are limited to the area between 30°E and 120°E and to northern Dronning Maud Land. This demonstrates that generally composition and temperature induced density variations are well balanced considering their integral effect through the depth. In contrast, southern Dronning Maud Land is characterized by very high gravity variations (up to 190 mGal), as well as the adjacent Filchner-Ronne Ice-shelf (up to 250 mGal). The last region of high gravity variation with values reaching 130 mGal is located in the Wilkes Subglacial Basin. The ring of high gravity values around the shores of EANT is likely related to the transition from continental to oceanic lithosphere. It can also be related to insufficient resolution of the crustal model; in particular, a sharp decrease of the Moho depth and an increase of the crustal density off the border of Antarctica would reduce these positive anomalies.

5. Results

5.1. Temperature

The initial temperature distribution closely reflects the input velocity models. We calculate temperatures for depth slices between 50 and 300 km to obtain two independent thermal models with a spacing of 50 km. Representative depth slices for 100, 150, and 200 km are shown in Figure 6. In the first iteration based on a uniform primitive composition, both the SL2013 (Figures 6a–6c) and the AN1-S (Figures 6g and 6h) models show a clear distinction between EANT and WANT with temperatures generally over 1,100 °C in WANT at a depth of 100 km for SL2013 and over 1200 °C for AN1-S with maximum values of approximately 1,330 and 1,400 °C, respectively. Both models attribute significantly lower temperatures to EANT yet show strong differences in small scale structures and amplitudes. During the iterative process, compositional variations are determined within EANT, and their influence on the temperature model is calculated. Convergence is reached in the third iteration, and the resulting temperature distributions are shown in Figures 6d–6f for

Geochemistry, Geophysics, Geosystems 10.1029/2018GC008033

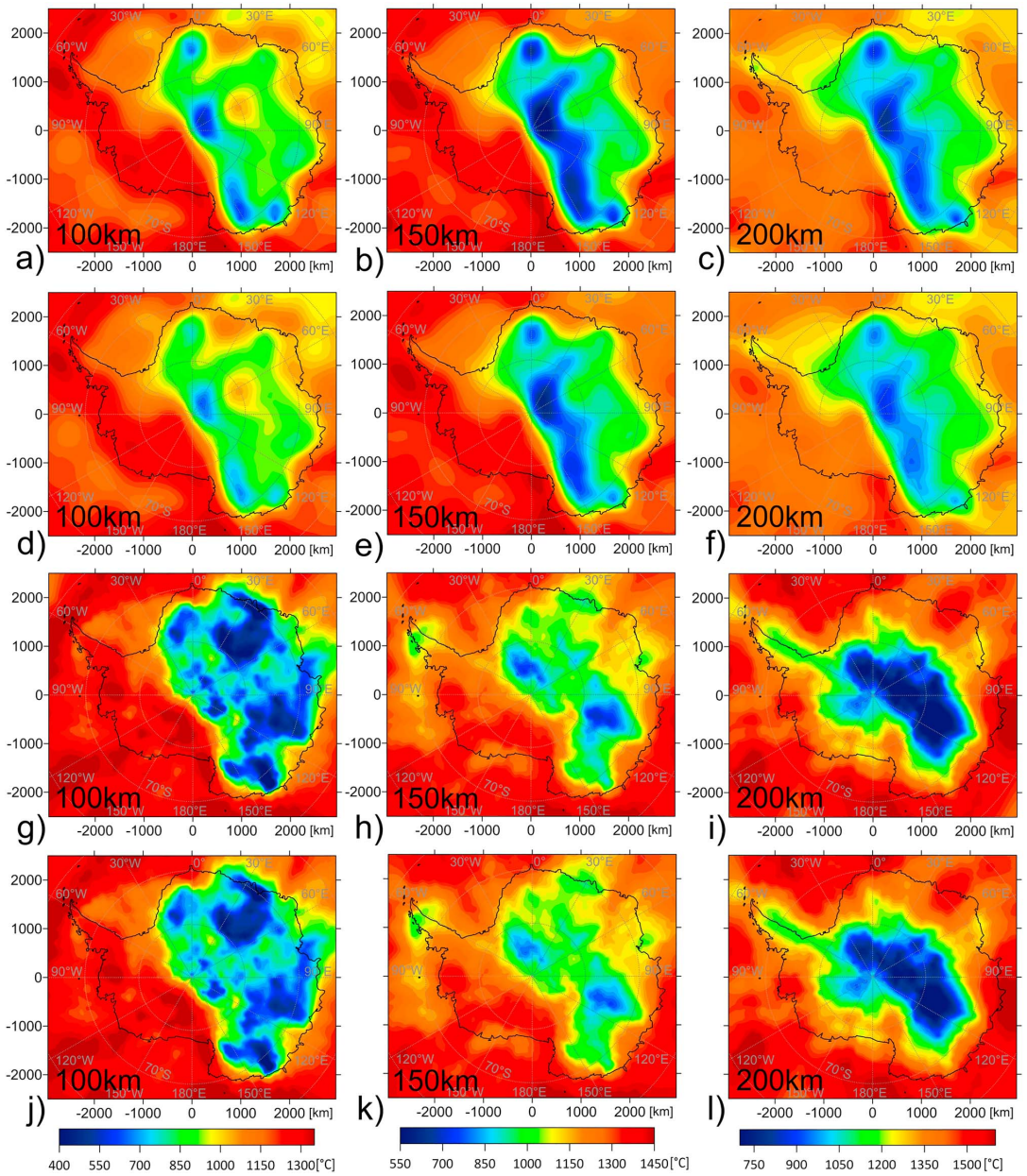

Figure 6. Temperature variations estimated for 100 (first column), 150 (second column), and 200 km (third column). Panels (a)–(f) are estimated on the basis of the SL2013 model, with panels (a)–(c) representing results from the first iteration and (d)–(f) representing the third and final iteration. Panels (g)–(l) are based on the AN1-S model in the first (panels (g)–(i)) and final (panels (j)–(l)) iteration.

Geochemistry, Geophysics, Geosystems 10.1029/2018GC008033

the SL2013 and Figures 6j–6l for the An1-S model. For both models, adding compositional variations does not change the size and distribution of anomalies but elevates temperatures in depleted areas by up to 150 °C. From here on out, we will only examine the models calculated in the final iteration.

In the temperature model derived from SL2013, the majority of EANT is characterized by temperatures below 900 °C for depths of 100 and 150 km. The coldest zones can be found around the South Pole with values below 610 °C, in central Dronning Maud Land (780 °C), and along the eastern flank of the Transantarctic Mountains (690 °C) for the same depths. The TAM themselves are characterized by a transition from very high temperatures (around 1,300 °C at 100 km) in the west to those aforementioned low temperatures in the east in all depth layers under investigation. A local maximum of 1,050 °C is present around the Gamburtsev Subglacial Mountains. At depths of 200 km and below, the temperatures are generally higher and the anomalies smoother, but the general division of the continent is still present and the lithospheric root extends to a depth of roughly 250 km in EANT.

In comparison, the model based on AN1-S is generally characterized by lower temperatures with most of EANT not exceeding 800 °C at 100-km depth. Anomalously low temperatures (<300 °C) are located in the Wilkes Subglacial Basin and inland and offshore Enderby Land. The Aurora Subglacial Basin exhibits temperatures below 500 °C. Like in the SL2013 model, we find local minima just east of the South Pole and in Dronning Maud Land, but those anomalies are shifted in comparison and show more fragmentation. At 150- and 200-km depth, the cold structures are shifted more and more toward central Antarctica with the strongest anomalies in the Aurora Subglacial Basin around the South Pole with anomalous values below 600 °C at 200 km. Additionally, temperatures in the western Transantarctic Mountains even decrease with increasing depth (1,200 °C at 100 km and 940 °C at 200 km), which is probably caused by a strong local increase in velocity in the tomography model that cannot be explained by pressure increase due to depth alone.

When estimating uncertainties in the conversion of seismic velocities to temperatures, several factors have to be taken into account that might vary on a regional scale (Kaban et al., 2014). The choice of the compositional model can cause errors in temperature as high as 200 °C in the presence of high depletion (Lee, 2003). An error in S wave velocity of 0.05 km/s in the input model will cause temperature variations of up to 150 °C in cold cratons (Tesauro et al., 2012). In hot areas, the effect of this uncertainty is diminished, while the effects due to the uncertainties in anelasticity increase. The uncertainties of the elastic parameters are dominated by those of the temperature derivatives, translating into errors in temperature of 70 °C above 300 km (Tesauro et al., 2010). At temperatures over 900 °C, the uncertainty in the attenuation model can also cause errors of about 100 °C in the final model (Jackson et al., 2002). Conversely, our analysis clearly demonstrated that a choice of the tomography model is much more critical for estimation of mantle temperatures than the uncertainty due to the conversion from seismic velocities to temperatures.

5.2. Density

We jointly invert the residual gravity field and the residual topography to obtain the 3-D density distribution of the Antarctic upper mantle. Gravity field variations are more sensitive to changes in composition and depletion while seismic velocities exhibit stronger dependencies to temperature. Iteratively combining these results with the seismic tomography with the gravity based estimates allows to distinguish between temperature-induced versus composition-induced density changes. The abovementioned inversion has been conducted for seven depth layers: in addition to the six depth slices already discussed for temperature variations, the uppermost layer centered at 15 km contains errors within the assumed crustal model. The layer centered at 50 km also includes potential corrections of the initial Moho model. Same as for temperature variations, representative horizontal slices at depths of 100, 150, and 200 km are shown in Figure 7 for the SL2013 model and in Figure 8 for the AN1-S model. For the former, two vertical cross sections are displayed in Figure 9.

Figures 7a–7c and 8a–8c depict the density changes caused by temperature variation for the SL2013 and the AN1-S model, respectively. The thermal density variation resembles closely the temperature variations obtained in the previous step with low temperatures causing high densities and vice versa. For 100 km, the thermal density variation ranges from −0.034 to 0.029 g/cm^3 and from −0.038 to 0.085 g/cm^3 for the SL2013 and AN1-S models, respectively. For the former, the maximum offset of extreme values decreases

Geochemistry, Geophysics, Geosystems 10.1029/2018GC008033

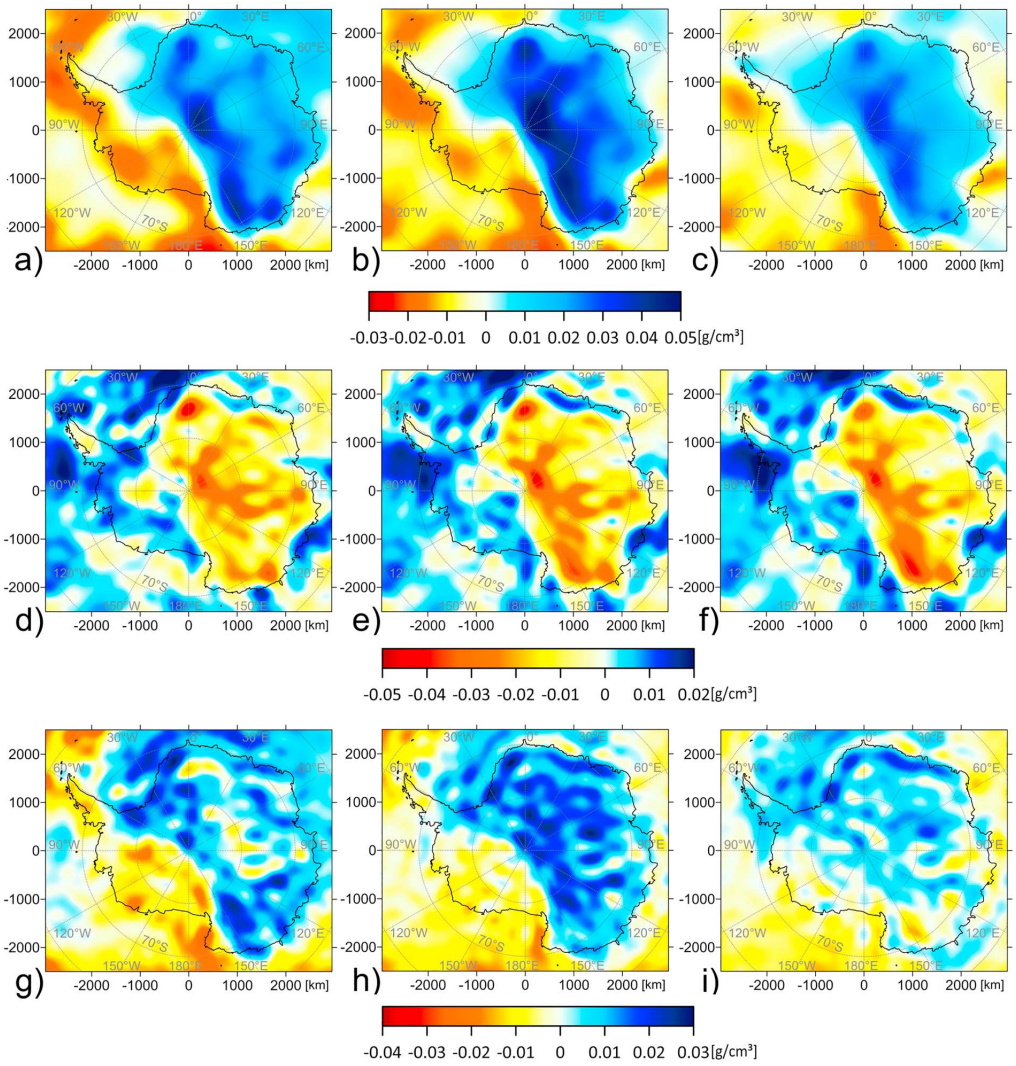

Figure 7. Density variations estimated for 100 (first column), 150 (second column), and 200 km (third column) based on the SL2013 tomography model. Panels (a)–(c) show thermal, (d)–(f) compositional, and (g)–(i) total density variations as obtained in the final iteration.

monotonously with increasing depth to −0.016 to 0.025 g/cm^3 in 200 km, while the latter exhibits minimal values for 150 km (−0.031–0.044 g/cm^3) and a subsequent increase to −0.035 to 0.061 g/cm^3 in 200 km.

Just like the temperature and thermal density variations, composition-induced density variations (Figures 7d–7f and Figures 8d–8f) show a clear division between EANT with lower and WANT with higher densities. The values lie relatively constant for different depths and models between −0.048 ± 0.005 and 0.025 ± 0.002 g/cm^3, but local structures of anomalies differ between the two models. If corrections derived from SL2013 are used in the inversion process, the lowest densities are found in Dronning Maud Land and along the eastern flank of the Transantarctic Mountains. With corrections from AN1-S, the minimum in Dronning Maud Land still exists but is significantly weaker in comparison and further weakens with depth. The minimum along the flanks of the TAM is shifted further toward central EANT with the lowest values in

Geochemistry, Geophysics, Geosystems 10.1029/2018GC008033

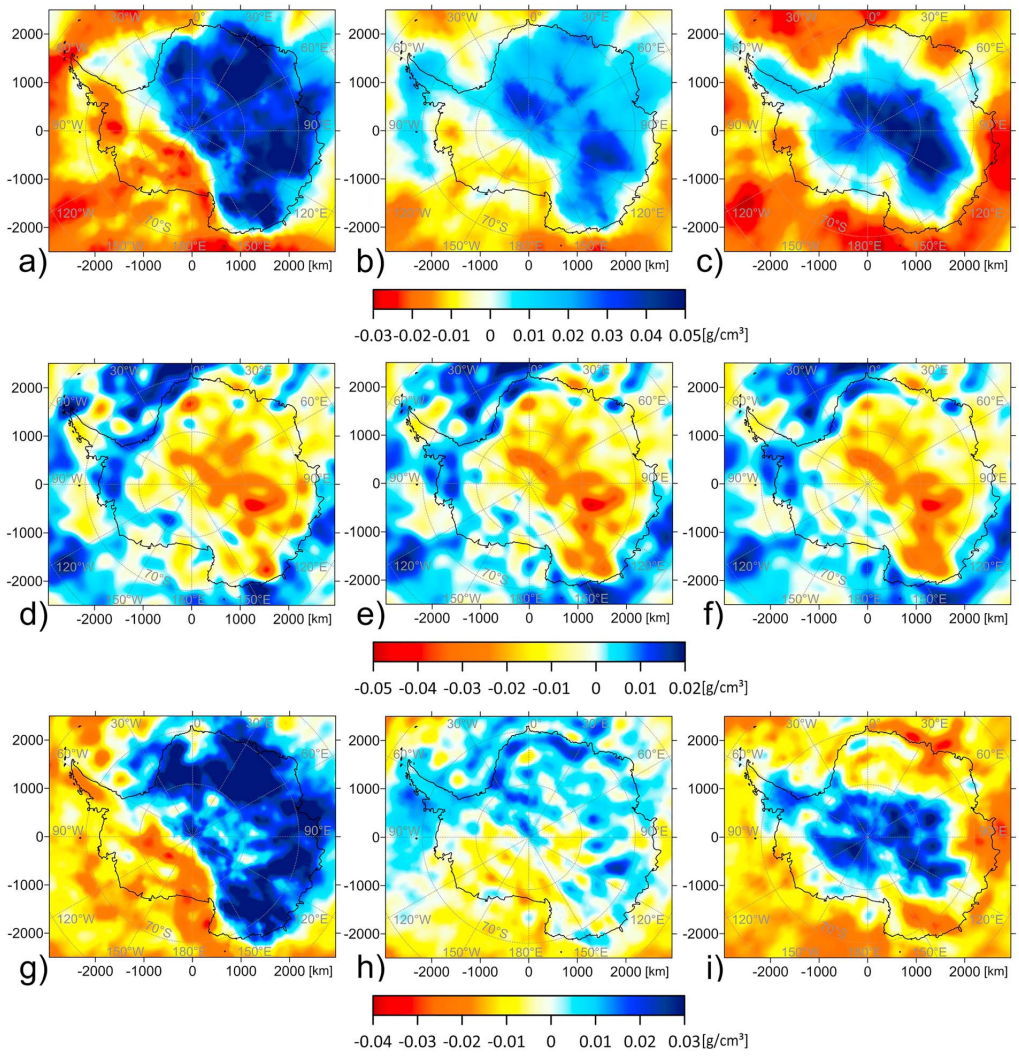

Figure 8. Density variations estimated for 100 (first column), 150 (second column), and 200 km (third column) based on the AN1-S tomography model. Panels (a)–(c) show thermal, (d)–(f) compositional, and (g)–(i) total density variations as obtained in the final iteration.

the Aurora Subglacial Basin. Variations on smaller scales are likely artifacts caused by the conversion into spherical harmonics during the inversion process and are dependent on the maximum degree and order used in the process. To limit the occurrence of artifacts but still retain a reasonable resolution, a maximum value of 120 degree and order was chosen.

Adding up both fields yields the total density variation within Antarctica (Figures 7g–7i and Figures 8g–8i). In the first model, the density distribution in 100-km depth spanning between −0.034 and 0.029 g/cm^3 resemble closely that of the residual gravity and the residual topography, indicating that density variations located in the uppermost mantle control these fields to a large extent. The distinction between EANT and WANT is reflected in the total density variations, as well, but is fading when density contrasts decrease at 200 km (−0.016–0.025 g/cm^3) and beyond. Over the majority of Antarctica, thermal density variations

Geochemistry, Geophysics, Geosystems 10.1029/2018GC008033

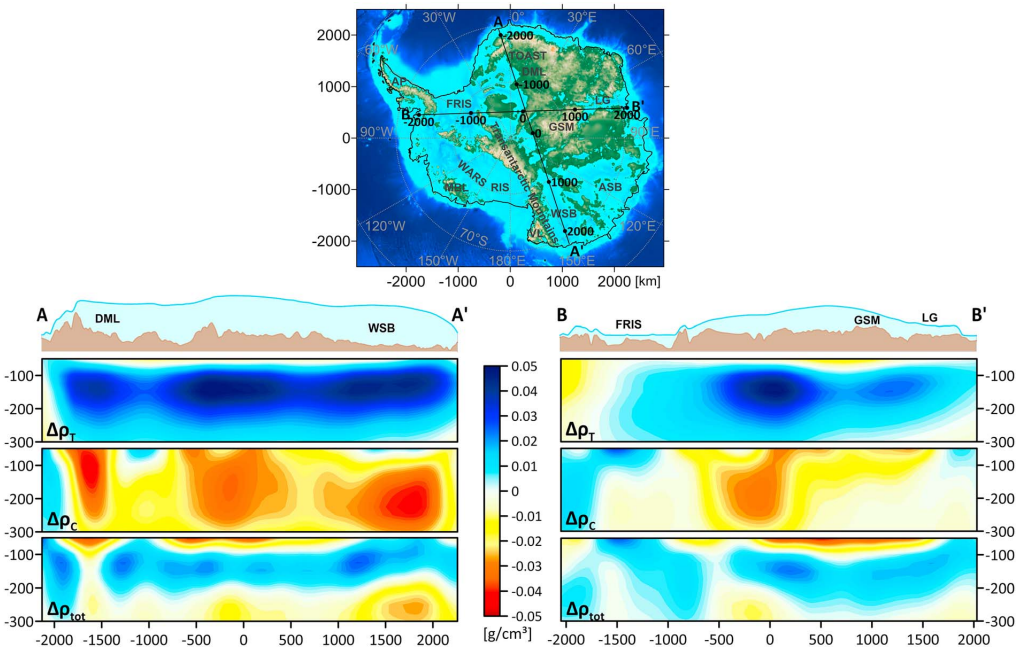

Figure 9. Bedrock topography (top) with location of two cross sections through the density variations calculated based on the SL2013sv model. First row = surface (blue) and bedrock (brown) topography, second row = thermal density variations, third row = compositional density variation, fourth row = total density variations, WSB = Wilkes Subglacial Basin; DML = Dronning Maud Land; GSM = Gamburtsev Subglacial Mountains; FRIS = Filchner-Ronne Ice Shelf; LG = Lambert Graben.

dominate in the total field, causing generally high density in EANT and low density in WANT. Only the strong minima in compositional density in Dronning Maud Land and close to the Pole are clearly reflected in the total field at a depth of 100 km. The model based on AN1-S is also strongly dominated by thermal density variations, especially at 100 (−0.037–0.067 g/cm^3) and 200 km (−0.036–0.38 g/cm^3) where anomalously low temperatures and hence high thermal density variations are estimated. A clear distinction between EANT and WANT is only visible at 100-km depth.

The cross sections (Figure 9) give a better idea about the depth extents of both thermal and compositional density variations. Within EANT, high thermal density features (> 0.026 g/cm^3) extend to depths between 200 and 250 km, while no such structures are visible for WANT, indicating significantly lower depth of the lithospheric root (<100 km). The roots of the (low) compositional density structures in EANT reach even deeper and are still visible below 250 km in Dronning Maud Land, central Antarctica, and in the Wilkes Subglacial Basin.

5.3. Composition

During the iterative process, we calculate not only temperature and density variations but also changes in composition in terms of Mg # for cratonic EANT. The resulting depletion variations for the above introduced representative depth slices are shown in Figure 10 based on the SL2013 model (panels a–c) and on the AN1-S model (panels d–f). The former exhibits strongest depletion in central Dronning Maud Land with up to Mg # = 92 in 100-km depth with another local maximum around the South Pole (Mg # = 91.3). Another highly depleted area can be found along the eastern flank of the Transantarctic Mountains with Mg # = 91.6 at 200 km. The Lambert Graben and Gamburtsev Subglacial Mountains as well as the Aurora Subglacial Basin on the other hand exhibit low to no depletion and preserve almost primitive mantle composition. These structures become increasingly clear with increasing depth. The model based on AN1-S shows similar yet weaker structures in Dronning Maud Land and around the South Pole. Maximum depletion can be found

Geochemistry, Geophysics, Geosystems 10.1029/2018GC008033

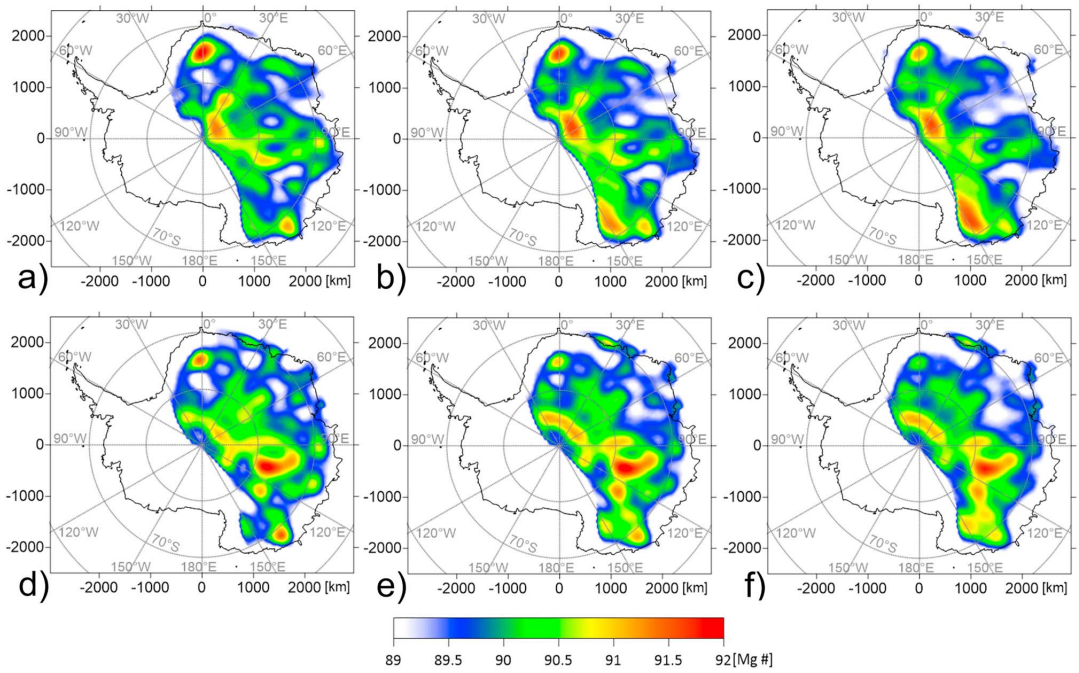

Figure 10. Depletion variations in terms of Mg # (100 × Mg/(Mg + Fe)) estimated for 100 (first column), 150 (second column), and 200 km (third column) based on the SL2013 tomography model (panels (a)–(c)) and on AN1-S model (panels (d)–(f)) as obtained in the final iteration.

in the central Aurora Subglacial Basin (Mg # = 91.9), though. In the vicinity of the Lambert Graben, an almost undepleted area is present but seems to be less distinct and shifted further toward Enderby Land in comparison with the SL2013 model. In contrast to the SL2013sv model, no such minimum exists around the Aurora Subglacial Basin.

6. Discussion

The joint inversion of gravity and tomography data allows us to get new insight into the lithospheric structures of Antarctica. The choice of the seismic tomography model used in the inversion strongly affects the results obtained in the iterative scheme. Both tomographic models used in this study stem from surface wave tomography but yield quite different amplitudes and local structures, likely caused by different data and inversion techniques. Especially at 200 km and below, the AN1-S model exhibits very high velocities in EANT, translating into temperatures that are far below the temperatures estimated for comparable cratonic regions derived from xenolith data (e.g., Griffin et al., 2004; Hasterok & Chapman, 2011), and can explain the differences with the model SL2013sv. In some regions like the western TAM, temperatures estimated using the AN1-S model even decrease with increasing depth. Furthermore, it causes the total density variations to be strongly dominated by thermal variations possibly masking compositional changes. Therefore, we conclude that the AN1-S model is not well suited for our study and the discussion will be focused on the analysis of the results obtained using the SL2013sv model.

WANT is characterized by very low variations in compositional density ($<\pm 0.015$ g/cm^3), indicating that the negative variations in residual gravity are chiefly induced by a hot upper mantle present in this region. In EANT, however, the negative residual density anomalies can no longer be explained by thermal variations alone. Here negative compositional density variations are necessary to explain the gravity observations, indicating high depletion in iron. Positive compositional density variations without equivalent expression in seismic velocity present in WANT can be explained by the presence of eclogite, which can cause an

Geochemistry, Geophysics, Geosystems 10.1029/2018GC008033

increase of the density from 3.3 to up to 3.5 g/cm^3 (e.g., Kurtz & Garland, 1976) while being seismically indistinguishable from peridotite. This hypothesis has been suggested by Tesauro et al. (2014) to explain the positive anomalies in the off-cratonic areas and is supported by petrological studies that found eclogite originated from the Ross orogeny in Northern Victoria Land (Godard & Palmeri, 2013, and Melchiorre et al., 2011), corresponding very well with the local maximum in compositional density in our study. Similar conditions can be argued for other continental sutures within WANT, yet no xenolith data exist in these regions to date due to poor exposure. EANT and WANT also differ strongly in lithospheric thickness. While WANT is characterized by lithospheric thickness well below 100 km, the thermal lithospheric root in EANT reaches values of >200 km.

Within EANT, several regions are characterized by both low temperatures and strongly negative compositional density variations, namely along the eastern flank of the Transantarctic Mountains with the strongest anomalies in the Wilkes Subglacial Basin and close to the South Pole and in central Dronning Maud Land, indicating the presence of Archean to Paleoproterozoic cratonic blocs. The Mawson craton located in Wilkes Land (Boger, 2011; Leitchenkov et al., 2016) is of such Archean to Paleoproterozoic origin and coincides well with the anomaly in the Wilkes Subglacial Basin. Based on xenolith data from the Miller Range, Boger (2011) further suggests a continuation of the Mawson Craton into EANT with a distinct fragment of Archean to Paleoproterozoic basement around the Nimrod Group, coinciding with the second abovementioned anomaly. Dronning Maud Land is a region of key importance when studying the formation and subsequent breakup of Gondwana as it played a central role in this process. Recent studies (e.g., Jacobs et al., 2015, 2017; Ruppel et al., 2018) found evidence that large parts of this region are characterized by juvenile early Mesoproterozoic to Neoproterozoic terranes that form part of the Tonian Oceanic Arc Super Terrane. These authors also suggest the presence of an unidentified terrane or craton. Since we find a structure with low temperature, negative compositional density, and high depletion there, we argue that this unidentified terrane is of Precambrian age. In these regions, compositional density variations also suggest a much deeper lithospheric root of over 250 km.

The Lambert Graben is characterized by low compositional density variation ($<\pm 0.01$ g/cm^3), low to no depletion in terms of Fe, and slightly elevated temperatures at shallow depth compared to its surroundings. Hence, rejuvenation of the lithospheric mantle must have taken place during the rifting process in this failed rift system. Two distinct phases of denudation have been suggested for the Lambert Graben (e.g., Lisker et al., 2003), one in the late Paleozoic coincident with the onset of rifting and one in the Cretaceous, that could account for such rejuvenation. The Aurora Subglacial Basin is characterized by similar conditions in the models based on SL2013sv but contains the strongest differences to the models based on AN1-S, which found negative compositional density anomalies and high depletion in its southernmost part. Boger (2011) interprets this region to be of Mesoproterozoic age. Additionally, the region is characterized by several large suture zones with the Indo-Australo-Antarctic Suture and the Aurora Fault being the largest and lying directly within the region of low depletion. They both represent tectonic boundaries that played a major role in the assembly and break-up of supercontinent Rodinia in Proterozoic times (Aitken et al., 2014, 2016). Paleozoic to Mesozoic reactivation possibly linked to the rifting activity in the East Antarctic Rift System (Aitken et al., 2014; Cianfarra & Maggi, 2017; Ferraccioli et al., 2011) may have caused further rejuvenation of this terrane, hence, supporting the results obtained using the SL2013sv model.

7. Conclusion

We combine gravity and seismic tomography data in an iterative inversion scheme to create a 3-D model of the Antarctic lithosphere that quantifies temperature, density, and compositional variations. The residual gravity and topography models were estimated using a new model of lateral density variations within the crust and an improved map of Moho depth variation, both created in this study. Temperature variations were calculated using a regional (AN1-S) and a global (SL2013sv) tomography model. We conclude that the choice of tomography model has a significant role when estimating lithospheric temperatures. Anomalously low velocities in WANT as well as anomalously high velocities in cratonic EANT at 200 km and below when using the AN1-S model leading to unrealistic temperature variations indicate a preference to the results obtained using SL2013sv for interpretation. Incorporating compositional changes into the temperature calculations raised the final temperatures by up to 150 °C.

Geochemistry, Geophysics, Geosystems 10.1029/2018GC008033

A clear distinction between EANT and WANT is visible in all parameters that have been investigated in this study. In WANT, the lithospheric root is very shallow (<100 km), and density variations predominantly stem from high upper mantle temperatures. Existing positive compositional density variations, for example, in Northern Victoria Land, are argued to be caused by the presence of eclogite. In EANT, both thermal and compositional density variations suggest a much deeper lithospheric root (>200 km). Furthermore, temperature variations alone are not sufficient to explain the residual gravity and topography variations and negative compositional density variations caused by high depletion in iron are required.

Several key regions in EANT are characterized by negative, compositional-induced density variations, indicating high depletion in iron and low temperatures. In Dronning Maud Land, recent studies (e.g., Jacobs et al., 2015, 2017) infer that the rejuvenated Tonian Oceanic Arc Super Terrane was terminated against an unidentified, possibly cratonic fragment that coincides well with one of the abovementioned regions ($T < 800$ °C, $\rho < -0.045$ g/cm^3, Mg # = 92), thus supporting their interpretation. The Mawson Craton in the Wilkes Subglacial Basin is characterized by similar conditions ($T < 650$ °C, $\rho < -0.041$ g/cm^3, Mg # = 91.6) and could possibly be linked to a low temperature and high depletion zone (also likely of cratonic origin) close to the South Pole ($T < 550$ °C, $\rho < -0.04$ g/cm^3, Mg # = 91.6).

Undepleted lithosphere is located in the Lambert Graben and in the Aurora Subglacial Basin. The former is a part of the East Antarctic Rift System (Ferraccioli et al., 2011), and its rejuvenation likely took place during the rifting process that might be as recent as the Cretaceous (Lisker et al., 2003). The process of rifting could be linked to the reactivation of the Indo-Australo-Antarctic Suture and the Aurora Fault, two major suture zones within the Aurora Subglacial Basin, thus explaining the low depletion as being due to the rejuvenation of the lithosphere in this region.

Acknowledgments
This study was supported by DFG (German Research Foundation), SPP-1788 Dynamic Earth (grants KA2669/4-1 and KA2669/4-2) and SPP-2017 (grant PE 2167/2-1). The 3-D thermal, density, and compositional models and the Moho depth variations are available in the supporting information.

References

Aitken, A. R. A., Betts, P. G., Young, D. A., Blankenship, D. D., Roberts, J. L., & Siegert, M. J. (2016). The Australo-Antarctic Columbia to Gondwana transition. *Gondwana Research*, *29*(1), 136–152. https://doi.org/10.1016/J.GR.2014.10.019

Aitken, A. R. A., Young, D. A., Ferraccioli, F., Betts, P. G., Greenbaum, J. S., Richter, T. G., et al. (2014). The subglacial geology of Wilkes Land, East Antarctica. *Geophysical Research Letters*, *41*, 2390–2400. https://doi.org/10.1002/2014GL059405

An, M., Wiens, D. A., Zhao, Y., Feng, M., Nyblade, A., Kanao, M., et al. (2015a). Temperature, lithosphere-asthenosphere boundary, and heat flux beneath the Antarctic Plate inferred from seismic velocities. *Journal of Geophysical Research: Solid Earth*, *120*, 8720–8742. https://doi.org/10.1002/2015JB011917

An, M., Wiens, D. A., Zhao, Y., Feng, M., Nyblade, A. A., Kanao, M., et al. (2015b). *S*-velocity model and inferred Moho topography beneath the Antarctic Plate from Rayleigh waves. *Journal of Geophysical Research: Solid Earth*, *120*, 359–383. https://doi.org/10.1002/2014JB011332

Baranov, A., & Morelli, A. (2013). The Moho depth map of the Antarctica region. *Tectonophysics*, *609*, 299–313. https://doi.org/10.1016/j.tecto.2012.12.023

Bayer, B., Geissler, W. H., Eckstaller, A., & Jokat, W. (2009). Seismic imaging of the crust beneath Dronning Maud Land, East Antarctica. *Geophysical Journal International*, *178*(2), 860–876. https://doi.org/10.1111/j.1365-246X.2009.04196.x

Behrendt, J. C. (1999). Crustal and lithospheric structure of the West Antarctic Rift System from geophysical investigations—A review. *Global and Planetary Change*, *23*(1–4), 25–44. https://doi.org/10.1016/S0921-8181(99)00049-1

Boger, S. D. (2011). Antarctica—Before and after Gondwana. *Gondwana Research*, *19*(2), 335–371. https://doi.org/10.1016/j.gr.2010.09.003

Burton-Johnson, A., Halpin, J. A., Whittaker, J. M., Graham, F. S., & Watson, S. J. (2017). A new heat flux model for the Antarctic Peninsula incorporating spatially variable upper crustal radiogenic heat production. *Geophysical Research Letters*, *44*, 5436–5446. https://doi.org/10.1002/2017GL073596

Cammarano, F., Goes, S., Vacher, P., & Giardini, D. (2003). Inferring upper-mantle temperatures from seismic velocities. *Physics of the Earth and Planetary Interiors*, *138*(3–4), 197–222. https://doi.org/10.1016/S0031-9201(03)00156-0

Chen, B., Haeger, C., Kaban, M. K., & Petrunin, A. G. (2017). Variations of the effective elastic thickness reveal tectonic fragmentation of the Antarctic lithosphere. *Tectonophysics*, *746*, 412–424. https://doi.org/10.1016/j.tecto.2017.06.012

Christensen, N. I., & Mooney, W. D. (1995). Seismic velocity structure and composition of the continental crust: A global view. *Journal of Geophysical Research*, *100*(B6), 9761–9788. https://doi.org/10.1029/95JB00259

Cianfarra, P., & Maggi, M. (2017). Cenozoic extension along the reactivated Aurora Fault System in the East Antarctic Craton. *Tectonophysics*, *703-704*, 135–143. https://doi.org/10.1016/j.tecto.2017.02.019

Dalziel, I. W. D., & Elliot, D. H. (1982). West Antarctica: Problem child of Gondwanaland. *Tectonics*, *1*(1), 3–19. https://doi.org/10.1029/TC001i001p00003

Danesi, S., & Morelli, A. (2001). Structure of the upper mantle under the Antarctic Plate from surface wave tomography. *Geophysical Research Letters*, *28*(23), 4395–4398. https://doi.org/10.1029/2001GL013431

Deschamps, F., Trampert, J., & Snieder, R. (2002). Anomalies of temperature and iron in the uppermost mantle inferred from gravity data and tomographic models. *Physics of the Earth and Planetary Interiors*, *129*(3-4), 245–264. https://doi.org/10.1016/S0031-9201(01)00294-1

Ebbing, J., Pappa, F., Ferraccioli, F., van der Wal, W., & Barletta, V. R. (2016). Deciphering the changes in the lithospheric structure of antarctica by combining seismological and satellite gravity gradient data. *AGU Fall Meeting Abstracts*.

Ferraccioli, F., Bell, R. E., Blankenship, D. D., Young, D. A., Eagles, G., Forsberg, R., et al. (2016). Revealing the crustal architecture of the least understood composite craton on Earth: East Antarctica. *AGU Fall Meeting Abstracts*.

Ferraccioli, F., Finn, C. a., Jordan, T., Bell, R. E., Anderson, L., & Damaske, S. (2011). East Antarctic rifting triggers uplift of the Gamburtsev Mountains. *Nature*, *479*(7373), 388–392. https://doi.org/10.1038/nature10566

Finotello, M., Nyblade, A., Julia, J., Wiens, D., & Anandakrishnan, S. (2011). Crustal V_P-V_S ratios and thickness for Ross Island and the Transantarctic Mountain front, Antarctica. *Geophysical Journal International*, *185*(1), 85–92. https://doi.org/10.1111/j.1365-246X.2011.04946.x

Förste, C., Bruinsma, S., Abrikosov, O., Flechtner, F., Marty, J.-C., Lemoine, J.-M., et al. (2014). EIGEN-6C4—The latest combined global gravity field model including GOCE data up to degree and order 1949 of GFZ Potsdam and GRGS Toulouse. *EGU General Assembly*, *16*, 3707. https://doi.org/https://doi.org/10.5880/icgem.2015.1

Forte, A. M., & Peltier, R. (1991). Viscous flow models of global geophysical observables: 1. Forward problems. *Journal of Geophysical Research*, *96*(B12), 20,131–20,159. https://doi.org/10.1029/91JB01709

Fretwell, P., Pritchard, H. D., Vaughan, D. G., Bamber, J. L., Barrand, N. E., Bell, R., et al. (2013). Bedmap2: Improved ice bed, surface and thickness datasets for Antarctica. *The Cryosphere*, *7*(1), 375–393. https://doi.org/10.5194/tc-7-375-2013

Godard, G., & Palmeri, R. (2013). High-pressure metamorphism in Antarctica from the Proterozoic to the Cenozoic: A review and geodynamic implications. *Gondwana Research*, *23*(3), 844–864. https://doi.org/10.1016/J.GR.2012.07.012

Godey, S., Deschamps, F., Trampert, J., & Snieder, R. (2004). Thermal and compositional anomalies beneath the North American continent. *Journal of Geophysical Research*, *109*, B01308. https://doi.org/10.1029/2002JB002263

Goodge, J. W. (2018). Crustal heat production and estimate of terrestrial heat flow in central East Antarctica, with implications for thermal input to the East Antarctic ice sheet. *The Cryosphere*, *12*(2), 491–504. https://doi.org/10.5194/tc-12-491-2018

Griffin, W. L., O'Reilly, S. Y., Doyle, B. J., Pearson, N. J., Coopersmith, H., Kivi, K., et al. (2004). Lithosphere mapping beneath the North American plate. *Lithos*, *77*(1-4), 873–922. https://doi.org/10.1016/j.lithos.2004.03.034

Harrowfield, M., Holdgate, G. R., Wilson, C. J. L., & McLoughlin, S. (2005). Tectonic significance of the Lambert graben, East Antarctica: Reconstructing the Gondwanan rift. *Geology*, *33*(3), 197–200. https://doi.org/10.1130/G21081.1

Hasterok, D., & Chapman, D. S. (2011). Heat production and geotherms for the continental lithosphere. *Earth and Planetary Science Letters*, *307*(1–2), 59–70. https://doi.org/10.1016/j.epsl.2011.04.034

Hole, M. J., & LeMasurier, W. E. (1994). Tectonic controls on the geochemical composition of Cenozoic, mafic alkaline volcanic rocks from West Antarctica. *Contributions to Mineralogy and Petrology*, *117*(2), 187–202. https://doi.org/10.1007/BF00286842

Huerta, A. D., & Harry, D. L. (2007). The transition from diffuse to focused extension: Modeled evolution of the West Antarctic rift system. *Earth and Planetary Science Letters*, *255*(1–2), 133–147. https://doi.org/10.1016/j.epsl.2006.12.011

Jackson, I., Fitz Gerald, J. D., Faul, U. H., & Tan, B. H. (2002). Grain-size-sensitive seismic wave attenuation in polycrystalline olivine. *Journal of Geophysical Research*, *107*(B12), 2360. https://doi.org/10.1029/2001JB001225

Jacobs, J., Elburg, M., Läufer, A., Kleinhanns, I. C., Henjes-Kunst, F., Estrada, S., et al. (2015). Two distinct Late Mesoproterozoic/Early Neoproterozoic basement provinces in central/eastern Dronning Maud Land, East Antarctica: The missing link, 15–21°E. *Precambrian Research*, *265*, 249–272. https://doi.org/10.1016/j.precamres.2015.05.003

Jacobs, J., Opås, B., Elburg, M. A., Läufer, A., Estrada, S., Ksienzyk, A. K., et al. (2017). Cryptic sub-ice geology revealed by a U-Pb zircon study of glacial till in Dronning Maud Land, East Antarctica. *Precambrian Research*, *294*, 1–14. https://doi.org/10.1016/j.precamres.2017.03.012

Janik, T., Grad, M., Guterch, A., & Środa, P. (2014). The deep seismic structure of the Earth's crust along the Antarctic Peninsula—A summary of the results from Polish geodynamical expeditions. *Global and Planetary Change*, *123*, 213–222. https://doi.org/10.1016/j.gloplacha.2014.08.018

Kaban, M. K., El Khrepy, S., & Al-Arifi, N. (2016a). Isostatic model and isostatic gravity anomalies of the Arabian Plate and surroundings. *Pure and Applied Geophysics*, *173*(4), 1211–1221. https://doi.org/10.1007/s00024-015-1164-0

Kaban, M. K., Mooney, W. D., & Petrunin, A. G. (2015). Cratonic root beneath North America shifted by basal drag from the convecting mantle. *Nature Geoscience*, *8*(10), 797–800. https://doi.org/10.1038/ngeo2525

Kaban, M. K., & Schwintzer, P. (2001). Oceanic upper mantle structure from experimental scaling of *VS* and density at different depths. *Geophysical Journal International*, *147*(1), 199–214. https://doi.org/10.1046/j.0956-540x.2001.01520.x

Kaban, M. K., Schwintzer, P., & Reigber, C. (2004). A new isostatic model of the lithosphere and gravity field. *Journal of Geodesy*, *78*(6), 368–385. https://doi.org/10.1007/s00190-004-0401-6

Kaban, M. K., Stolk, W., Tesauro, M., El Khrepy, S., Al-Arifi, N., Beekman, F., & Cloetingh, S. A. P. L. (2016b). 3D density model of the upper mantle of Asia based on inversion of gravity and seismic tomography data. *Geochemistry, Geophysics, Geosystems*, *17*, 4457–4477. https://doi.org/10.1002/2016GC006458

Kaban, M. K., Tesauro, M., Mooney, W. D., & Cloetingh, S. A. P. L. (2014). Density, temperature, and composition of the North American lithosphere—New insights from a joint analysis of seismic, gravity, and mineral physics data: 1. Density structure of the crust and upper mantle. *Geochemistry, Geophysics, Geosystems*, *15*, 4781–4807. https://doi.org/10.1002/2014GC005483

Kanao, M., & Shibutani, T. (2012). Shear wave velocity models beneath Antarctic margins inverted by genetic algorithm for teleseismic receiver functions. In M. Kanao (Ed.), *Seismic waves—Research and analysis* (pp. 237–252). InTech. https://doi.org/10.5772/32130

Khan, A., Zunino, A., & Deschamps, F. (2013). Upper mantle compositional variations and discontinuity topography imaged beneath Australia from Bayesian inversion of surface-wave phase velocities and thermochemical modeling. *Journal of Geophysical Research: Solid Earth*, *118*, 5285–5306. https://doi.org/10.1002/jgrb.50304

Kuge, K., & Fukao, Y. (2005). High-velocity lid of East Antarctica: Evidence of a depleted continental lithosphere. *Journal of Geophysical Research*, *110*, B06309. https://doi.org/10.1029/2004JB003382

Kumar, P., Talukdar, K., & Sen, M. K. (2014). Lithospheric structure below transantarctic mountain using receiver function analysis of TAMSEIS data. *Journal of the Geological Society of India*, *83*(5), 483–492. https://doi.org/10.1007/s12594-014-0075-5

Kurtz, R. D., & Garland, G. D. (1976). Magnetotelluric measurements in eastern Canada. *Geophysical Journal of the Royal Astronomical Society*, *45*(2), 321–347. https://doi.org/10.1111/j.1365-246X.1976.tb00329.x

Lamarque, G., Barruol, G., Fontaine, F. R., Bascou, J., & Menot, R.-P. (2015). Crustal and mantle structure beneath the Terre Adelie Craton, East Antarctica: Insights from receiver function and seismic anisotropy measurements. *Geophysical Journal International*, *200*(2), 807–821. https://doi.org/10.1093/gji/ggu430

Laske, G., & Masters, G. (2013). Update on CRUST1. 0—A 1-degree global model of Earth's crust. *EGU General Assembly*, *15*, 2658. Retrieved from http://meetingorganizer.copernicus.org/EGU2013/EGU2013-2658.pdf

Lee, C.-T. A. (2003). Compositional variation of density and seismic velocities in natural peridotites at STP conditions: Implications for seismic imaging of compositional heterogeneities in the upper mantle. *Journal of Geophysical Research*, *108*(B9), 2441. https://doi.org/10.1029/2003JB002413

Leitchenkov, G. L., Antonov, A. V., Luneov, P. I., & Lipenkov, V. Y. (2016). Geology and environments of subglacial Lake Vostok. *Philosophical Transactions of the Royal Society A: Mathematical, Physical and Engineering Sciences*, *374*(2059), 20140302. https://doi.org/10.1098/rsta.2014.0302

Lisker, F., Brown, R., & Fabel, D. (2003). Denudational and thermal history along a transect across the Lambert Graben, northern Prince Charles Mountains, Antarctica, derived from apatite fission track thermochronology. *Tectonics*, *22*(5), 1055. https://doi.org/10.1029/2002TC001477

Maule, C. F., Purucker, M. E., Olsen, N., & Mosegaard, K. (2005). Heat flux anomalies in Antarctica revealed by satellite magnetic data. *Science*, *309*(5733), 464–467. https://doi.org/10.1126/science.1106888

Melchiorre, M., Coltorti, M., Bonadiman, C., Faccini, B., O'Reilly, S. Y., & Pearson, N. J. (2011). The role of eclogite in the rift-related metasomatism and Cenozoic magmatism of Northern Victoria Land, Antarctica. *Lithos*, *124*(3–4), 319–330. https://doi.org/10.1016/J.LITHOS.2010.11.012

Miyamachi, H., Toda, S., Matsushima, T., & Takada, M. (2003). Seismic refraction and wide-angle reflection exploration by JARE-43 on Mizuho Plateau, East Antarctica. *Polar Geoscience*, *16*, 1–21.

Mooney, W. D., & Kaban, M. K. (2010). The North American upper mantle: Density, composition, and evolution. *Journal of Geophysical Research*, *115*, B12424. https://doi.org/10.1029/2010JB000866

Morelli, A., & Danesi, S. (2004). Seismological imaging of the Antarctic continental lithosphere: A review. *Global and Planetary Change*, *42*(1-4), 155–165). https://doi.org/10.1016/j.gloplacha.2003.12.005

O'Donnell, J. P., & Nyblade, A. A. (2014). Antarctica's hypsometry and crustal thickness: Implications for the origin of anomalous topography in East Antarctica. *Earth and Planetary Science Letters*, *388*, 143–155. https://doi.org/10.1016/j.epsl.2013.11.051

Owada, M., Kamei, A., Horie, K., Shimura, T., Yuhara, M., Tsukada, K., et al. (2013). Magmatic history and evolution of continental lithosphere of the Sør Rondane Mountains, eastern Dronning Maud Land, East Antarctica. *Precambrian Research*, *234*, 63–84. https://doi.org/10.1016/j.precamres.2013.02.007

Pappa, F., Ebbing, J., Ferraccioli, F., van der Wal, W., & Blank, B. (2018). A 3D lithospheric model of Antarctica and its implications on mantle viscosity. In *EGU General Assembly Conference Abstracts* (Vol. 20, p. 4939).

Petrunin, A. G., Kaban, M. K., Rogozhina, I., & Trubitsyn, V. (2013). Revising the spectral method as applied to modeling mantle dynamics. *Geochemistry, Geophysics, Geosystems*, *14*, 3691–3702. https://doi.org/10.1002/ggge.20226

Petrunin, A. G., Rogozhina, I., Vaughan, A. P. M., Kukkonen, I. T., Kaban, M. K., Koulakov, I., & Thomas, M. (2013). Heat flux variations beneath central Greenland's ice due to anomalously thin lithosphere. *Nature Geoscience*, *6*(9), 746–750. https://doi.org/10.1038/ngeo1898

Powell, C. M., Roots, S. R., & Veevers, J. J. (1988). Pre-breakup continental extension in East Gondwanaland and the early opening of the eastern Indian Ocean. *Tectonophysics*, *155*(1–4), 261–283. https://doi.org/10.1016/0040-1951(88)90269-7

Rabbel, W., Kaban, M., & Tesauro, M. (2013). Contrasts of seismic velocity, density and strength across the Moho. *Tectonophysics*, *609*, 437–455. https://doi.org/10.1016/j.tecto.2013.06.020

Ruppel, A., Jacobs, J., Eagles, G., Läufer, A., & Jokat, W. (2018). New geophysical data from a key region in East Antarctica: Estimates for the spatial extent of the Tonian Oceanic Arc Super Terrane (TOAST). *Gondwana Research*, *59*(c), 97–107. https://doi.org/10.1016/j.gr.2018.02.019. https://doi.org/10.1016/j.gr.2018.02.019

Schaeffer, A. J., & Lebedev, S. (2013). Global shear speed structure of the upper mantle and transition zone. *Geophysical Journal International*, *194*(1), 417–449. https://doi.org/10.1093/gji/ggt095

Schaffer, J., Timmermann, R., Arndt, J. E., Steinhage, D., & Kanzow, T. (2014). RTopo-2: A global dataset of ice sheet topography, cavity geometry and ocean bathymetry to study ice-ocean interactions in Northeast Greenland. *REKLIM Conference "Our Climate - Our Future", Berlin, Germany, 6 October 2014–9 October 2014*. Retrieved from http://epic.awi.de/37733/#.WFFkhlNeaOA.mendeley

Scheinert, M., Ferraccioli, F., Schwabe, J., Bell, R., Studinger, M., Damaske, D., et al. (2016). New Antarctic gravity anomaly grid for enhanced geodetic and geophysical studies in Antarctica. *Geophysical Research Letters*, *43*, 600–610. https://doi.org/10.1002/2015GL067439

Shapiro, N. M., & Ritzwoller, M. H. (2004). Inferring surface heat flux distributions guided by a global seismic model: Particular application to Antarctica. *Earth and Planetary Science Letters*, *223*(1–2), 213–224. https://doi.org/10.1016/j.epsl.2004.04.011

Simmons, N. A., Forte, A. M., & Grand, S. P. (2009). Joint seismic, geodynamic and mineral physical constraints on three-dimensional mantle heterogeneity: Implications for the relative importance of thermal versus compositional heterogeneity. *Geophysical Journal International*, *177*(3), 1284–1304. https://doi.org/10.1111/j.1365-246X.2009.04133.x

Steinberger, B., & Calderwood, A. R. (2006). Models of large-scale viscous flow in the Earth's mantle with constraints from mineral physics and surface observations. *Geophysical Journal International*, *167*(3), 1461–1481. https://doi.org/10.1111/j.1365-246X.2006.03131.x

Stixrude, L., & Lithgow-Bertelloni, C. (2005). Thermodynamics of mantle minerals - I. Physical properties. *Geophysical Journal International*, *162*(2), 610–632. https://doi.org/10.1111/j.1365-246X.2005.02642.x

Stolk, W., Kaban, M., Beekman, F., Tesauro, M., Mooney, W. D., & Cloetingh, S. (2013). High resolution regional crustal models from irregularly distributed data: Application to Asia and adjacent areas. *Tectonophysics*, *602*, 55–68. https://doi.org/10.1016/j.tecto.2013.01.022

ten Brink, U., & Stern, T. (1992). Rift flank uplifts and hinterland basins—Comparison of the Transantarctic Mountains with the great escarpment of southern Africa. *Journal of Geophysical Research*, *97*(B1), 569–585. https://doi.org/10.1029/91JB02231

Tesauro, M., Audet, P., Kaban, M. K., Bürgmann, R., & Cloetingh, S. (2012). The effective elastic thickness of the continental lithosphere: Comparison between rheological and inverse approaches. *Geochemistry, Geophysics, Geosystems*, *13*, Q09001. https://doi.org/10.1029/2012GC004162

Tesauro, M., Kaban, M. K., & Cloetingh, S. A. P. L. (2010). Thermal and rheological model of the European lithosphere. In S. Cloetingh & J. Negendank (Eds.), *New frontiers in integrated solid earth sciences* (pp. 71–101). Dordrecht: Springer Netherlands. https://doi.org/10.1007/978-90-481-2737-5_3

Tesauro, M., Kaban, M. K., Mooney, W. D., & Cloetingh, S. A. P. L. (2014). Density, temperature, and composition of the North American lithosphere—New insights from a joint analysis of seismic, gravity, and mineral physics data: 2. Thermal and compositional model of the upper mantle. *Geochemistry, Geophysics, Geosystems*, *15*, 4808–4830. https://doi.org/10.1002/2014GC005484

van Wijk, J. W., Lawrence, J. F., & Driscoll, N. W. (2008). Formation of the Transantarctic Mountains related to extension of the West Antarctic Rift System. *Tectonophysics*, *458*(1–4), 117–126. https://doi.org/10.1016/j.tecto.2008.03.009

Veevers, J. J. (2007). Pan-Gondwanaland post-collisional extension marked by 650-500 Ma alkaline rocks and carbonatites and related detrital zircons: A review. *Earth-Science Reviews*, *83*(1-2), 1–2), 1–47. https://doi.org/10.1016/j.earscirev.2007.03.001

Context

In the previous two studies, the characterization of the Antarctic lithosphere was primarily based on gravitiy field analysis which yields highly non-unique solutions. Therefore, in order to obtain reliable results, effect separation is crucial. A priori information is employed to correct the total gravity field for known structures and loads. Aiming to retrieve information from the upper mantle gravity field, influences of the deep mantle, the crust and surface loads have to be deducted. For the crustal correction, sediment deposits are a crucial factor to consider, as their low density can lead to errors in the residual gravity field if no sufficient correction is applied. However, due to the thick ice cover impeding direct measurements, accurate knowledge about sediment thickness and distribution are still sparse for Antarctica, causing large uncertainties in the determinations made previously.
Sediment distribution is also essential when modeling ice dynamics. It affects the geothermal heat flux estimated from a lithospheric thermal model because of changes in thermal conductivity compared to the crystalline crust and additional radiogenic heat production (e.g. Della Vedova and Von Herzen, 1987). Such a model can be calculated from the results of the second study (chapter 5). It also has direct implications on ice streaming. Geophysical studies have shown, that the presence of subglacial sediments facilitates ice flow and influences the onset of streaming (e.g., Smith et al., 2013).
Decompensative gravity anomalies can offer insight into upper crustal structures including sediment distribution in case of local compensation (Zorin et al., 1985; Cordell et al., 1991). The first study (chapter 4) however shows, that the effective elastic thickness varies strongly over Antarctica indicating changes from local to regional compensation. Kaban et al. (2016a) expanded the method to consider varying T_e over the study region. Therefore, the variations of T_e obtained in this first study represent crucial input data for the determination of upper crustal structures using decompensative gravity anomalies. The Moho serves as the compensation level in calculating the isostatic gravity, which is the basis for the decompensative anomaly calculation. Hence, we employ the Moho depth determinations calculated in the second study (chapter 5) to improve the decompensative corrections. Based on the results of the previous two studies, we estimate sediment deposits below the

ice shield from decompensative gravity anomalies over the Antarctic continent in the third study. These (qualitative) estimates will help to assess and reduce the uncertainties caused by upper crustal structures and sediments in future studies.

6 | Decompensative gravity anomalies reveal the structure of the upper crust of Antarctica

Chapter abstract

As Antarctica is almost entirely covered by thick ice shields impeding in-situ measurements, information about upper crustal structures and sedimentary basins is still sparse and the analysis of the gravity anomalies offers new insights. Isostatic gravity anomalies are often used to investigate upper crust structures. However, compensating masses significantly reduce the gravity effect of unknown sedimentary and upper crustal structures. To separate these effects, we apply so-called decompensative corrections to the isostatic anomalies for the Antarctic continent, which reach values of up to ±70 mGal. The obtained decompensative anomalies well correspond to the known sedimentary basins, such as in the areas of the Filchner-Ronne Ice Shelf and Lambert Graben, and also suggest the existence of other large sedimentary deposits both in West and East Antarctica, which are not or only sparsely mapped by existing seismic surveys, e.g. in coastal Dronning Maud Land and Enderby Land. A dipole-like structure exists at the Transantarctic Mountains and the Wilkes Subglacial Basin, suggesting the presence of isostatic disturbances linked to the dynamic uplift of the Transantarctic Mountains and thick sedimentary accumulations in the east. Extended positive anomalies in East Antarctica are likely related to the old and dense cratonic crust as well as to isostatic disturbances caused by the transition from local to regional compensation around the Lambert Graben.

Published manuscript:

Haeger, C. and Kaban, M. K. (2019). Decompensative gravity anomalies reveal the structure of the upper crust of Antarctica. *Pure and Applied Geophysics*.
http://dx.doi.org/10.1007/s00024-019-02212-5

6.1. Introduction

In recent years, big efforts have been made to unveil the structure of the Antarctic crust and lithosphere using a variety of geophysical measurements. However, in-situ measurements are strongly hindered by the ice shield covering 99% of the continent with thicknesses of up to 4.5 km (Fig. 6.1b). Hence, knowledge of upper crustal structures and sediment distribution is still limited, especially in central Antarctica. In particular, thickness and properties of sediments also impact ice dynamics by influencing basal controls and likely facilitating the onset of streaming flow (Smith et al., 2013). Therefore, several studies about sediment distribution were conducted below ice streams (e.g. Bamber et al., 2006; Bell et al., 1998). Significant amounts of sediments were also discovered below ice shelves with up to 8 km in the Ross Ice Shelf (e.g. Trey et al., 1999; Wobbe et al., 2014) or up to 14 km in the Filchner-Ronne Ice Shelf (e.g. Hübscher et al., 1996; Leitchenkov and Kudryavtzev, 1997), in the Wilkes Subglacial Basin (up to 7 km, Frederick et al., 2016) and in the Adventure Trench ($\sim$ 10 km Ferraccioli et al., 2001) using mainly gravity, magnetic and seismic data. Aitken et al. (2014) used gravity signals and depth to magnetic basement to detect several sediment basins within Wilkes Land. Global information about sediment thickness are available from CRUST1.0 (Laske and Masters, 2013), however, data coverage over Antarctica is sparse. Baranov et al. (2018) compiled existing surveys to create an Antarctica-wide map of sediment thickness but were still faced with large gaps in data in the continental interior that they filled by using a numerical interpolation scheme involving bedrock topography information (Fretwell et al., 2013).

Gravity anomalies have been used successfully before for investigation of density structures of the upper crust in other continents. Commonly, the isostatic anomalies of the gravity field are employed for these purposes since the effect of deep density variations can be effectively reduced from the observed field by applying the isostatic correction (e.g. Simpson et al., 1986; Blakely, 1995). The isostatic anomalies are computed by subtracting the effect of the deep density variations from the Bouguer gravity anomalies, i.e. associated with Moho undulations that balance the topography load according to an expected isostatic compensation model (e.g. Simpson et al., 1986). If the principal parameters of the compensating scheme, chiefly the depth of the compensation and the effective elastic thickness of the lithosphere, are chosen correctly, the local and mid-wave components of the residual isostatic anomalies should reflect the density structure of the upper crust. The long-wavelength anomalies, which reflect the effects of the mantle convection and glacial-isostatic adjustment, can be easily filtered out from the residual field (Kaban et al., 2004). The isostatic anomalies

were often used for investigations of sedimentary basins all over the World, e.g. in Nevada (Jachens and Moring, 1990), the Los Angeles Basin (Langenheim and Jachens, 1996) and Barents Sea (Ebbing et al., 2007). In Antarctica, the isostatic gravity anomalies constrained with other geophysical data sets such as aeromagnetic measurements have been analyzed to infer thickness of sediments across the Wilkes Subglacial Basin (Frederick et al., 2016). Unfortunately, the isostatic anomalies don't reveal the full effect of the upper crust heterogeneity. These structures are also isostatically compensated (locally or regionally); therefore, the gravity effect is substantially reduced by the opposing effect of the compensating masses, especially for wide sedimentary basins (Cordell et al., 1991). To refine the gravity field induced by the upper crust heterogeneity, a decompensative correction has been suggested by Zorin et al. (1985) and Cordell et al. (1991), which should be applied to the isostatic anomalies. The decompensative gravity anomalies were then employed for study of the density structure of the upper crust in the New Madrid seismic zone and Missouri gravity low (Hildenbrand et al., 1996), the Rio Grande rift (Cordell et al., 1991; Wilson et al., 2005) and sedimentary basins in South Siberia and Mongolia (e.g. Zorin et al., 1993). Recently, the decompensative gravity anomalies were calculated to study the structure of the upper crust of the Arabian plate and surroundings (Kaban et al., 2017). As was demonstrated in the last paper, the decompensative anomalies are very sensitive to the actual isostatic model and especially to the effective elastic thickness (T_e) of the lithosphere. Variations of T_e have been recently determined for the whole Antarctic continent using the new high resolution data on bedrock topography, ice thickness and on the gravity field based on recent satellite missions and available terrestrial observations (Chen et al., 2018). Furthermore, new Moho models, which are also required for accurate determination of the isostatic and decompensative corrections, have appeared in the last years (An et al., 2015b; Baranov et al., 2018; Haeger et al., 2019). These results provide a solid basis for computation of the isostatic and decompensative anomalies for Antarctica.

In the present study, we calculate the decompensative gravity anomalies for the whole Antarctic continent and use them to investigate the structure of the upper crust and particularly for determination of the sediments thickness in the basins, which are still hidden under the ice shield.

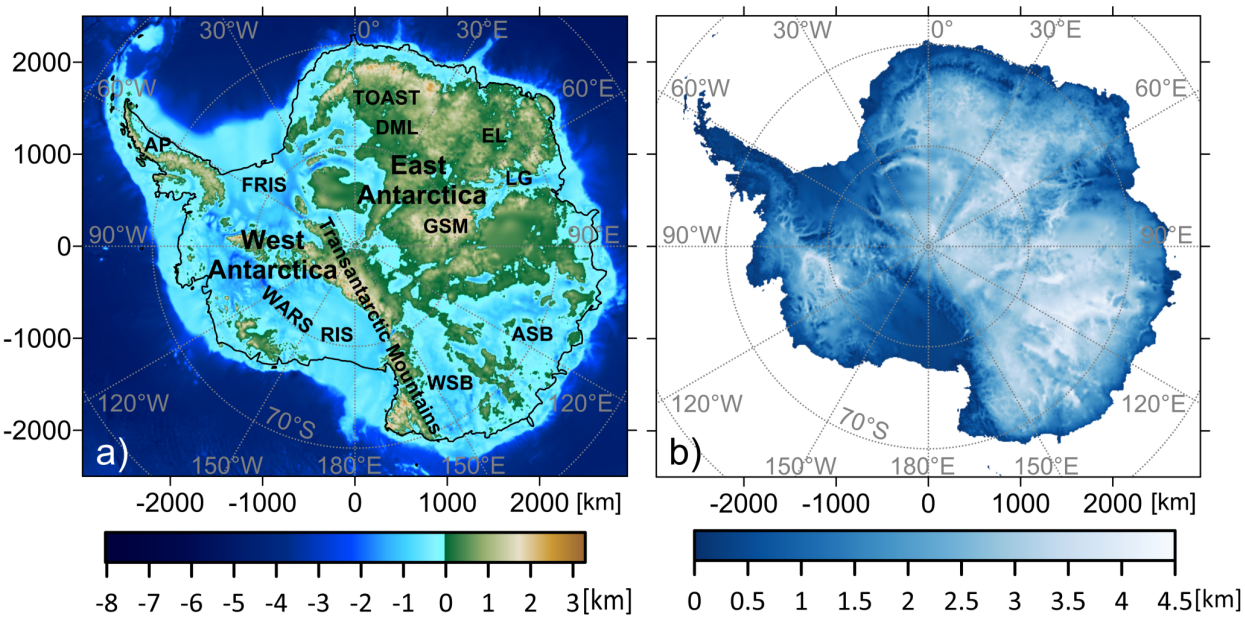

Figure 6.1.: **(a)** Bedrock topography of Antarctica (Fretwell et al., 2013) and bathymetry of the surrounding ocean (Schaffer et al., 2014). Key tectonic units: AP - Antarctic Peninsula, ASB - Aurora Subglacial Basin, DML - Dronning Maud Land, EL – Enderby Land, FRIS - Filchner-Ronne Ice Shelf, GSM - Gamburtsev Subglacial Mountains, LG - Lambert Glacier, RIS - Ross Ice Shelf, TOAST - Tonian Oceanic Arc Super Terrane, WARS - West Antarctic Rift System, WSB - Wilkes Subglacial Basin and **(b)** ice thickness (Fretwell et al., 2013)

6.2. Tectonic settings of Antarctica and initial data

6.2.1. Tectonic settings

Antarctica can be divided in two tectonically very different regions: East Antarctica (EANT) is of mostly Precambrian cratonic origin with a thick and cold lithosphere, while West Antarctica (WANT) consists of several crustal micro-blocs that only reached its present day shape in the Cenozoic and is characterized by notably thinner and hotter lithosphere (Danesi and Morelli, 2001; Haeger et al., 2019). The two regions are divided by the Transantarctic Mountains, a 3500 km long and 200 km wide mountain chain with elevations of up to 4500 m (Fretwell et al., 2013). While they were not uplifted by subduction or contraction (Morelli and Danesi, 2004; ten Brink and Stern, 1992), the exact uplift mechanism is still debated (e.g. Behrendt, 1999; ten Brink and Stern, 1992; van Wijk et al., 2008). EANT consists of several subglacial orogens, basins and rifts. A big plateau spans 0°-100°E and includes Dronning Maud Land, which held a key position in Gondwana formation and break-up. It

includes the Archean Grunehogna craton and the juvenile Neoproterozoic remnants of the Mozambique Ocean called the Tonian Oceanic Arc Super Terrane (Jacobs et al., 2015). The plateau is interrupted by the Lambert Graben, a Mesozoic failed rift system (Lisker et al., 2003) filled by a glacier that is suggested to hold large amounts of sediments (Baranov et al., 2018). With elevations of over 1 km below sea level, the Wilkes Subglacial Basin is one of the most notable basin structures in EANT. In comparison, most of WANT exhibits bedrock topography below sea level, with the most important feature being the West Antarctic Rift System, a 750-1000 km long, mostly aseismic rift system (O'Donnell and Nyblade, 2014). The bedrock topography with superimposed names of tectonic key regions is displayed in Fig. 6.1a.

6.2.2. Initial data

In order to obtain the free air gravity field, we combine the EIGEN-6C4 model (Förste et al., 2014), containing terrestrial and satellite data from GRACE, GOCE, and LAGEOS with the purely terrestrial AntGG model (Scheinert et al., 2016). The maximum resolution for EIGEN-6C4 is 2190 spherical harmonics degree and order, but actual resolution varies locally depending on the ground data included in the gravity field model. For Antarctica, this limits the resolution to approximately 200 km (Chen et al., 2018). The AntGG model is a compilation of 13 million data points from ground-based, shipborne, and airborne gravity surveys covering 73% of Antarctica at a resolution of 10 km. Therefore, each model provides reliable data at different wavelengths: we employ the Eigen-6C4 model for $\lambda > 250\,\mathrm{km}$, since it lacks high resolution information but provides continent-wide coverage on long wavelengths and the AntGG model for $\lambda < 150\,\mathrm{km}$, since it offers high resolution information with large gaps in coverage distorting long wavelength signals (Chen et al., 2018; Haeger et al., 2019). A gradual transition is employed for $150\,\mathrm{km} < \lambda < 250\,\mathrm{km}$.
Subsequently, we calculate the Bouguer gravity field displayed in Fig. 6.2a by removing the effect of topography and of the ice and water columns. The gravity effect of each load was calculated according to (Kaban et al., 2016a) using the reference densities $\rho_\mathrm{w} = 1.03\,\mathrm{g/cm^3}$ for water, $\rho_\mathrm{t} = 2.67\,\mathrm{g/cm^3}$ for the topography and a constant ice density of $\rho_\mathrm{i} = 0.92\,\mathrm{g/cm^3}$ (Chen et al., 2018) within a 2° (222.4 km) radius around each grid point. We further calculate the adjusted topography t_adj displayed in Fig. 6.2b by compressing the ice and water columns to ρ_t:

$$t_\mathrm{adj} = t_\mathrm{b} + \frac{\rho_\mathrm{w}}{\rho_\mathrm{t}} t_\mathrm{w} + \frac{\rho_\mathrm{i}}{\rho_\mathrm{t}} t_\mathrm{i} \tag{6.1}$$

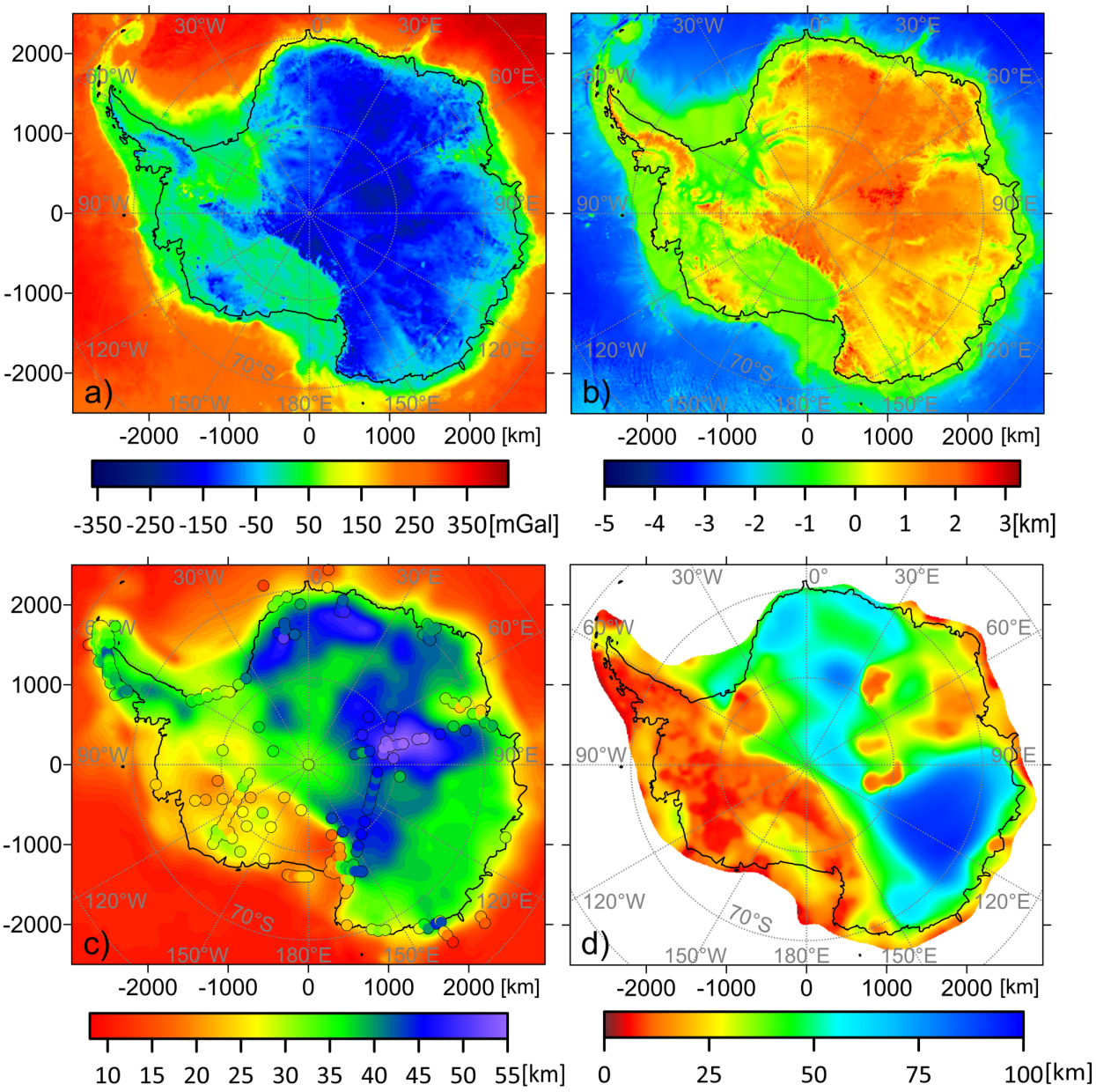

Figure 6.2.: **(a)** Full Bouguer gravity anomalies and **(b)** adjusted topography calculated with respect to the reference density for the uppermost crust of 2.67 g/cm^3. **(c)** Map of the Moho depth with superimposed determinations from refraction, reflection, and receiver function data (circles) (An et al., 2015b; Janik et al., 2014; Lamarque et al., 2015). **(d)** Variations of T_e obtained using the coherence method with a central wavenumber of the Morlet wavelet of 3.773 (Chen et al., 2018)

where t_b is the bedrock topography and t_w and t_i are the thickness of the water and ice column, respectively. The extent of each load was determined using surface elevation, ice

thickness and bedrock topography south of 60°S from Bedmap2 (Fretwell et al., 2013) and bathymetry from RTopo-2 (Schaffer et al., 2014) north of 60°S. Initial resolution of the Bedmap2 grids varies with location between 1 and 5 km, which was adjusted to a constant 10 km grid spacing in the calculations.
The calculation of the decompensative gravity anomaly requires information on the Moho depth (Fig. 6.2c) and effective elastic thickness variation T_e (Fig. 6.2d). We use the map of Moho depth variation by Haeger et al. (2019). They interpolate Moho depths from receiver function, reflection and refraction measurements within a 150 km radius and fill the remaining gaps using Moho depth constraints from surface wave tomography. The T_e variations used in this study (Chen et al., 2018) were calculated based on the coherence of Bouguer gravity and topography adjusted for variations of bedrock topography and ice thickness using cross-spectral analysis methods employing the fan wavelet technique (Kirby and Swain, 2004, 2011).

6.3. Decompensative gravity anomalies

6.3.1. Isostatic gravity anomalies

In the first stage, the isostatic gravity anomalies have been determined for Antarctica and surrounding areas. In the spectral domain, the isostatic correction can be formulated as the following (Kaban et al., 2016a):

$$\Delta g_{\mathrm{ic}}(k_{\mathrm{x}}, k_{\mathrm{y}}) = G_{\mathrm{is}}(k_{\mathrm{x}}, k_{\mathrm{y}}) \cdot t_{\mathrm{adj}}(k_{\mathrm{x}}, k_{\mathrm{y}}) = -2\pi G\rho C \cdot \exp(-k \cdot M) \cdot t_{\mathrm{adj}}(k_{\mathrm{x}}, k_{\mathrm{y}}) \,, \tag{6.2}$$

where $k = \sqrt{(k_{\mathrm{x}}^2 + k_{\mathrm{y}}^2)}$ is the wavenumber, $k_{\mathrm{x}} = 2\pi/\lambda_{\mathrm{x}}$ and $k_{\mathrm{y}} = 2\pi/\lambda_{\mathrm{y}}$, G is the gravitational constant, M is the Moho depth, which is chiefly associated with the isostatic compensation depth, t_{adj} is the adjusted topography and ρ is its density. The factor C characterizes the amount of the isostatic compensation depending on the wavelength and effective elastic thickness of the lithosphere (e.g. Turcotte and Schubert, 1982):

$$C = \Delta\rho g/(k^4 D + \Delta\rho g) \,, \tag{6.3}$$

where $D = ET_{\mathrm{e}}^3/[12(1-\nu^2)]$ is the flexural rigidity of the lithosphere, T_e is the effective elastic thickness of the lithosphere, E is the Young modulus, ν is the Poisson ratio, $\Delta\rho$ is the average difference of the density of topography and the upper mantle material, and g is the gravitational acceleration.

The Eq. 6.2 cannot be used directly for calculation of the isostatic correction in the spectral domain in case of variable T_e. Therefore, a convolution of the adjusted topography with specific Green's functions depending on M and T_e is employed as suggested by Braitenberg et al. (2002), Wienecke and Braitenberg (2007) and Dill et al. (2015) for modeling of the lithosphere deformations under external load. It has been demonstrated in the above papers that this method is sufficiently accurate to describe a response of the elastic lithosphere to the external load. The isostatic correction and isostatic anomalies (Δg_i) are calculated as follows:

$$\begin{gathered}\Delta g_i(x_0, y_0) = \Delta g_b(x_0, y_0) + \int\int_{-1250\,\mathrm{km}}^{1250\,\mathrm{km}} t_{adj}(x_0 + x, y_0 + y) \cdot G_{is}(x, y) dx dy \\ G_{is}(x, y) = F^{-1}(G_{is}(k_x, k_y))\end{gathered} \tag{6.4}$$

where F^{-1} is the inverse Fourier transform, G_{is} is the Green's function, which depends on M and T_e, $\Delta g_b(x, y)$ are the Bouguer gravity anomalies.

These anomalies still reflect the effect of the glacial isostatic adjustment and of the dynamic topography associated with the mantle convection. It has been demonstrated that this effect is dominated at the long-wavelengths chiefly exceeding 3000 km (Kaban et al., 1999, 2004). At the same time, the effect of the upper crust density variations in the isostatic anomalies anomalies is limited to the wavelengths 1000-1500 km, which are determined by the maximum value of T_e (~ 70 km, e.g. Audet and Bürgmann, 2011; Tesauro et al., 2012). Therefore, to reduce the effect of mantle dynamics and GIA, we have applied a Gauss type filter on the sphere with the boundary wavelength (0.5 amplitude) equal to 2500 km (Kaban et al., 1999). To avoid the "edge" effects, the isostatic anomalies for Antarctica have been embedded in the global model of Kaban et al. (2004).

The isostatic anomalies of the gravity field (Fig. 6.3a) are dominated by small-scale structures. Along the Transantarctic Mountains, a dipole-like structure is visible with positive values along the western flank and negative values towards the east. The most notable negative features are located in northern Dronning Maud Land with up to -90 mGal. A ring of positive gravity anomalies is located around the coast of EANT and is likely related to the transition from continental to oceanic lithosphere that is not sufficiently resolved in the crustal input model.

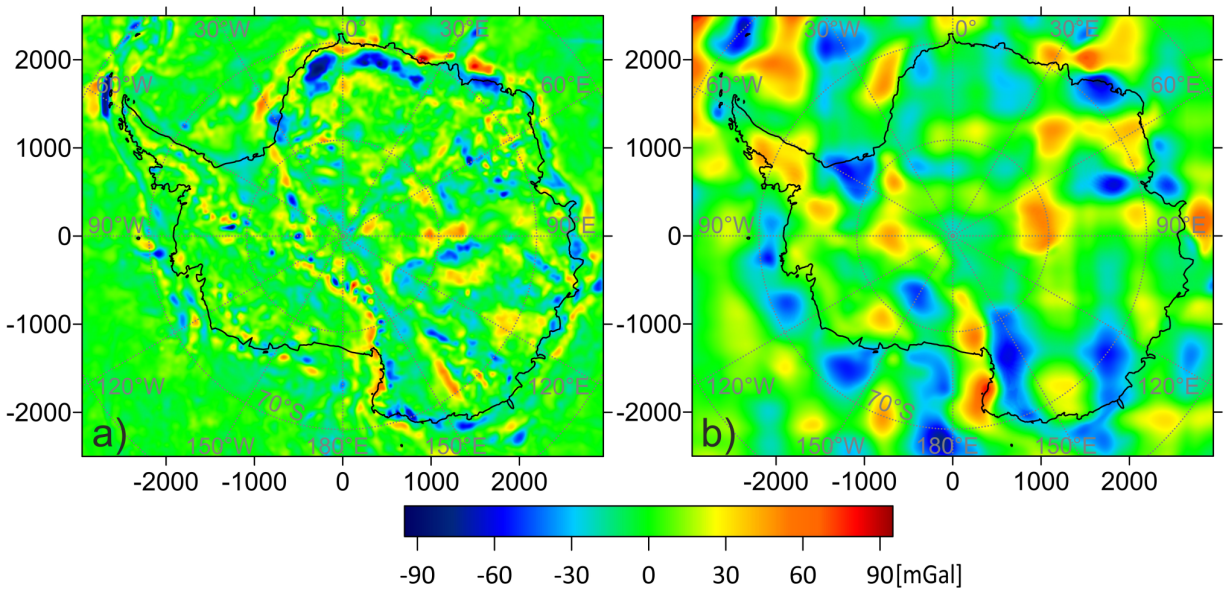

Figure 6.3.: **(a)** Isostatic anomalies of the gravity field and **(b)** decompensative gravity corrections

6.3.2. Decompensative anomalies of the gravity field

Following Kaban et al. (2017), the decompensative correction (Δg_{dc}) can be formulated in the spectral domain as the following:

$$\Delta g_{\mathrm{dc}}(k_{\mathrm{x}}, k_{\mathrm{y}}) = \frac{1}{\exp(k \cdot M)/C - 1} \cdot \Delta g_{\mathrm{i}}(k_{\mathrm{x}}, k_{\mathrm{y}})\,, \tag{6.5}$$

where Δg_{i} stands for the isostatic anomalies and other terms remain as in Eq. 6.2. This equation is based on formulations of Zorin et al. (1985) and Cordell et al. (1991), which are extended for the case of elastic support (Kaban et al., 2017). It is clear from this equation that the decompensative correction exponentially increases with increasing wavelength and approaches infinity. It has been suggested to apply a high-pass filter to reduce the correction above some boundary wavelength (λ_0) (Cordell et al., 1991). The long-wavelength component is already excluded from the isostatic anomalies in Fig. 6.3a, however, the decompensative correction can still be overestimated as demonstrated in Kaban et al. (2017). Following their argumentation, a high-pass filter starting from the wavelength 1500 km with a gradual decrease towards longer wavelengths has been applied to Eq. 6.5.

The decompensative correction is calculated using the same Green's functions technique as for the isostatic anomalies (Eqs. 6.4) and is displayed in Fig. 6.3b and exhibits larger scale features compared to the isostatic anomalies. The most notable negative decompensative

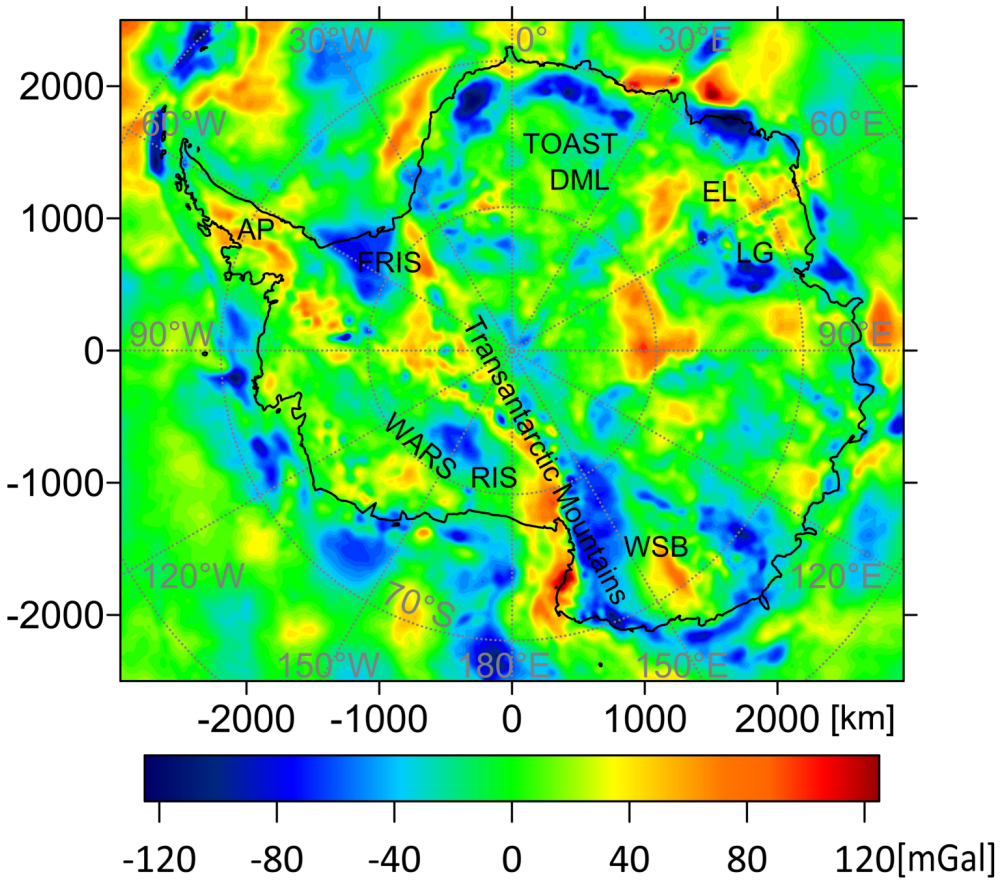

Figure 6.4.: Decompensative gravity anomalies

corrections are located in Enderby Land (-75 mGal), in the Lambert Graben (-64 mGal), the Filchner-Ronne Ice Shelf (-60 mGal), and the West Antarctic Rift System (-50 mGal). A similar dipole structure as in the isostatic anomalies is visible along the Transantarctic Mountains and in the Wilkes Subglacial Basin with positive values of up to 80 mGal in the west and negative values of up to -62 mGal in the east. Positive corrections are also located in the Antarctic Peninsular and around the Lambert Graben minimum (up to 47 and 52 mGal, respectively). The final decompensative gravity anomalies are calculated through

$$\Delta g_{\mathrm{d}} = \Delta g_{\mathrm{i}} + \Delta g_{\mathrm{dc}} \tag{6.6}$$

and are shown in Fig. 6.4. The main negative anomalies can be found in northern Dronning Maud Land (-120 mGal), in Enderby Land (-143 mGal), in the Lambert Graben (-110 mGal), the Filchner-Ronne Ice Shelf (-80 mGal) and the West Antarctic Rift System (-73 mGal). Another negative anomaly (-110 mGal), interrupted by a narrow, elongated,

positive anomaly in the Northern Basin (80 mGal), exists around the Wilkes Subglacial Basin and forms a dipole-like structure along the Transantarctic Mountains with the western flank exhibiting positive decompensative anomalies (138 mGal). This positive feature continues along the Transantarctic Mountains towards the Antarctic Peninsula. The Lambert Graben exhibits strong negative anomalies of up to -110 mGal while the surrounding region is characterized by positive values of up to 104 mGal.

6.4. Discussion

The decompensative gravity anomalies can help us understand the structure of the uppermost crust of Antarctica where direct measurements are still rare. An important if not the most important factor causing negative anomalies is the presence of sediments. Since knowledge about their distribution over Antarctica is still limited, no correction involving sediment has been applied in the initial processing. We calculate the thickness of sediments by assuming that negative decompensative anomalies are purely caused by sediments. This assumption is not valid all over the study area, therefore our results might be overestimated in some places. As well, some basins may be characterized by high density; in this case, the actual thickness could be higher than predicted. As density within sedimentary basins increases with depth in different ways for different basins and tectonic background, it would be ideal, if density-depth relations for each individual basin were used. However, these data don't exist for Antarctica and therefore standard density-depth curves for continental and oceanic basins (Mooney and Kaban, 2010) are used in the calculations. The resulting uncertainties in sediment thickness estimates depend strongly on the thickness of the sedimentary basin. Assuming that the uncertainties associated with average density variations within a basin reach up to $\pm 0.05\,\mathrm{g/cm^3}$ and a decompensative gravity anomaly of -40 mGal, the density uncertainties translate into thickness uncertainties of up to ± 1 km. It should also be noted, that not every sedimentary basins may be detectible using this approach. As mentioned above, old cratonic sediment basins can be characterized by very dense sediments that are almost indistinguishable from the crystalline crust using gravity data, which has been shown for e.g. the Illinois and the Michigan Basin (Mooney and Kaban, 2010). Additional compaction might be caused by the ice load over the majority of the Antarctic continent. Potential influence of this effect on the estimated thickness has been investigated by shifting the original density-depth curves. Where the ice is grounded, the ice thickness was converted into equivalent sediment thickness with respect to the average density of the first 1.5 km of sediments ($\rho_{\mathrm{eq}} = 2.34\,\mathrm{g/cm^3}$) and the density-depth curves were shifted

accordingly. The density-depth curves for the oceanic domain and for the continental one with the compacting effect of the ice load for 0, 1.5, 3 and 4.5 km are plotted in Fig. 6.5. The decompensative anomalies (Fig. 6.4) don't contain the long-wavelength component and

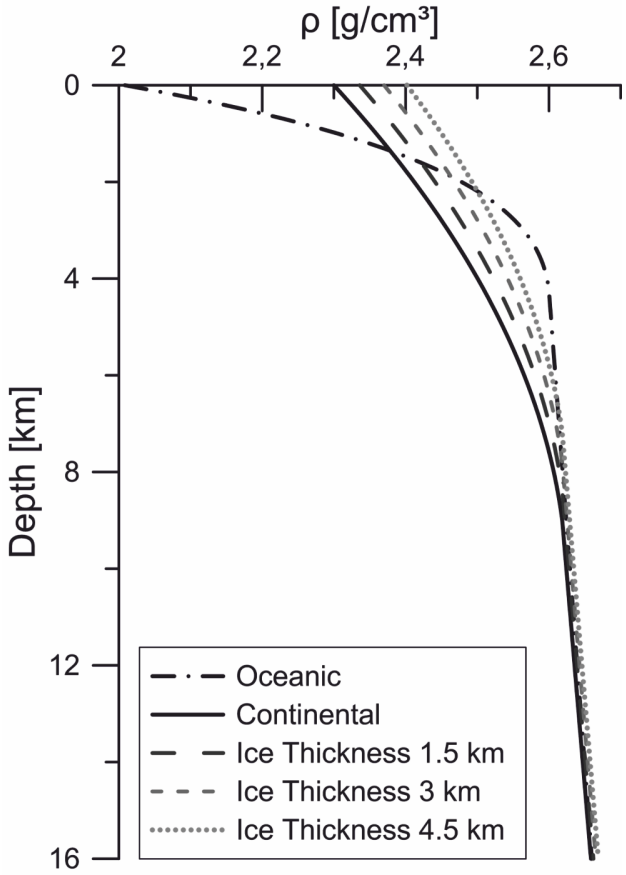

Figure 6.5.: Variation of sediment density with depth for oceanic and continental settings (Mooney and Kaban, 2010) with the compacting effect of grounded ice loads of 0, 1.5, 3 and 4.5 km thickness

their average is equal to zero. However, the actual effect of the upper crust relative to a standard reference density of 2.7 g/cm^3 should be negative (e.g. Mooney and Kaban, 2010; Kaban et al., 2014). Density variations in the crystalline crust relative to this value are close to zero on the average (Christensen and Mooney, 1995), while density of sediments is generally lower. Therefore, for estimation of the sediment thickness we should shift downward the field in Fig. 6.4 by some constant level. It is hardly possible to determine it from the existing data, however, estimates for other continents demonstrate that the average gravity effect of the upper crust is quite stable. It is equal to -17.5 mGal for North America (Kaban et al., 2014) and -14.6 mGal for Australia (Tesauro et al., 2018), for which continents very

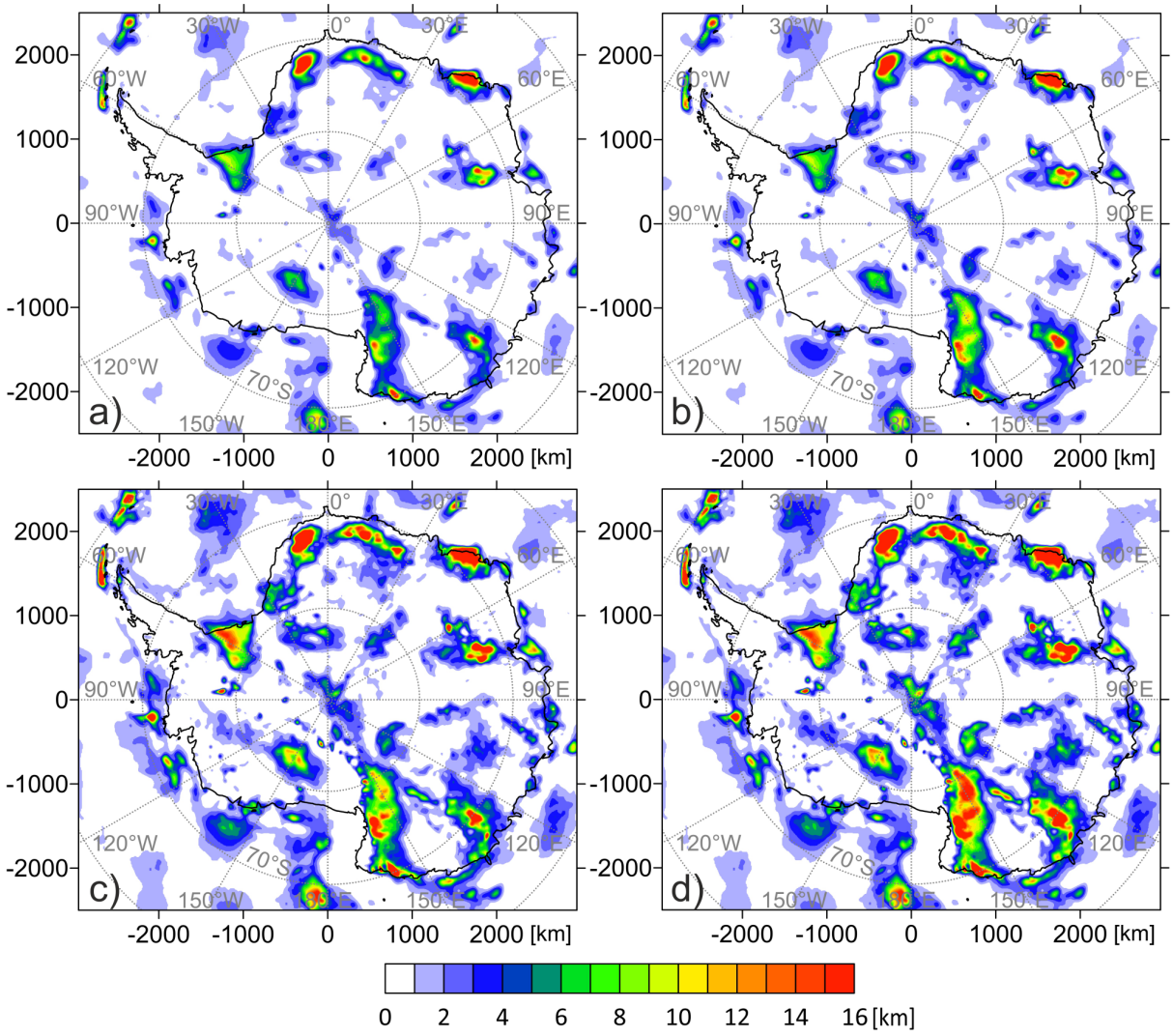

Figure 6.6.: Sediment thickness calculated from the decompensative gravity anomalies (top row). A correction of the upper crust for the decompensative gravity anomalies of -14.6 mGal is considered in the bottom row. Left column: sediment thickness calculations without ice load. Right column: sediment thickness considering compaction caused by ice loads.

detailed models of the sedimentary cover are available. For Antarctica we use the lowest value assuming that sedimentation is partially restricted due to glaciation and sediments might be more compressed under the additional ice load. This value is anyway arbitrary and possible uncertainty might reach $\pm 3-4$ mGal translating into uncertainties in sediment thickness of up to ± 0.9 km for sediment basins of 5 km depth. For the deeper sedimentary basins this uncertainty increases, but the effect of the density uncertainty is much larger anyway. This is taken into account in the interpretation of the results.

The resulting sediment thickness estimated straight from the decompensative gravity anomaly and considering the -14.6 mGal shift, both with and without considering compaction caused by the ice shield are shown in Fig. 6.6. The maximum sediment thickness is limited to 16 km, because the density of deeper sediments would be indistinguishable from crystalline rocks. Adding the corrections for the ice load and for the reduced gravity effect of the upper crust in the presence of sediments only changes the amplitude, not the distribution of sediment deposits, with both effects increasing the thickness. Despite the uncertainty in the upper crustal correction, we will discuss the sediment thicknesses obtained including both corrections from this point forward. Therefore, and because calculations of the actual thickness strongly depend on the chosen density-depth relationship which is still unknown for Antarctic sediment basins, we emphasize that all discussions of the results should be done qualitatively instead of quantitatively.
The most notable feature is the dipole like structure around the Transantarctic Mountains. The western flank is characterized by high decompensative anomalies while the eastern region as well as the western margin of the adjacent Wilkes Subglacial Basin exhibit very low values. This could be caused by local isostatic disturbances originated from extension forces of prior rifting in the West Antarctic Rift System or from dynamic uplift of the Transantarctic Mountains of possibly thermal origin as suggested by several previous studies (e.g. Behrendt, 1999; Smith and Drewry, 1984; ten Brink and Stern, 1992). Lawrence et al. (2006) state that uplift of the Transantarctic Mountains can be explained by conductive heating between cold EANT and warm WANT alone along the entire mountain chain also explaining the positive decompensative anomaly values along the continuation of the Transantarctic Mountains. They also state, that this uplift was asymmetrical causing erosion of younger sediments on the coastward side, exposing denser basement rock and older sediments. This together with the large sediment dispositions in the southern Wilkes Subglacial Basin suggested by Frederick et al. (2016) can also cause the negative decompensative anomalies we observe. However, even though we confirm the presence of large sediment deposits, attributing these negative variations purely to sediments as done in our calculations leading to thicknesses of up to 16 km likely represents an overestimation of the sediment thickness. This value can be reduced if the sediments have lower density than suggested. The western Wilkes Subglacial Basin exhibits low sedimentation (Frederick et al., 2016) and high decompensative anomaly values which is likely related to denser basement rocks. Adjacent, further sediment infill is detected. The border of this feature coincides with the Adventure Trench that has been shown to have $\sim$ 10 km sediment infill (Ferraccioli et al., 2001), but is not limited to the trench.

Negative decompensative gravity anomalies suggesting the presence of significant sediment accumulations are also found in the West Antarctic Rift System with a maximum infill at the transition to the Ross Ice Shelf and a continuation in the western Ross Sea. Sediment infill of the Rift System has been documented by several studies in the past (e.g. Baranov et al., 2018; Laske and Masters, 2013), supporting our interpretation. Anandakrishnan et al. (1998) estimated a sediment layer of 2.8 km under an ice stream (roughly 82°S, 121°E) agreeing well with our estimates of $\sim$ 2.5 km. While the above mentioned studies mapped a relatively constant sediment infill of 2-3 km along most of the West Antarctic Rift System, the newly found thick sediment cover at the ice shelf transition offers new insight into variation in sediment thickness along the Rift System. Wobbe et al. (2014) found evidence of a thick sediment layer of up to 8 km under most of the Ross Ice Shelf. This sediment layer continues in the Ross Sea with major infill in the Victoria Land Basin, the Central Trough and the Eastern Basin (Behrendt et al., 1991; Trey et al., 1999). We only map sediment infill in the western Ross Ice Shelf and in the Eastern Basin, with the positive decompensative anomaly attributed to Transantarctic Mountain uplift described above masking potential sediments in the eastern ice shelf region and in the other two sediment basins in the Ross Sea. Trey et al. (1999) also predict high density upper crust below the sediment basins, further equalizing the gravity effect of low density sediments. Lindeque et al. (2016) further determined sediment thicknesses along a seismic profile in the Amundsen Sea Basin and found maximum thicknesses of almost 4 km around 145°W, corresponding well with the location of a maximum in sediment infill in our determinations.

The other large Antarctic ice shelf, the Filchner-Ronne Ice Shelf is also characterized by low decompensative gravity anomalies that translate into sediment thicknesses of over 15 km. Two seismic profiles crossing the Filchner-Ronne Ice shelf were conducted in the past (Hübscher et al., 1996; Leitchenkov and Kudryavtzev, 1997), independently determining sediment layers of up to 13 and 15 km, respectively, agreeing well with our determinations. High sediment infill is expected in the Lambert Graben when converting the low compensative gravity anomalies to sediment deposits, which is confirmed by previous studies (Harrowfield et al., 2005; Holdgate et al., 2005). However, thickness determinations only exist offshore in the Prydz Bay (Stagg et al., 2004). Their sediment thickness determinations of 5-8 km lie well below our estimates of up to 13 km, suggesting an overestimation in both the Prydz Bay and the Lambert Graben. A ring of high decompensative gravity anomalies surrounds the Lambert Graben, possibly caused by older, denser upper crustal rocks. Furthermore, Chen et al. (2018) predict notable lithospheric weakening in the graben structure compared to higher effective elastic thickness estimates in the surroundings. This

transition from local to regional compensation might cause disturbances of the isostatic equilibrium insufficiently corrected for in the initial calculations, reflecting in the above described anomaly structures.
Dronning Maud Land is chiefly governed by negative decompensative gravity anomalies that can be explained by sediment deposits. The largest sediment accumulations are predicted in coastal Dronning Maud Land in the vicinity of the Grunehogna craton and the Tonian Oceanic Arc Super Terrane and in northern Enderby Land. The coverage of studies analyzing sediments in this region is still sparse, making direct comparison difficult. Curtis and Riley (2003) and Krynauw et al. (1994) found evidence of sediment deposits when investigating the Grunehogna nunataks, however no geophysical estimate of sediment thickness or density has been conducted. Gupta et al. (2017) studied the subsurface below Maitri station (70.76°S, 11.73°E) at the northern edge of the decompensative anomaly minimum estimating a sediment layer of 1.5 km. This supports our interpretation of the feature as a sediment basin of possibly marine origin, as the Tonian Oceanic Arc Super Terrane is proposed to be a remnant of the Mozambique Ocean (Jacobs et al., 2015). Further south, we find thinner sediment deposits underlying parts of the Recovery Glacier and the Bailey Ice Stream. In the vicinity, Bamber et al. (2006) detected sediment deposits of $\sim$ 3 km underlying the Slessor Tributary North using aeromagnetic measurements.

6.5. Conclusions

Here, we present a continent wide study of the decompensative gravity anomaly over Antarctica revealing upper crustal structures. Isostatic gravity anomalies are widely used for this purpose; they are however still reduced by deep compensating masses. The decompensative correction over Antarctica reaches values of up to $\pm$70 mGal. Hence, neglecting this effect might lead to misinterpretation of upper crustal structures. Large positive decompensative gravity anomalies are located around a minimum in the Lambert Graben, which are probably caused by higher density, old crystalline crust combined with isostatic disturbances induced by the transition from regional to local compensation as suggested by analyzing effective elastic thickness variations in this region (Chen et al., 2018).
Negative anomalies are translated into sediment thickness, which is still largely unknown for Antarctica due to the thick ice shield covering the majority of the continent, taking into account the compacting effect of these ice loads on sediment density. The resulting sediment thicknesses are subject to large uncertainties caused by unknown density-depth relationships for the individual basins and the unknown reducing gravity effect of the upper crust.

Therefore, they should be understood as qualitative instead of quantitative estimates.
We confirm the presence of major sediment basins in the Filchner-Ronne Ice Shelf, the northern Wilkes Subglacial Basin and the Lambert Graben. Further sedimentary deposits that were previously not or only partially mapped are detected in both EANT and WANT. Thus, we find maximum sediment infill of the West Antarctic Rift System at the transition from the continent to the Ross Ice Shelf and thick sediment basins along the coast of Dronning Maud Land and Enderby Land. Additionally, sediments are found underlying major ice streams of the East Antarctic Ice Shield like the Recovery Glacier, which might have played an important role in ice stream formation and dynamics. Known sedimentary deposits such as in the Ross Sea are not mapped in this study but were masked by positive decompensative gravity anomalies caused by local isostatic disturbances due to the dynamic (possibly thermally driven, Lawrence et al., 2006), uplift of the Transantarctic Mountains.

7 Conclusion and Outlook

The main focus of this thesis is to characterize the structures and properties of the Antarctic lithosphere in terms of strength, temperature, density and composition based on the integration of various geophysical data. High resolution gravity disturbances combined from satellite and ground-based observations are the main data source throughout the three consecutive studies this thesis consists of. In the first study, spectral parameters, namely the coherence and admittance of the gravity field and the topography corrected for the differences in density of ice, water and bedrock loads are calculated to determine, for the first time, a map of effective elastic thickness variations of the entire Antarctic continent. In the second study, temperature, density and composition variations of the Antarctic upper mantle are estimated. In order to retrieve corrections of the crustal gravity field, the Moho depth is recovered from seismic reflection, refraction and receiver functions combined with surface wave tomography and a first order model of crustal densities is determined. Iteratively combining seismic tomography converted into temperature variation using mineral physics equations with a joint inversion of residual gravity and residual topography data allows to not only estimate total density variations but also to distinguish between thermal and composition induced density. Composition in terms of iron content of the minerals is also obtained and used to correct the temperature estimates for the next iteration. During the first two studies, corrections of the gravity field for upper crustal structures such as sedimentary loads could not be conducted properly due to the sparseness of direct measurements of sediment thickness and density, causing uncertainties in the calculations. Hence, the third study employs decompensative gravity anomalies to decipher upper crustal structures, notably the distribution of low density sediments relying on the results of the previous studies. Since large uncertainties due to, for example, unknown density depth relations for the specific sediment basins are present in the estimates, the results provide a qualitative rather than quantitative distribution of sediment accumulations.

The distinction between West and East Antarctica has been well documented in the past (compare section 1.2). All lithospheric parameters studied here support this assumption. In EANT, the lithosphere is found to be cold, thick and of high density, resulting in gen-

erally high values of T_e. High depletion also affirms the Precambrian age compared to the notably younger WANT that only reached its current position and shape in the Cenozoic. The lithosphere of WANT is characterized by low T_e, indicating high temperatures and a thin lithosphere, which is corroborated by the calculated Moho thicknesses and direct temperature estimates. Low variations in compositional density ($< \pm 0.015\,g/cm^3$) indicate, that the negative residual gravity variations present here are chiefly induced by a hot upper mantle. The Transantarctic Mountains mark the border and transition between EANT and WANT. It is still not clear whether they should be attributed to EANT or WANT. Since they are characterized by low T_e along the entire mountain chain and by high temperatures and thermal as well as total density, a connection to WANT seems likely. The dipole in the decompensative gravity anomalies along the TAM could be caused by isostatic disturbances related to dynamic uplift of the TAM and extension forces of prior rifting in the West Antarcitc Rift System. Significant sediment infill was detected in the WARS, confirming previous studies (e.g. Baranov et al., 2018; Laske and Masters, 2013) but providing more detail on the distribution within the rift system, with a local maximum at the transition to the Ross Ice Shelf. Sedimentation continues into the Ross see, but is partially masked by the TAM anomaly. Large sediment deposits are also detected in the other big Antarctic ice shelf, the Filchner-Ronne Ice Shelf.

Apart from the general distinction between west and east, additional lithospheric structures within EANT have been discovered. Along the Lambert Graben that might be part of a bigger East Antarctic rift system (Ferraccioli et al., 2011) severe lithospheric weakening has been detected with a drop of T_e of over 50 km compared to the surrounding area. This agrees well with the composition analysis. The almost undepleted lithosphere is likely caused by rejuvenation during the rifting process that might have been as recent as the Cretaceous (Lisker et al., 2003). Low decompensative gravity anomalies associated with high sediment infill are found in the rift, while the surroundings exhibit very high decompensative anomalies. Likely causes are the presence of old and dense crystalline crust combined with isostatic disturbances induced by the abrupt change in lithospheric strength. Low T_e is further predicted around the Gamburtsev Subglacial Mountains, agreeing well with the high temperatures estimates in this area, which could potentially be caused by a mantle plume (Sleep, 2006). This correlation between the results of the different studies support the preference given to the T_e determinations obtained using the coherence method. The estimates based on the admittance locate this low T_e structure in Enderby Land instead, finding higher T_e in the graben.

Dronning Maud Land is characterized by high T_e, correlating with low temperature, high

depletion and negative compositional density that can be interpreted as an Archean to Paleoproterozoic craton. In the vicinity of this cratonic structure, recent studies (Jacobs et al., 2015, 2017; Ruppel et al., 2018) found evidence of juvenile early Mesoproterozoic to Neoproterozoic terrains that are proposed to be remnants of the Mozambique Ocean called Tonian Oceanic Arc Super Terrane. In this area, depletion is reduced, supporting the assumed younger age. T_e is reduced as well. Further, sediment deposition, that could hence be of oceanic origin when following the previously mentioned authors argumentation, has been detected. Similar cratonic structures are detected close to the South Pole and in Wilkes Land. The Archean to Paleoproterozoic Mawson craton is located in Wilkes Land (e.g. Boger, 2011), with a proposed continuation into EANT with a distinct fragment around the Nimrod Group, coinciding with the anomalies. Furthermore, sediment deposits are found underlying major east Antarctic ice streams (e.g. the Recovery Glacier), which might have had a significant influence on the onset and speed of ice streaming.

The highest values of T_e within Antarctica are consistently located between around 90°E and 130°E based on both coherence and admittance analysis. At the same time, a local maximum of composition induced density exists that was translated into almost primitive mantle composition that gets more distinct with increasing depth (>150 km). This minimum in depletion coincides with the Indo-Australo-Antarctic Suture and was interpreted as rejuvenation caused by Paleo- to Mesozoic reactivation linked to rifting in the East Antarctic Rift System (e.g. Aitken et al., 2014). This would indicate structural weakening opposing high T_e. However, T_e is most sensitive to the upper part of the lithosphere (until 100-125 km), while rejuvenation of the mantle dominates at greater depths. A shifted depleted cratonic root as observed for North America (Kaban et al., 2015) could potentially explain such observations. Additionally, the Precambrian suture event could have caused eclogitisation, increasing the density without increasing the Mg # which might have led to an underestimation of depletion. Still, further research is required to provide a solid explanation.

This thesis presents a comprehensive model of the structure and properties of the lithosphere of Antarctica. Lithospheric strength as well as a 3D model of temperature, density and composition variations was obtained for the entire continent. In addition, upper crustal structures such as sediment distributions were determined. However, the system Earth does not consists of static independent layers, but represents a complex system of interacting dynamic sub-systems. Solid understanding of each of these layers is required to understand the dynamic processes linking them to each other. Therefore, the lithospheric model provided in this thesis represents an indispensable foundation for analyzing the link of the lithosphere

with near-surface processes. Particularly the density and viscosity variation in the lithosphere strongly influences visco-elastic processes such as glacial isostatic adjustment. GIA is closely interconnected with changes in ice dynamics, which is, in turn, influenced by the thermal state of the lithosphere and the nature of the upper crust. Recent studies (e.g. Kaban et al., 2015) have further shown interconnection between the lithosphere and the convecting mantle.

Traditionally, models of mantle convection are conducted without taking into account the lithosphere as more than a thin-sheet approximation. At the same time, lithospheric modeling usually does not consider mantle currents. However, mantle convection plays a key role in plate tectonics and interacts with the base of the lithosphere, with basal drag and dynamic topography caused by mantle flow altering the stress field distribution. Against conventional belief, even cratonic structures were shown to be affected (Kaban et al., 2015). Therefore, a dynamic model of the lithosphere-upper mantle system should be constructed, providing mantle flow velocities, heat transfer in the upper mantle and stresses at the base of the lithosphere using the code ProSpher3D (Petrunin et al., 2013a). As input parameters, this code requires the density distribution of the lithosphere and the upper mantle, 3D viscosity variations and a rheological model of the lithosphere. The first and the last parameter can be directly obtained from the results of this thesis. 3D viscosity variations can be calculated based on the presented thermal model with mineral physics constraints (Paulson et al., 2005).

Geothermal heat flux strongly influences ice temperature, viscosity and water content, which in turn determines the deformation response of the ice under stresses applied by the overlying ice column. Hence, higher ice temperatures cause higher ice flow speeds. Geothermal heat flux combined with basal friction heating additionally affects the thermal state at the base of the ice sheet. If the pressure melting point is reached, basal melting water further lubricates the ice base and higher sliding velocities are reached (e.g. Goeller et al., 2013). If the ice freezes to the underlying substrate, no sliding occurs and ice flow is purely caused by internal deformation. Therefore, high quality maps of geothermal heat flux are crucial when monitoring ice dynamics, the shape and the mass balance of the Antarctic Ice Sheet. Since direct measurements are sparse because of the large ice thicknesses, other solid earth models are necessary to estimate the heat flux. The thermal model of the lithosphere constructed in this thesis combined with the heat transfer calculated using ProSpher3D and constrained with magnetic determinations of the Curie depth will provide the basis for geothermal heat flux determination.

Since the dynamic behavior of the ice shield depends on both the geothermal heat flux

and climate forcing, a coupled model connecting the solid earth with the ice shield and the atmosphere is necessary to describe ice dynamics. Such a model has been developed for Greenland (Petrunin et al., 2013b; Rogozhina et al., 2016), providing heat flow at the base of the ice sheet, temperature distribution within the ice and ice flow velocities. Verification with measured ice flow velocities validate the accuracy of the results. This method can be applied to Antarctica based on the solid Earth parameters presented in this thesis to improve knowledge on the ice dynamics in Antarctica. Therefore, the findings of this thesis are not only important to fully characterize the structure and state of the lithosphere in Antarctica, but also provide the basis for further research in various aspects of this enigmatic continent.

List of Figures

Bibliography

Aitken, A., Betts, P., Young, D., Blankenship, D., Roberts, J., and Siegert, M., 2016: The Australo-Antarctic Columbia to Gondwana transition, Gondwana Research, 29, 136–152, doi:10.1016/J.GR.2014.10.019.

Aitken, A. R. A., Young, D. A., Ferraccioli, F., Betts, P. G., Greenbaum, J. S., Richter, T. G., Roberts, J. L., Blankenship, D. D., and Siegert, M. J., 2014: The subglacial geology of Wilkes Land, East Antarctica, Geophysical Research Letters, 41, 2390–2400, doi:10.1002/2014GL059405.

An, M., Wiens, D. A., Zhao, Y., Feng, M., Nyblade, A., Kanao, M., Li, Y., Maggi, A., and Lévêque, J.-J., 2015a: Temperature, lithosphere-asthenosphere boundary, and heat flux beneath the Antarctic Plate inferred from seismic velocities, Journal of Geophysical Research: Solid Earth, 120, 8720–8742, doi:10.1002/2015JB011917.

An, M., Wiens, D. A., Zhao, Y., Feng, M., Nyblade, A. A., Kanao, M., Li, Y., Maggi, A., and Lévêque, J. J., 2015b: S-velocity model and inferred Moho topography beneath the Antarctic Plate from Rayleigh waves, Journal of Geophysical Research B: Solid Earth, 120, 359–383, doi:10.1002/2014JB011332.

Anandakrishnan, S., Blankenship, D. D., Alley, R. B., and Stoffa, P. L., 1998: Influence of subglacial geology on the position of a West antarctic ice stream from seismic observations, Nature, 394, 62–65, doi:10.1038/27889.

Audet, P. and Bürgmann, R., 2011: Dominant role of tectonic inheritance in supercontinent cycles, Nature Geoscience, 4, 184–187, doi:10.1038/ngeo1080.

Audet, P. and Mareschal, J. C., 2007: Wavelet analysis of the coherence between Bouguer gravity and topography: Application to the elastic thickness anisotropy in the Canadian Shield, Geophysical Journal International, 168, 287–298, doi:10.1111/j.1365-246X.2006.03231.x.

Bamber, J. L., Ferraccioli, F., Joughin, I., Shepherd, T., Rippin, D. M., Siegert, M. J., and Vaughan, D. G., 2006: East Antartic ice stream tributary underlain by major sedimentary basin, Geology, 34, 33–36, doi:10.1130/G22160.1.

Banks, R. J., Parker, R. L., and Huestis, S. P., 1977: Isostatic compensation on a regional scale: Local vs. regional mechanisms, Geophysical Journal Royal Astronomical Society, 51, 431–452.

Baranov, A. and Morelli, A., 2013: The Moho depth map of the Antarctica region, Tectonophysics, 609, 299–313, doi:10.1016/j.tecto.2012.12.023.

Baranov, A., Tenzer, R., and Bagherbandi, M., 2018: Combined Gravimetric–Seismic Crustal Model for Antarctica, Surveys in Geophysics, 39, 23–56, doi:10.1007/s10712-017-9423-5.

Barthelmes, F., 2013: Definition of Functionals of the Geopotential and Their Calculation from Spherical Harmonic Models, Scientific Technical Report STR09/02, Revised Edition, Tech. Rep. January, doi:10.2312/GFZ.b103-0902-26.

Bayer, B., Geissler, W. H., Eckstaller, A., and Jokat, W., 2009: Seismic imaging of the crust beneath Dronning Maud Land, East Antarctica, Geophysical Journal International, 178, 860–876, doi:10.1111/j.1365-246X.2009.04196.x.

Behrendt, J. C., 1999: Crustal and lithospheric structure of the west Antarctic Rift System from geophysical investigations - A review, Global and Planetary Change, 23, 25–44, doi:10.1016/S0921-8181(99)00049-1.

Behrendt, J. C., LeMasurier, W. E., Cooper, A. K., Tessensohn, F., Tréhu, A., and Damaske, D., 1991: Geophysical studies of the West Antarctic Rift System, Tectonics, 10, 1257–1273, doi:10.1029/91TC00868.

Bell, R. E., Blankenship, D. D., Finn, C. A., Morse, D. L., Scambos, T. A., Brozena, J. M., and Hodge, S. M., 1998: Influence of subglacial geology on the onset of a West Antarctic ice stream from aerogeophysical observations, Nature, 394, 58–62.

Blakely, R. J.: 1995, Potential theory in gravity and magnetic applications, Cambridge university press.

Block, A. E., Bell, R. E., and Studinger, M., 2009: Antarctic crustal thickness from satellite gravity: Implications for the Transantarctic and Gamburtsev Subglacial Mountains, Earth and Planetary Science Letters, 288, 194–203, doi:10.1016/j.epsl.2009.09.022.

Boger, S. D., 2011: Antarctica - Before and after Gondwana, Gondwana Research, 19, 335–371, doi:10.1016/j.gr.2010.09.003.

Braitenberg, C., Ebbing, J., and Götze, H. J., 2002: Inverse modelling of elastic thickness by convolution method - The eastern Alps as a case example, Earth and Planetary Science Letters, 202, 387–404, doi:10.1016/S0012-821X(02)00793-8.

Burov, E. B. and Diament, M., 1995: The effective elastic thickness (Te) of continental lithosphere: What does it really mean?, Journal of Geophysical Research: Solid Earth, 100, 3905–3927, doi:10.1029/94JB02770.

Burton-Johnson, A., Halpin, J. A., Whittaker, J. M., Graham, F. S., and Watson, S. J., 2017: A new heat flux model for the Antarctic Peninsula incorporating spatially variable upper crustal radiogenic heat production, Geophysical Research Letters, 44, 5436–5446, doi:10.1002/2017GL073596.

Cammarano, F., Goes, S., Vacher, P., and Giardini, D., 2003: Inferring upper-mantle temperatures from seismic velocities, Physics of the Earth and Planetary Interiors, 138, 197–222, doi:10.1016/S0031-9201(03)00156-0.

Chen, B., Kaban, M. K., El Khrepy, S., and Al-Arifi, N., 2015a: Effective elastic thickness of the Arabian plate: Weak shield versus strong platform, Geophysical Research Letters, 42, 3298–3304, doi:10.1002/2015GL063725.

Chen, B., Liu, J., Chen, C., Du, J., and Sun, Y., 2015b: Elastic thickness of the Himalayan-Tibetan orogen estimated from the fan wavelet coherence method, and its implications for lithospheric structure, Earth and Planetary Science Letters, 409, 1–14, doi:10.1016/j.epsl.2014.10.039.

Chen, B., Haeger, C., Kaban, M., and Petrunin, A., 2018: Variations of the effective elastic thickness reveal tectonic fragmentation of the Antarctic lithosphere, Tectonophysics, 746, doi:10.1016/j.tecto.2017.06.012.

Christensen, N. I. and Mooney, W. D., 1995: Seismic velocity structure and composition of the continental crust: A global view, Journal of Geophysical Research: Solid Earth, 100, 9761–9788, doi:10.1029/95JB00259.

Cianfarra, P. and Maggi, M., 2017: Cenozoic extension along the reactivated Aurora Fault System in the East Antarctic Craton, Tectonophysics, 703-704, 135–143, doi:10.1016/j.tecto.2017.02.019.

Clarkson, P., 1983: The reconstruction of Lesser Antarctica within Gondwana, in: Antarctic earth science, edited by Oliver, R. L., James, P., and Jago, J., p. 599, Cambridge University Press.

Close, D. I., Stagg, H. M. J., and O'Brien, P. E., 2007: Seismic stratigraphy and sediment distribution on the Wilkes Land and Terre Ad??lie margins, East Antarctica, Marine Geology, 239, 33–57, doi:10.1016/j.margeo.2006.12.010.

Cordell, L., Zorin, Y. A., and Keller, G. R., 1991: The decompensative gravity anomaly and deep structure of the region of the Rio Grande Rift, Journal of Geophysical Research, 96, 6557–6568, doi:10.1029/91JB00008.

Curtis, M. L. and Riley, T. R., 2003: Mobilization of fluidized sediment during sill emplacement, western Dronning Maud Land, East Antarctica, Antarctic Science, 15, 393–398, doi:10.1017/S0954102003001408.

Dalziel, I. W. D., 1992: Antartica; a tale of two supercontinents, Statewide Agricultural Land Use Baseline 2015, 1, doi:10.1017/CBO9781107415324.004.

Dalziel, I. W. D. and Elliot, D. H., 1982: West Antarctica: Problem child of Gondwanaland, Tectonics, 1, 3–19, doi:10.1029/TC001i001p00003.

Danesi, S. and Morelli, A., 2001: Structure of the upper mantle under the Antarctic Plate from surface wave tomography, Geophysical Research Letters, 28, 4395–4398, doi:10.1029/2001GL013431.

Della Vedova, B. and Von Herzen, R. P.: 1987, Geothermal heat flux at the COST B-2 and B-3 Wells, U. S. Atlantic continental margin, Woods Hole Oceanographic Institution, Woods Hole, MA, doi:10.1575/1912/7589.

Deschamps, F., Trampert, J., and Snieder, R., 2002: Anomalies of temperature and iron in the uppermost mantle inferred from gravity data and tomographic models, Physics of the Earth and Planetary Interiors, doi:10.1016/S0031-9201(01)00294-1.

Dill, R., Klemann, V., Martinec, Z., and Tesauro, M., 2015: Applying local Green's functions to study the influence of the crustal structure on hydrological loading displacements, Journal of Geodynamics, 88, 14–22, doi:10.1016/j.jog.2015.04.005.

Dorman, L. M. and Lewis, B. T. R., 1970: Experimental isostasy: 1. Theory of the determination of the Earth's isostatic response to a concentrated load, Journal of Geophysical Research, 75, 3357, doi:10.1029/JB075i017p03357.

Ebbing, J., Braitenberg, C., and Wienecke, S., 2007: Insights into the lithospheric structure and tectonic setting of the Barents Sea region from isostatic considerations, Geophysical Journal International, 171, 1390–1403, doi:10.1111/j.1365-246X.2007.03602.x.

Ebbing, J., Pappa, F., Ferraccioli, F., van der Wal, W., and Barletta, V., 2016: Deciphering the Changes in the Lithospheric Structure of Antarctica by Combining Seismological and Satellite Gravity Gradient Data, AGU Fall Meeting Abstracts.

Ebbing, J., Haas, P., Ferraccioli, F., Pappa, F., Szwillus, W., and Bouman, J., 2018: Earth tectonics as seen by GOCE - Enhanced satellite gravity gradient imaging, Scientific Reports, 8, 1–9, doi:10.1038/s41598-018-34733-9.

Fanning, C. M., Flint, R. B., Parker, A. J., Ludwig, K. R., and Blissett, A. H., 1988: Refined Proterozoic evolution of the Gawler Craton, South Australia, through U-Pb zircon geochronology, Precambrian Research, 40-41, 363–386, doi:10.1016/0301-9268(88)90076-9.

Ferraccioli, F., Coren, F., Bozzo, E., Zanolla, C., Gandolfi, S., Tabacco, I., and Frezzotti, M., 2001: Rifted(?) crust at the East Antarctic Craton margin: Gravity and magnetic interpretation along a traverse across the Wilkes Subglacial Basin region, Earth and Planetary Science Letters, 192, 407–421, doi:10.1016/S0012-821X(01)00459-9.

Ferraccioli, F., Finn, C. a., Jordan, T., Bell, R. E., Anderson, L., and Damaske, S., 2011: East Antarctic rifting triggers uplift of the Gamburtsev Mountains, Nature, 479, 388–392, doi:10.1038/nature10566.

Ferraccioli, F., Bell, R., Blankenship, D., Young, D., Eagles, G., Forsberg, R., Armadillo, E., Aitken, A., Jacobs, J., Seddon, S., Jordan, T., Golynsky, S., Ebbing, J., Finn, C., and Dalziel, I., 2016: Revealing the crustal architecture of the least understood composite craton on Earth: East Antarctica, AGU Fall Meeting Abstracts, doi: 2016AGUFM.T11B2620F.

Finotello, M., Nyblade, A., Julia, J., Wiens, D., and Anandakrishnan, S., 2011: Crustal Vp-Vs ratios and thickness for Ross Island and the Transantarctic Mountain front, Antarctica, Geophysical Journal International, 185, 85–92, doi:10.1111/j.1365-246X.2011.04946.x.

Fisher, A. T., Mankoff, K. D., Tulaczyk, S. M., and Tyler, S. W., 2015: High geothermal heat flux measured below the West Antarctic Ice Sheet, pp. 1–9.

Flöttmann, T. and Oliver, R., 1994: Review of Precambrian-Palaeozoic relationships at the craton margins of southeastern Australia and adjacent Antarctica, Precambrian Research, 69, 293–306, doi:10.1016/0301-9268(94)90093-0.

Fogg, G. E.: 1992, A history of Antarctic science, Cambridge University Press.

Förste, C., Bruinsma, S. L., Abrikosov, O., Lemoine, J.-M., Marty, J. C., Flechtner, F., Balmino, G., Barthelmes, F., and Biancale, R., 2014: EIGEN-6C4 The latest combined global gravity field model including GOCE data up to degree and order 2190 of GFZ Potsdam and GRGS Toulouse., GFZ Data Services., doi:http://doi.org/10.5880/icgem.2015.1.

Forsyth, D. W., 1985: Subsurface loading and estimates of the flexural rigidity of continental lithosphere, Journal Of Geophysical Research: Planets, 90, 12 623–12 632, doi:10.1029/JB090iB14p12623.

Forte, A. M. and Peltier, R., 1991: Viscous flow models of global geophysical observables: 1. Forward problems, Journal of Geophysical Research: Solid Earth, 96, 20 131–20 159, doi:10.1029/91JB01709.

Frederick, B. C., Young, D. A., Blankenship, D. D., Richter, T. G., Kempf, S. D., Ferraccioli, F., and Siegert, M. J., 2016: Distribution of subglacial sediments across the Wilkes Subglacial Basin, East Antarctica, Journal of Geophysical Research F: Earth Surface, 121, 790–813, doi:10.1002/2015JF003760.

Fretwell, P., Pritchard, H. D., Vaughan, D. G., Bamber, J. L., Barrand, N. E., Bell, R., Bianchi, C., Bingham, R. G., Blankenship, D. D., Casassa, G., Catania, G., Callens, D., Conway, H., Cook, A. J., Corr, H. F. J., Damaske, D., Damm, V., Ferraccioli, F., Forsberg, R., Fujita, S., Gim, Y., Gogineni, P., Griggs, J. A., Hindmarsh, R. C. A., Holmlund, P., Holt, J. W., Jacobel, R. W., Jenkins, A., Jokat, W., Jordan, T., King, E. C., Kohler, J., Krabill, W., Riger-Kusk, M., Langley, K. A., Leitchenkov, G., Leuschen, C., Luyendyk, B. P., Matsuoka, K., Mouginot, J., Nitsche, F. O., Nogi, Y., Nost, O. A., Popov, S. V., Rignot, E., Rippin, D. M., Rivera, A., Roberts, J., Ross, N., Siegert, M. J., Smith, A. M., Steinhage, D., Studinger, M., Sun, B., Tinto, B. K., Welch, B. C., Wilson, D., Young, D. A., Xiangbin, C., and Zirizzotti, A., 2013: Bedmap2: Improved ice bed, surface and thickness datasets for Antarctica, Cryosphere, 7, 375–393, doi:10.5194/tc-7-375-2013.

Godard, G. and Palmeri, R., 2013: High-pressure metamorphism in Antarctica from the Proterozoic to the Cenozoic: A review and geodynamic implications, Gondwana Research, 23, 844–864, doi:10.1016/J.GR.2012.07.012.

Godey, S., Deschamps, F., Trampert, J., and Snieder, R., 2004: Thermal and compositional anomalies beneath the North American continent, Journal of Geophysical Research: Solid Earth, doi:10.1029/2002JB002263.

Goeller, S., Thoma, M., Grosfeld, K., and Miller, H., 2013: A balanced water layer concept for subglacial hydrology in large-scale ice sheet models, Cryosphere, 7, 1095–1106, doi: 10.5194/tc-7-1095-2013.

Goes, S., Govers, R., and Vacher, P., 2000: Shallow mantle temperatures under Europe from P and S wave tomography, Journal Of Geophysical Research-Solid Earth, 105, 11 153–11 169, doi:10.1029/1999jb900300.

Golynsky, A., Chiappini, M., Damaske, D., Ferraccioli, F., Ferris, J., Finn, C., Ghidella, M., Isihara, T., Johnson, A., Kim, H., et al., 2001: ADMAP–Magnetic Anomaly Map of the Antarctic, 1: 10 000 000 scale map, BAS (Misc.), 10, 1109–1112.

Golynsky, A. V., Ferraccioli, F., Hong, J. K., Golynsky, D. A., von Frese, R. R., Young, D. A., Blankenship, D. D., Holt, J. W., Ivanov, S. V., Kiselev, A. V., Masolov, V. N., Eagles, G., Gohl, K., Jokat, W., Damaske, D., Finn, C., Aitken, A., Bell, R. E., Armadillo, E., Jordan, T. A., Greenbaum, J. S., Bozzo, E., Caneva, G., Forsberg, R., Ghidella, M., Galindo-Zaldivar, J., Bohoyo, F., Martos, Y. M., Nogi, Y., Quartini, E., Kim, H. R., and Roberts, J. L., 2018: New Magnetic Anomaly Map of the Antarctic, Geophysical Research Letters, 45, 6437–6449, doi:10.1029/2018GL078153.

Goodge, J. W., 2018: Crustal heat production and estimate of terrestrial heat flow in central East Antarctica, with implications for thermal input to the East Antarctic ice sheet, The Cryosphere, 12, 491–504, doi:10.5194/tc-12-491-2018.

Griffin, W. L., O'Reilly, S. Y., Doyle, B. J., Pearson, N. J., Coopersmith, H., Kivi, K., Malkovets, V., and Pokhilenko, N., 2004: Lithosphere mapping beneath the North American plate, Lithos, 77, 873–922, doi:10.1016/j.lithos.2004.03.034.

Gupta, S., Kanna, N., and Akilan, A., 2017: Volcanic passive continental margin beneath Maitri station in central DML , East Antarctica : constraints from crustal shear velocity through receiver function modelling, Polar Research, 36, doi: 10.1080/17518369.2017.1332947.

Hackney, R. I. and Featherstone, W. E., 2003: Geodetic versus geophysical perspectives of the 'gravity anomaly', Geophysical Journal International, 154, 35–43, doi:10.1046/j.1365-246X.2003.01941.x.

Haeger, C., Kaban, M. K., Tesauro, M., Petrunin, A. G., and Mooney, W. D., 2019: 3D density, thermal and compositional model of the Antarctic lithosphere and implications for its evolution, Geochemistry, Geophysics, Geosystems, pp. 1–20, doi:10.1029/2018GC008033.

Harrowfield, M., Holdgate, G. R., Wilson, C. J. L., and McLoughlin, S., 2005: Tectonic significance of the Lambert graben, East Antarctica: Reconstructing the Gondwanan rift, Geology, 33, 197–200, doi:10.1130/G21081.1.

Hasterok, D. and Chapman, D. S., 2011: Heat production and geotherms for the continental lithosphere, Earth and Planetary Science Letters, 307, 59–70, doi:10.1016/j.epsl.2011.04.034.

Heck, B. and Seitz, K., 2007: A comparison of the tesseroid, prism and point-mass approaches for mass reductions in gravity field modelling, Journal of Geodesy, 81, 121–136, doi:10.1007/s00190-006-0094-0.

Hildenbrand, T. G., Griscom, A., Van Schmus, W. R., and Stuart, W. D., 1996: Quantitative investigations of the Missouri gravity low: A possible expression of a large, Late Precambrian batholith intersecting the New Madrid seismic zone, Journal of Geophysical Research: Solid Earth, 101, 21 921–21 942, doi:10.1029/96JB01908.

Holdgate, G. R., McLoughlin, S., Drinnan, A. N., Finkelman, R. B., Willett, J. C., and Chiehowsky, L. A., 2005: Inorganic chemistry, petrography and palaeobotany of Permian coals in the Prince Charles Mountains, East Antarctica, International Journal of Coal Geology, 63, 156–177, doi:10.1016/j.coal.2005.02.011.

Hole, M. J. and LeMasurier, W. E., 1994: Tectonic controls on the geochemical composition of Cenozoic, mafic alkaline volcanic rocks from West Antarctica, Contributions to Mineralogy and Petrology, 117, 187–202, doi:10.1007/BF00286842.

Hübscher, C., Jokat, W., and Miller, H., 1996: Structure and origin of southern Weddell Sea crust: results and implications, Geological Society, London, Special Publications, 108, 201–211, doi:10.1144/GSL.SP.1996.108.01.15.

Huerta, A. D. and Harry, D. L., 2007: The transition from diffuse to focused extension: Modeled evolution of the West Antarctic Rift system, Earth and Planetary Science Letters, 255, 133–147, doi:10.1016/j.epsl.2006.12.011.

Jachens, R. C. and Moring, B. C., 1990: Maps of the thickness of Cenozoic deposits and the isostatic residual gravity over basement for Nevada, Tech. rep., doi:10.3133/ofr90404.

Jackson, I. and Rigden, S. M., 1996: Analysis of P-V-T data: constraints on the thermoelastic properties of high-pressure minerals, Physics of the Earth and Planetary Interiors, 96, 85–112, doi:10.1016/0031-9201(96)03143-3.

Jackson, I., Fitz Gerald, J. D., Faul, U. H., and Tan, B. H., 2002: Grain-size-sensitive seismic wave attenuation in polycrystalline olivine, Journal of Geophysical Research: Solid Earth, 107, ECV 5–1–ECV 5–16, doi:10.1029/2001JB001225.

Jacobs, J., Elburg, M., Läufer, A., Kleinhanns, I. C., Henjes-Kunst, F., Estrada, S., Ruppel, A. S., Damaske, D., Montero, P., and Bea, F., 2015: Two distinct Late Mesoproterozoic/Early Neoproterozoic basement provinces in central/eastern Dronning Maud Land, East Antarctica: The missing link, 15–21°E, Precambrian Research, 265, 249–272, doi:10.1016/j.precamres.2015.05.003.

Jacobs, J., Opås, B., Elburg, M., Läufer, A., Estrada, S., Ksienzyk, A., Damaske, D., and Hofmann, M., 2017: Cryptic sub-ice geology revealed by a U-Pb zircon study of glacial till in Dronning Maud Land, East Antarctica, Precambrian Research, 294, 1–14, doi:10.1016/j.precamres.2017.03.012.

Janik, T., Grad, M., Guterch, A., and Środa, P., 2014: The deep seismic structure of the Earth's crust along the Antarctic Peninsula-A summary of the results from Polish geodynamical expeditions, Global and Planetary Change, 123, 213–222, doi:10.1016/j.gloplacha.2014.08.018.

Ji, Q., Pang, X., and Zhao, X., 2014: A bibliometric analysis of research on Antarctica during 1993–2012, Scientometrics, 101, 1925–1939, doi:10.1007/s11192-014-1332-5.

Kaban, M. K., 2011: Gravity anomalies, interpretation, Encyclopedia of solid earth geophysics, pp. 456–461.

Kaban, M. K. and Schwintzer, P., 2001: Oceanic upper mantle structure from experimental scaling of Vs ad density at different depths, Geophysical Journal International, 147, 199–214, doi:10.1046/j.0956-540X.2001.01520.x.

Kaban, M. K., Schwintzer, P., and Tikhotsky, S. A., 1999: A global isostatic gravity model of the Earth, Geophysical Journal International, 136, 519–536, doi:10.1046/j.1365-246X.1999.00731.x.

Kaban, M. K., Schwintzer, P., and Reigber, C., 2004: A new isostatic model of the lithosphere and gravity field, Journal of Geodesy, 78, 368–385, doi:10.1007/s00190-004-0401-6.

Kaban, M. K., Tesauro, M., Mooney, W. D., and Cloetingh, S. A. P. L., 2014: Density, temperature, and composition of the North American lithosphere - New insights from a joint analysis of seismic, gravity, and mineral physics data: 1. Density structure of the crust and upper mantle, Geochemistry, Geophysics, Geosystems, 15, 4781–4807, doi: 10.1002/2014GC005483.

Kaban, M. K., Mooney, W. D., and Petrunin, A. G., 2015: Cratonic root beneath North America shifted by basal drag from the convecting mantle, Nature Geoscience, 8, 797–800, doi:10.1038/ngeo2525.

Kaban, M. K., El Khrepy, S., and Al-Arifi, N., 2016a: Isostatic Model and Isostatic Gravity Anomalies of the Arabian Plate and Surroundings, Pure and Applied Geophysics, 173, 1211–1221, doi:10.1007/s00024-015-1164-0.

Kaban, M. K., Stolk, W., Tesauro, M., El Khrepy, S., Al-Arifi, N., Beekman, F., and Cloetingh, S. A. P. L., 2016b: 3D density model of the upper mantle of Asia based on inversion of gravity and seismic tomography data, Geochemistry, Geophysics, Geosystems, 17, 4457–4477, doi:10.1002/2016GC006458.

Kaban, M. K., El Khrepy, S., and Al-Arifi, N., 2017: Importance of the Decompensative Correction of the Gravity Field for Study of the Upper Crust: Application to the Arabian Plate and Surroundings, Pure and Applied Geophysics, 174, 349–358, doi:10.1007/s00024-016-1382-0.

Kanao, M. and Shibutani, T., 2012: Shear Wave Velocity Models Beneath Antarctic Margins Inverted by Genetic Algorithm for Teleseismic Receiver Functions, in: Seismic Waves - Research and Analysis, edited by Kanao, M., chap. 12, pp. 237–252, InTech, doi: 10.5772/32130.

Khan, A., Zunino, A., and Deschamps, F., 2013: Upper mantle compositional variations and discontinuity topography imaged beneath Australia from Bayesian inversion of surface-wave phase velocities and thermochemical modeling, Journal of Geophysical Research: Solid Earth, doi:10.1002/jgrb.50304.

Kirby, J. F., 2005: Which wavelet best reproduces the Fourier power spectrum?, Computers and Geosciences, 31, 846–864, doi:10.1016/j.cageo.2005.01.014.

Kirby, J. F., 2014: Estimation of the effective elastic thickness of the lithosphere using inverse spectral methods: The state of the art, Tectonophysics, 631, 87–116, doi: 10.1016/j.tecto.2014.04.021.

Kirby, J. F. and Swain, C. J., 2004: Global and local isostatic coherence from the wavelet transform, Geophysical Research Letters, 31, 1–5, doi:10.1029/2004GL021569.

Kirby, J. F. and Swain, C. J., 2006: Mapping the mechanical anisotropy of the lithosphere using a 2D wavelet coherence, and its application to Australia, Physics of the Earth and Planetary Interiors, 158, 122–138, doi:10.1016/j.pepi.2006.03.022.

Kirby, J. F. and Swain, C. J., 2008: An accuracy assessment of the fan wavelet coherence method for elastic thickness estimation, Geochemistry, Geophysics, Geosystems, 9, doi: 10.1029/2007GC001773.

Kirby, J. F. and Swain, C. J., 2009: A reassessment of spectral t<inf>e</inf> estimation in continental interiors: The case of North America, Journal of Geophysical Research: Solid Earth, 114, 1–36, doi:10.1029/2009JB006356.

Kirby, J. F. and Swain, C. J., 2011: Improving the spatial resolution of effective elastic thickness estimation with the fan wavelet transform, Computers and Geosciences, 37, 1345–1354, doi:10.1016/j.cageo.2010.10.008.

Klokočník, J., Kosteleckỳ, J., and Bezděk, A.: 2017, Gravitational Atlas of Antarctica, Springer Geophysics, Springer International Publishing.

Krupnik, I., Allison, I., Bell, R., Cutler, P., Hik, D., Lopez-Martinez, J., Rachold, V., Sarukhanian, E., Summerhayes, C., et al., 2011: Understanding earth's polar challenges: International Polar Year 2007-2008.

Krynauw, J. R., Behr, H. J., and Vandenkerkhof, A. M., 1994: Sill Emplacement in Wet Sediments - Fluid Inclusion and Cathodoluminescence Studies at Grunehogna, Western Dronning-Maud-Land, Antarctica, Journal of the Geological Society, 151, 777–794, doi: 10.1144/gsjgs.151.5.0777.

Kuge, K. and Fukao, Y., 2005: High-velocity lid of East Antarctica: Evidence of a depleted continental lithosphere, Journal of Geophysical Research B: Solid Earth, 110, 1–15, doi: 10.1029/2004JB003382.

Kumar, P., Talukdar, K., and Sen, M. K., 2014: Lithospheric structure below transantarctic mountain using receiver function analysis of TAMSEIS data, Journal of the Geological Society of India, 83, 483–492, doi:10.1007/s12594-014-0075-5.

Kurtz, R. D. and Garland, G. D., 1976: Magnetotelluric Measurements in Eastern Canada, Geophysical Journal of the Royal Astronomical Society, 45, 321–347, doi:10.1111/j.1365-246X.1976.tb00329.x.

Lamarque, G., Barruol, G., Fontaine, F. R., Bascou, J., and Menot, R.-P., 2015: Crustal and mantle structure beneath the Terre Adelie Craton, East Antarctica: insights from receiver function and seismic anisotropy measurements, Geophysical Journal International, 200, 807–821, doi:10.1093/gji/ggu430.

Langenheim, V. E. and Jachens, R. C., 1996: Gravity data collected along the Los Angeles Regional Seismic Experiment (LARSE) and preliminary model of regional density variations in basement rocks, southern California, Tech. rep., doi:10.3133/ofr96682.

Laske, G. and Masters, G., 2013: Update on CRUST1. 0—A 1-degree global model of Earth's crust, EGU General Assembly, 15, 2658.

Lawrence, J. F., Wiens, D. A., Nyblade, A. A., Anandakrishnan, S., Shore, P. J., and Voigt, D., 2006: Crust and upper mantle structure of the transantarctic mountains and surrounding regions from receiver functions, surface waves, and gravity: Implications for uplift models, Geochemistry, Geophysics, Geosystems, 7, doi:10.1029/2006GC001282.

Lee, C.-T. A., 2003: Compositional variation of density and seismic velocities in natural peridotites at STP conditions: Implications for seismic imaging of compositional heterogeneities in the upper mantle, Journal of Geophysical Research: Solid Earth, 108, doi:10.1029/2003JB002413.

Leitchenkov, G. L. and Kudryavtzev, G. A., 1997: Structure and Origin of the Earth's Crust in the Weddell Sea Embayment (beneath the Front of the Filchner and Ronne Ice Shelves) from Deep Seismic Sounding data, Polarforschung, 67, 143–154.

Leitchenkov, G. L., Antonov, A. V., Luneov, P. I., and Lipenkov, V. Y., 2016: Geology and environments of subglacial Lake Vostok, Philosophical Transactions of the Royal Society A: Mathematical, Physical and Engineering Sciences, 374, 20140 302, doi:10.1098/rsta.2014.0302.

Lindeque, A., Gohl, K., Henrys, S., Wobbe, F., and Davy, B., 2016: Seismic stratigraphy along the Amundsen Sea to Ross Sea continental rise: A cross-regional record of pre-glacial to glacial processes of the West Antarctic margin, Palaeogeography, Palaeoclimatology, Palaeoecology, 443, 183–202, doi:10.1016/j.palaeo.2015.11.017.

Lisker, F., Brown, R., and Fabel, D., 2003: Denudational and thermal history along a transect across the Lambert Graben, northern Prince Charles Mountains, Antarctica, derived from apatite fission track thermochronology, Tectonics, 22, 1055, doi: 10.1029/2002TC001477.

Lowry, A. R. and Smith, R. B., 1994: Flexural rigidity of the Basin and Range-Colorado Plateau-Rocky Mountain transition from coherence analysis of gravity and topography, Journal of Geophysical Research: Solid Earth, 99, 20 123–20 140, doi:10.1029/94JB00960.

Lythe, M. B., Vaughan, D. G., and and the BEDMAP Consortium, 2001: BEDMAP: A new ice thickness and subglacial topographic model of Antarctica, Journal of Geophysical Research: Solid Earth, 106, 11 335–11 351, doi:10.1029/2000JB900449.

Martos, Y. M., Catalán, M., Jordan, T. A., Golynsky, A., Golynsky, D., Eagles, G., and Vaughan, D. G., 2017: Heat Flux Distribution of Antarctica Unveiled, Geophysical Research Letters, 44, 11,417–11,426, doi:10.1002/2017GL075609.

Maule, C. F., Purucker, M. E., Olsen, N., and Mosegaard, K., 2005: Heat Flux Anomalies in Antarctica Revealed by Satellite Magnetic Data, Science, 309, 464–467, doi: 10.1126/science.1106888.

McKenzie, D., 2003: Estimating T e in the presence of internal loads , Journal of Geophysical Research: Solid Earth, 108, 1–21, doi:10.1029/2002jb001766.

McKenzie, D. and Fairhead, D., 1997: Estimates of the effective elastic thickness of the continental lithosphere from Bouguer and free air gravity anomalies, Journal of Geophysical Research: Solid Earth, 102, 27 523–27 552, doi:10.1029/97JB02481.

McKenzie, D., Yi, W., and Rummel, R., 2015: Estimates of Te for continental regions using GOCE gravity, Earth and Planetary Science Letters, 428, 97–107, doi: 10.1016/j.epsl.2015.07.036.

Mckenzie, D. A. N. and Bowin, C., 1976: on values of With / > Clearly , no such restriction, 81, 1903–1915.

Melchiorre, M., Coltorti, M., Bonadiman, C., Faccini, B., O'Reilly, S. Y., and Pearson, N. J., 2011: The role of eclogite in the rift-related metasomatism and Cenozoic magmatism of Northern Victoria Land, Antarctica, Lithos, 124, 319–330, doi: 10.1016/J.LITHOS.2010.11.012.

Miyamachi, H., Toda, S., Matsushima, T., and Takada, M., 2003: Seismic refraction and wide-angle reflection exploration by JARE-43 on Mizuho Plateau , East Antarctica, Polar Geoscience, 16, 1–21.

Mooney, W. D. and Kaban, M. K., 2010: The North American upper mantle: Density, composition, and evolution, Journal of Geophysical Research, 115, B12 424, doi: 10.1029/2010JB000866.

Morelli, A. and Danesi, S., 2004: Seismological imaging of the Antarctic continental lithosphere: A review, in: Global and Planetary Change, vol. 42, pp. 155–165, doi: 10.1016/j.gloplacha.2003.12.005.

Mukasa, S. B. and Dalziel, I. W. D., 2000: Marie Byrd Land, West Antarctica: Evolution of Gondwana's Pacific margin constrained by zircon U-Pb geochronology and feldspar common-Pb isotopic compositions, Geological Society of America Bulletin, 112, 611–627, doi:10.1130/0016-7606(2000)112¡0611:MBLWAE¿2.3.CO;2.

Naylor, S., Siegert, M., Dean, K., and Turchetti, S., 2008: Science, geopolitics and the governance of Antarctica, Nature Geoscience, 1, 143–145, doi:10.1038/ngeo138.

Nowell, D., 1999: Gravity terrain corrections - an overview, Journal of Applied Geophysics, 42, 117–134, doi:10.1016/S0926-9851(99)00028-2.

O'Donnell, J. P. and Nyblade, A. A., 2014: Antarctica's hypsometry and crustal thickness: Implications for the origin of anomalous topography in East Antarctica, Earth and Planetary Science Letters, 388, 143–155, doi:10.1016/j.epsl.2013.11.051.

Owada, M., Kamei, A., Horie, K., Shimura, T., Yuhara, M., Tsukada, K., Osanai, Y., and Baba, S., 2013: Magmatic history and evolution of continental lithosphere of the Sør Rondane Mountains, eastern Dronning Maud Land, East Antarctica, Precambrian Research, 234, 63–84, doi:10.1016/j.precamres.2013.02.007.

Pappa, F., Ebbing, J., Ferraccioli, F., van der Wal, W., and Blank, B., 2018: A 3D lithospheric model of Antarctica and its implications on mantle viscosity, in: EGU General Assembly Conference Abstracts, vol. 20 of *EGU General Assembly Conference Abstracts*, p. 4939.

Paulson, A., Zhong, S., and Wahr, J., 2005: Modelling post-glacial rebound with lateral viscosity variations, Geophysical Journal International, 163, 357–371, doi:10.1111/j.1365-246X.2005.02645.x.

Paxman, G. J. G., Watts, A. B., Ferraccioli, F., Jordan, T. A., Bell, R. E., Jamieson, S. S. R., and Finn, C. A., 2016: Erosion-driven uplift in the Gamburtsev Subglacial Mountains of East Antarctica, Earth and Planetary Science Letters, 452, 1–14, doi: 10.1016/j.epsl.2016.07.040.

Pérez-Gussinyé, M. and Watts, A., 2005: The long-term strength of Europe and its implications for plate-forming processes, Nature, 436, 381–384, doi:10.1038/nature03854.

Pérez-Gussinyé, M., Lowry, A. R., Watts, A. B., and Velicogna, I., 2004: On the recovery of effective elastic thickness using spectral methods: Examples from synthetic data and from the Fennoscandian Shield, Journal of Geophysical Research: Solid Earth, 109, 1–20, doi:10.1029/2003JB002788.

Pérez-Gussinyé, M., Metois, M., Fernández, M., Vergés, J., Fullea, J., and Lowry, A. R., 2009: Effective elastic thickness of Africa and its relationship to other proxies for lithospheric structure and surface tectonics, Earth and Planetary Science Letters, 287, 152–167, doi:10.1016/j.epsl.2009.08.004.

Petrunin, A. G., Kaban, M. K., Rogozhina, I., and Trubitsyn, V., 2013a: Revising the spectral method as applied to modeling mantle dynamics, Geochemistry, Geophysics, Geosystems, 14, 3691–3702, doi:10.1002/ggge.20226.

Petrunin, A. G., Rogozhina, I., Vaughan, A. P. M., Kukkonen, I. T., Kaban, M. K., Koulakov, I., and Thomas, M., 2013b: Heat flux variations beneath central Greenland's ice due to anomalously thin lithosphere, Nature Geoscience, 6, 746–750, doi: 10.1038/ngeo1898.

Phillips, G. and Läufer, A. L., 2009: Brittle deformation relating to the Carboniferous-Cretaceous evolution of the Lambert Graben, East Antarctica: A precursor for Cenozoic relief development in an intraplate and glaciated region, Tectonophysics, 471, 216–224, doi:10.1016/j.tecto.2009.02.012.

Powell, C. M., Roots, S. R., and Veevers, J. J., 1988: Pre-breakup continental extension in East Gondwanaland and the early opening of the eastern Indian Ocean, Tectonophysics, 155, 261–283, doi:10.1016/0040-1951(88)90269-7.

Price, S. F., Bindschadler, R. A., Hulbe, C. L., and Blankenship, D. D., 2002: Force balance along an inland tributary and onset to Ice Stream D, West Antarctica, Journal of Glaciology, 48, 20–30, doi:10.3189/172756502781831539.

Rabbel, W., Kaban, M., and Tesauro, M., 2013: Contrasts of seismic velocity, density and strength across the Moho, Tectonophysics, 609, 437–455, doi:10.1016/j.tecto.2013.06.020.

Ramillien, G., Lombard, A., Cazenave, A., Ivins, E. R., Llubes, M., Remy, F., and Biancale, R., 2006: Interannual variations of the mass balance of the Antarctica and Greenland ice sheets from GRACE, Global and Planetary Change, 53, 198–208, doi: 10.1016/j.gloplacha.2006.06.003.

Reading, A. M., 2006: The seismic structure of Precambrian and early Palaeozoic terranes in the Lambert Glacier region, East Antarctica, Earth and Planetary Science Letters, 244, 44–57, doi:10.1016/j.epsl.2006.01.031.

Reading, A. M., 2007: The seismicity of the Antarctic plate, The Geological Society of America Special Paper, 425, 285–298, doi:10.1130/2007.2425(18).

Rignot, E., Mouginot, J., and Scheuchl, B., 2011: Ice Flow of the Antarctic Ice Sheet, Science, 333, 1427–1430, doi:10.1126/science.1208336.

Ritzwoller, M. H., Shapiro, N. M., Levshin, A. L., and Leahy, G. M., 2001: Crustal and upper mantle structure beneath Antarctica and surrounding oceans, Journal Of Geophysical Research-Solid Earth, 106, 30 645–30 670, doi:10.1029/2001JB000179.

Robin, G. d. Q., 1953: Measurements of ice thickness in Dronning Maud Land, Antarctica, Nature, 171, 55.

Robin, G. d. Q.: 1958, Glaciology III: Seismic shooting and related investigations, Norsk Polarinstitutt.

Rogozhina, I., Petrunin, A. G., Vaughan, A. P. M., Steinberger, B., Johnson, J. V., Kaban, M. K., Calov, R., Rickers, F., Thomas, M., and Koulakov, I., 2016: Melting at the base of the Greenland ice sheet explained by Iceland hotspot history, Nature Geoscience, 9, 366–372, doi:10.1038/ngeo2689.

Ruppel, A., Jacobs, J., Eagles, G., Läufer, A., and Jokat, W., 2018: New geophysical data from a key region in East Antarctica: Estimates for the spatial extent of the Tonian Oceanic Arc Super Terrane (TOAST), Gondwana Research, 59, 97–107, doi: 10.1016/j.gr.2018.02.019.

Schaeffer, A. J. and Lebedev, S., 2013: Global shear speed structure of the upper mantle and transition zone, Geophysical Journal International, 194, 417–449, doi:10.1093/gji/ggt095.

Schaffer, J., Timmermann, R., Arndt, J. E., Steinhage, D., and Kanzow, T., 2014: RTopo-2: A global dataset of ice sheet topography, cavity geometry and ocean bathymetry to study ice-ocean interaction in Northeast Greenland, REKLIM conference "Our Climate - Our Future", Berlin, Germany, 6 October 2014 - 9 October 2014.

Scheinert, M., Ferraccioli, F., Schwabe, J., Bell, R., Studinger, M., Damaske, D., Jokat, W., Aleshkova, N., Jordan, T., Leitchenkov, G., Blankenship, D. D., Damiani, T. M., Young, D., Cochran, J. R., and Richter, T. D., 2016: New Antarctic gravity anomaly grid for enhanced geodetic and geophysical studies in Antarctica, Geophysical Research Letters, 43, 600–610, doi:10.1002/2015GL067439.

Shapiro, N. M. and Ritzwoller, M. H., 2004: Inferring surface heat flux distributions guided by a global seismic model: Particular application to Antarctica, Earth and Planetary Science Letters, 223, 213–224, doi:10.1016/j.epsl.2004.04.011.

Simmons, N. A., Forte, A. M., and Grand, S. P., 2009: Joint seismic, geodynamic and mineral physical constraints on three-dimensional mantle heterogeneity: Implications for the relative importance of thermal versus compositional heterogeneity, Geophysical Journal International, doi:10.1111/j.1365-246X.2009.04133.x.

Simons, F. J., Zuber, M. T., and Korenaga, J., 2000: Isostatic response of the Australian lithosphere: Estimation of effective elastic thickness and anisotropy using multitaper spectral analysis, Journal of Geophysical Research: Solid Earth, 105, 19 163–19 184, doi:10.1029/2000JB900157.

Simpson, R. W., Jachens, R. C., Blakely, R. J., and Saltus, R. W., 1986: A new isostatic residual gravity map of the conterminous United States with a discussion on the significance of isostatic residual anomalies, Journal of Geophysical Research, 91, 8348, doi:10.1029/JB091iB08p08348.

Sleep, N. H., 2006: Mantle plumes from top to bottom, Earth-Science Reviews, 77, 231–271, doi:10.1016/j.earscirev.2006.03.007.

Smith, A. G. and Drewry, D. J., 1984: Delayed phase change due to hot asthenosphere causes Transantarctic uplift?, Nature, 309, 536–538.

Smith, A. M., Jordan, T. A., Ferraccioli, F., and Bingham, R. G., 2013: Influence of subglacial conditions on ice stream dynamics: Seismic and potential field data from Pine

Island Glacier, West Antarctica, Journal of Geophysical Research: Solid Earth, 118, 1471–1482, doi:10.1029/2012JB009582.

Snyder, J. P.: 1987, Map Projections - A Working Manual, vol. 1395, US Government Printing Office.

Stagg, H. M. J., Colwel, J. B., Direen, N. G., O'Brien, P. E., Bernardel, G., Borissova, I., Brown, B. J., and Ishirara, T., 2004: Geology of the continental margin of Enderby and Mac. Robertson Lands, East Antarctica: Insights from a regional data set, Marine Geophysical Researches, 25, 183–219, doi:10.1007/s11001-005-1316-1.

Stark, C. P., 2003: Wavelet transform mapping of effective elastic thickness and plate loading: Validation using synthetic data and application to the study of southern African tectonics, Journal of Geophysical Research, 108, 1–19, doi:10.1029/2001jb000609.

Steinberger, B. and Calderwood, A. R., 2006: Models of large-scale viscous flow in the Earth's mantle with constraints from mineral physics and surface observations, Geophysical Journal International, 167, 1461–1481, doi:10.1111/j.1365-246X.2006.03131.x.

Stern, T. A. and ten Brink, U. S., 1989: Flexural uplift of the Transantarctic Mountains, Journal of Geophysical Research: Solid Earth, 94, 10 315–10 330, doi:10.1029/JB094iB08p10315.

Stixrude, L. and Lithgow-Bertelloni, C., 2005: Thermodynamics of mantle minerals - I. Physical properties, Geophysical Journal International, 162, 610–632, doi:10.1111/j.1365-246X.2005.02642.x.

Stolk, W., Kaban, M., Beekman, F., Tesauro, M., Mooney, W. D., and Cloetingh, S., 2013: High resolution regional crustal models from irregularly distributed data: Application to Asia and adjacent areas, Tectonophysics, 602, 55–68, doi:10.1016/j.tecto.2013.01.022.

Swain, C. J. and Kirby, J. F., 2003: The effect of 'noise' on estimates of the elastic thickness of the continental lithosphere by the coherence method, Geophysical Research Letters, 30, 1–4, doi:10.1029/2003GL017070.

ten Brink, U. and Stern, T., 1992: Rift Flank Uplifts and Hinterland Basins - Comparison of the Transantarctic Mountains With the Great Escarpment of Southern Africa, Journal of Geophysical Research-Solid Earth, 97, 569–585, doi:10.1029/91JB02231.

ten Brink, U. S., Hackney, R. I., Bannister, S., and Stern, T. A., 1997: Uplift of the Transantarctic Mountains and the bedrock, Journal of Geophysical Research, 102, 27 603–27 621.

Tesauro, M., Kaban, M. K., and Cloetingh, S. A. P. L.: 2010, Thermal and Rheological Model of the European Lithosphere, pp. 71–101, Springer Netherlands, Dordrecht, doi: 10.1007/978-90-481-2737-5_3.

Tesauro, M., Audet, P., Kaban, M. K., Brgmann, R., and Cloetingh, S., 2012: The effective elastic thickness of the continental lithosphere: Comparison between rheological and inverse approaches, Geochemistry, Geophysics, Geosystems, 13, 1–18, doi: 10.1029/2012GC004162.

Tesauro, M., Kaban, M. K., Mooney, W. D., and Cloetingh, S. A. P. L., 2014: Density, temperature, and composition of the North American lithosphere - New insights from a joint analysis of seismic, gravity, and mineral physics data: 2. Thermal and compositional model of the upper mantle, Geochemistry, Geophysics, Geosystems, 15, 4808–4830, doi: 10.1002/2014GC005484.

Tesauro, M., Kaban, M. K., and Mooney, W. D., 2015: Variations of the lithospheric strength and elastic thickness in North America, Geochemistry, Geophysics, Geosystems, 16, 2197–2220, doi:10.1002/2015GC005937.

Tesauro, M., Kaban, M., and Aitken, A., 2018: Temperature and compositional variation in the Australian lithospheric mantle, in: EGU General Assembly Conference Abstracts, vol. 20 of *EGU General Assembly Conference Abstracts*, p. 7661.

Thomson, D., 1982: Spectrum estimation and harmonic analysis, Proceedings of the IEEE, 70, 1055–1096, doi:10.1109/PROC.1982.12433.

Thomson, S. N., Reiners, P. W., Hemming, S. R., and Gehrels, G. E., 2013: The contribution of glacial erosion to shaping the hidden landscape of East Antarctica, Nature Geoscience, 6, 203–207, doi:10.1038/ngeo1722.

Torsvik, T. H., Steinberger, B., Gurnis, M., and Gaina, C., 2010: Plate tectonics and net lithosphere rotation over the past 150 My, Earth and Planetary Science Letters, 291, 106–112, doi:10.1016/j.epsl.2009.12.055.

Trey, H., Cooper, A. K., Pellis, G., Della Vedova, B., Cochrane, G., Brancolini, G., and Makris, J., 1999: Transect across the West Antarctic rift system in the Ross Sea, Antarctica, Tectonophysics, 301, 61–74, doi:10.1016/S0040-1951(98)00155-3.

Turcotte, D. and Schubert, G.: 1982, Geodynamics, Cambridge University Press, 2 edn.

van Wijk, J. W., Lawrence, J. F., and Driscoll, N. W., 2008: Formation of the Transantarctic Mountains related to extension of the West Antarctic Rift system, Tectonophysics, 458, 117–126, doi:10.1016/j.tecto.2008.03.009.

Veevers, J. J., 2007: Pan-Gondwanaland post-collisional extension marked by 650-500??Ma alkaline rocks and carbonatites and related detrital zircons: A review, Earth-Science Reviews, 83, 1–47, doi:10.1016/j.earscirev.2007.03.001.

Veevers, J. J., 2012: Reconstructions before rifting and drifting reveal the geological connections between Antarctica and its conjugates in Gondwanaland, Earth-Science Reviews, 111, 249–318, doi:10.1016/j.earscirev.2011.11.009.

Watts, A. B., 1978: An analysis of isostasy in the world's oceans 1. Hawaiian-Emperor Seamount Chain, Journal of Geophysical Research: Solid Earth, 83, 5989–6004, doi:10.1029/JB083iB12p05989.

Watts, A. B.: 2001, Isostasy and Flexure of the Lithosphere, Cambridge University Press.

Watts, A. B., Sandwell, D. T., Smith, W. H. F., and Wessel, P., 2006: Global gravity , bathymetry , and the distribution of submarine volcanism through space and time, 111, 1–26, doi:10.1029/2005JB004083.

Wienecke, S. and Braitenberg, C., 2007: A new analytical solution estimating the flexural rigidity in the Central Andes, Geophysical Journal International, pp. 789–794, doi:10.1111/j.1365-246X.2007.3396.x.

Willett, S. D., Chapman, D. S., and Neugebauer, H. J., 1985: A thermo-mechanical model of continental lithosphere, Nature, 314, 520–523, doi:10.1038/314520a0.

Wilson, D., Baldridge, W. S., Aster, R., West, M., Ni, J., Grand, S., Gao, W., Semken, S., and Patel, P., 2005: Lithospheric structure of the Rio Grande rift., Nature, 433, 851–855, doi:10.1038/nature03297.

Wobbe, F., Lindeque, A., and Gohl, K., 2014: Anomalous South Pacific lithosphere dynamics derived from new total sediment thickness estimates off the West Antarctic margin, Global and Planetary Change, 123, 139–149, doi:10.1016/j.gloplacha.2014.09.006.

Yamasaki, T., Miura, H., and Nogi, Y., 2008: Numerical modelling study on the flexural uplift of the Transantarctic Mountains, Geophysical Journal International, 174, 377–390, doi:10.1111/j.1365-246X.2008.03815.x.

Zorin, Y. A., Pismenny, B., Novoselova, M., and Turutanov, E. K., 1985: Decompensative gravity anomalies, Geologia i Geofizika, 8, 104–108.

Zorin, Y. A., Belichenko, V. G., Turutanov, E. K., Kozhevnikov, V. M., Ruzhentsev, S. V., Dergunov, A. B., Filippova, I. B., Tomurtogoo, O., Arvisbaatar, N., Bayasgalan, T., Biambaa, C., and Khosbayar, P., 1993: The South Siberia-Central Mongolia transect, Tectonophysics, 225, 361–378, doi:10.1016/0040-1951(93)90305-4.

ACKNOWLEDGMENTS

Throughout the writing of this dissertation and throughout this entire PhD project, I have received a great deal of support and assistance from my colleagues, family and friends. I want to take this opportunity to express my thanks to all of them.

First of all, I would like to express my gratitude to my adviser Prof. Dr. Maik Thomas. His door was always open whenever I ran into a problem or had a question, be it on my research, my writing or the administrative side of a PhD project.

Many thanks go to my supervisor, Dr. habil. Mikhail Kaban for offering me the opportunity to undertake this exciting and challenging project and for his guidance and assistance through every step of it. Without his commitment and invaluable expertise especially on lithospheric modeling this thesis would not have been possible.

I would also like to thank Prof. Dr. Jörg Ebbing who agreed to be the reviewer for this thesis. His advice on this dissertation and on several SPP meeting was greatly appreciated.

I want to acknowledge Dr. Alexei Petrunin for his support during this PhD project and for always giving me valuable feedback on my article manuscripts and presentations.

I am grateful to Dr. Magdala Tesauro for her valuable guidance in thermal modeling and for giving me the opportunity to working with her on this subject in Trieste.

My sincere thanks go to the entire Section 1.3. Thank you for making me feel welcome, when I first started at GFZ, for the many interesting discussions, on topic or otherwise, for the help that was given freely, whenever I needed it and for the new-found friendships. It was a pleasure to work with you during these last years.

Last but not least, I want to thank my family and friends for accompanying and supporting

me through this interesting but also at times challenging time of my life. Your encouragement and moral support helped me a great deal! Most of all, I want to thank my mother, Petra Haeger. You always supported me in every way possible. It was your broad curiosity of the world that also sparked my first interest in science. Without you, I would not be where I am now.

A Supporting Information for 3D density, thermal and compositional model of the Antarctic lithosphere and implications for its evolution

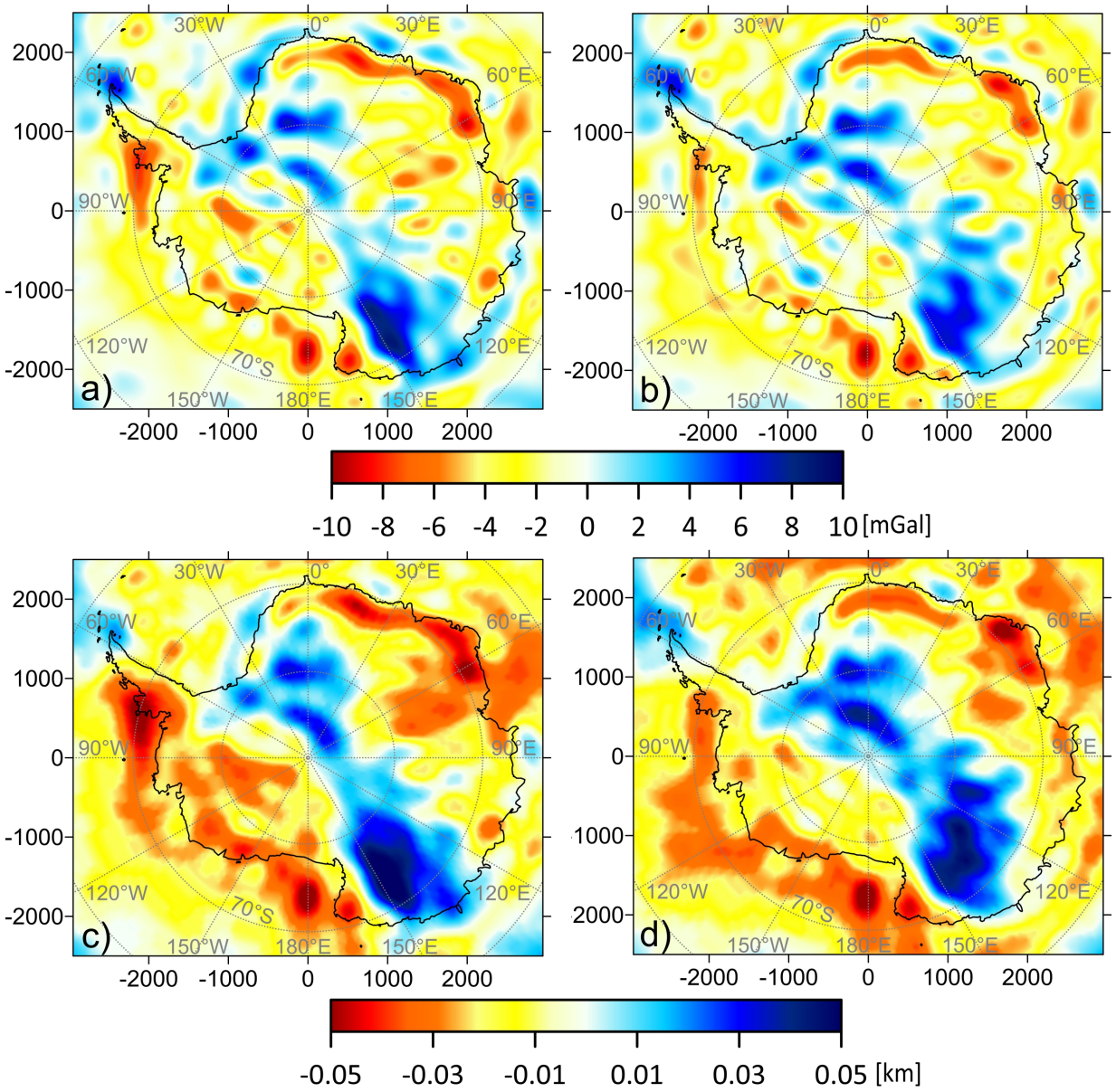

Figure A.1.: Non-fitted residuals after the final iteration of the gravity field using (a) the SL2013sv model and (b) the AN1-S model and of the residual topography calculated for a reference density of 2.67 g/cm^3, using (c) the SL2013sv model and (d) the AN1-S model